



Faculteit Wetenschappen  
Departement Fysica

# **2D and 3D Characterization of Plasmonic and Porous Nanoparticles using Transmission Electron Microscopy**

2D- en 3D-karakterisering van plasmonische en poreuze  
nanodeeltjes met behulp van transmissie-elektronenmicroscopie

Proefschrift voorgelegd tot het behalen van de graad van  
Doctor in de Wetenschappen  
aan de Universiteit Antwerpen, te verdedigen door  
**Kadir Şentosun**

Promotor: Prof. Dr. Sara Bals

Antwerp, 2018

## **Doctoral Committee**

### **Chairperson**

Prof. Dr. Sabine Van Doorslaer, University of Antwerp - Belgium

### **Promoter**

Prof. Dr. Sara Bals, University of Antwerp - Belgium

### **Members**

Prof. Dr. Pierre Van Mechelen, University of Antwerp - Belgium

Prof. Dr. Dirk Van Dyck, University of Antwerp - Belgium

Prof. Dr. Kees Joost Batenburg, University of Leiden - The Netherlands

Dr. Jon Ustarroz, Vrije Universiteit Brussel - Belgium

Prof. Dr. Sammy Verbruggen, University of Antwerp - Belgium

## **Contact information**

Kadir Sentosun

University of Antwerp - Department of Physics

EMAT - Electron Microscopy for Materials Science

Groenenborgerlaan 171

B-2020 Antwerp

Belgium

kadir.sentosun@uantwerpen.be

# Preface

Plasmonic and porous nanoparticles have attracted high interest during the last years due to their unique properties of interest for numerous applications in different fields ranging from biomedicine to optoelectronics. The combination of these structures opens up even more possibilities. Since the properties of nanostructures are closely related to their three dimensional (3D) structure and morphology, the rational design of nanomaterials strongly depends on the availability of quantitative 3D characterization tools. Transmission electron microscopy (TEM) is one of the most suitable characterization techniques to investigate nanosystems at the nanometer scale and below. However, images acquired by TEM only correspond to a two dimensional (2D) projection of a 3D object. To overcome this limitation, “electron tomography” is required. This technique enables one to obtain a 3D reconstruction of a nanomaterial using tilt series of 2D projection images. Although the technique has progressed significantly in the last decade, a quantitative 3D characterization of plasmonic and porous nanoparticles remains challenging. In this thesis, I have applied electron tomography to a broad range of materials. For the majority of the investigated systems, a 3D investigation was only possible by developing innovative approaches for electron tomography. Especially the investigation of hybrid soft-hard systems (e.g. a plasmonic particle in a porous SiO<sub>2</sub> shell) matter is extremely challenging. I therefore optimized the acquisition of the tilt series and developed different new reconstruction techniques in the field of electron tomography. It is only through the development of these new techniques that I was able to investigate the hybrid metallic-porous structures in the thesis. These novel methodologies are furthermore applicable to a broad range of investigations, e.g. to study materials that are very sensitive to the electron beam. My contribution is therefore not only of importance in this thesis, but will certainly be of great use in the field of (3D) electron microscopy and nanoscience in general.

In **Chapter 1**, an introduction on the different imaging modes in TEM is presented, followed by a historical overview and the main principles of electron tomography.

In **Chapter 2**, a 3D structural characterization of plasmonic Au nanostars encapsulated in a Au shell is performed. The use of high angle annular dark field scanning transmission electron microscopy (HAADF-STEM) tomography enables us to characterize these nanoparticles in 3D and to elucidate on the internal gaps between the Au nanostars and overgrown shell. The outcome of my experiments facilitated a better understanding of the connection between the 3D structure and the enhancement in the Raman intensity. This connection was also investigated by electric field simulations which were based on the electron tomography results I obtained.

Different plasmonic CuTe nanocrystals are investigated in **Chapter 3**. The plasmonic properties of such CuTe nanocrystals originate from the presence of Cu vacancies. By combining different 3D TEM techniques, we were able to visualize atomic vacancies in 3D. This was only possible by the development of a new reconstruction approach. The outcome of our experiment was used as an input for density functional theory (DFT) calculations enabling to understand the influence of the 3D structure on the optical properties.

In **Chapter 4**, a new quantification methodology, applied to porous Pt nanoparticles is presented. Hereby, a 3D procedure is developed which classifies the pores either as chemically active pores or as chemically inactive cavities. Based on this precise quantification, the influence of different electrodeposition voltages on the nanoparticle porosity could be revealed. This is an important achievement since so far, it was not straightforward to obtain porosity measurements at a local scale.

In **Chapter 5**, a methodology to investigate functional plasmonic-porous nanoparticles in 3D is presented. Because of their soft-hard structure, the characterization of these hybrid nanoparticles is very challenging. An example of a hybrid nanostructure is a Au nanoparticle encapsulated by mesoporous silica ( $\text{SiO}_2$ ). Due to the high atomic number difference of the different components, the data acquisition and reconstruction steps need to be optimized in order to characterize both components in a reliable manner. I therefore proposed an approach which is based on the simultaneous use of 2 ADF detectors. In addition I proposed a new approach to perform the 3D reconstruction in such a manner that remaining artifacts

can be overcome. It is only because of the development of this new methodology that I was able to investigate the nanostructures in Chapter 6. This proves the importance of the new technique.

In **Chapter 6**, I applied the technique I developed in Chapter 5 to obtain a better understanding of the growth of different Au morphologies encapsulated by SiO<sub>2</sub>. Because of the optimized characterization, we were able to visualize the interface between the soft and hard compound. We were also able to reveal the influence of the surfactant on the growth of ZIF-8 on Au@Ag nanorods. Due to the anisotropic nature of the hybrid compounds, this information cannot be obtained by conventional microscopy.

In **Chapter 7**, a methodology to obtain reliable 3D reconstructions based on tilt series with a highly limited number of projection images is presented. The methodology exploits the properties of Radon space, where a sinogram can be decomposed into single sine waves. This methodology is of uttermost importance to investigate beam sensitive materials, such as the hybrid systems in this thesis. In the field of microscopy this methodology is of great use since conventionally, a very large number of projection images is required for a 3D reconstruction. The new approach is able to overcome this limitation.

# Voorwoord

Gedurende de laatste decennia is de belangstelling naar plasmonische, poreuze en de hybride plasmonisch-poreuze nanomaterialen enorm gestegen vanwege hun unieke eigenschappen die nuttig zijn voor talrijke toepassingen, gaande van medische biologie tot opto-elektronica. De eigenschappen van nanomaterialen zijn sterk verbonden met hun driedimensionale (3D) structuur en morfologie, waardoor het voor de ontwikkeling van nanomaterialen erg belangrijk is dat er methodes beschikbaar zijn die deze materialen kwantitatief in 3D kunnen karakteriseren. Een zeer geschikte techniek om de morfologie tot op nanometer- en zelfs atomaire schaal te bestuderen is transmissie-elektronenmicroscopie (TEM). TEM levert echter enkel een tweedimensionale (2D) projectieafbeelding van een 3D object. Om deze beperking te overwinnen is elektronentomografie nodig. Deze techniek maakt gebruik van een tiltserie van 2D projectieafbeeldingen om een 3D reconstructie te maken. Ondanks de geboekte vooruitgang binnen de elektronentomografie in het laatste decennium blijft de 3D karakterisering van plasmonische en poreuze nanodeeltjes met behulp van elektronentomografie een uitdaging. In dit proefschrift heb ik een grote verscheidenheid aan materialen onderzocht met elektronentomografie. Voor het merendeel van deze materialen was een 3D onderzoek alleen mogelijk door elektronentomografie te gebruiken in combinatie met een nieuwe innovatieve aanpak. Vooral de hybride zacht-harde materialen, zoals een plasmonisch deeltje in een poreuze SiO<sub>2</sub> schil, zijn een grote uitdaging om te onderzoeken. Daarom heb ik de acquisitie van de tiltserie geoptimaliseerd en heb ik verschillende nieuwe reconstructietechnieken binnen de elektronentomografie ontwikkeld. Dit heeft er voor gezorgd dat ik de hybride metallisch-poreuze structuren in dit proefschrift kon onderzoeken. Deze nieuwe methodes zijn bovendien toepasbaar bij veel verschillende studies, zoals het onderzoek naar materialen die snel beschadigd raken door de elektronenbundel. Mijn bijdrage is daarom niet alleen belangrijk voor deze thesis, maar is ook van belang binnen de (3D) elektronenmicroscopie en nanowetenschap.

In **Hoofdstuk 1** wordt een inleiding over de verschillende beeldvormingsmethodes in een TEM gegeven, gevolgd door een historisch overzicht met de beginselen

van elektronentomografie.

In **Hoofdstuk 2** is een 3D structurele karakterisering gemaakt van plasmonische Au nanosterren die bedekt zijn met een Au schil. Doormiddel van tomografie voor donkerbeeldvorming met een ringvormige detector (HAADF: high angle annular dark field) rastertransmissie-elektronenmicroscopie (STEM: scanning TEM) kunnen deze nanodeeltjes in 3D gekarakteriseerd worden, wat het mogelijk maakt om de interne holtes tussen de Au nanosterren en de overgroeide schil te onderzoeken. De resultaten van mijn experimenten zorgden ervoor dat de relatie tussen de 3D structuur en de versterking van de Ramanintensiteit beter begrepen kan worden. Deze relatie is ook onderzocht met behulp van simulaties van het elektrische veld waarbij mijn elektrotomografie resultaten zijn gebruikt.

Verschillende plasmonische CuTe-nanokristallen zijn onderzocht in **Hoofdstuk 3**. De plasmonische eigenschappen van dergelijke CuTe-nanokristallen ontstaan doordat Cu-atomen niet overal in de kristalstructuur aanwezig zijn. Daarom zijn verschillende 3D TEM-technieken gebruikt om de aan- en afwezigheid van deze Cu-atomen in 3D te bestuderen. Dit was echter alleen mogelijk doordat een nieuwe aanpak voor de reconstructie ontwikkeld is. De resultaten van ons experiment zijn gebruikt als input voor dichtheidsfunctionaaltheorie (DFT) berekeningen om de invloed van de 3D structuur op de optische eigenschappen te begrijpen.

In **Hoofdstuk 4** wordt een nieuwe kwantificatiemethode gepresenteerd die gebruikt is voor poreuze Pt-nanodeeltjes. Deze 3D procedure classificeert porin als chemisch actief of als chemisch inactief. Op basis van deze precieze kwantificatie is de invloed van verschillende elektrodepositiespanningen op de porositeit van de nanodeeltjes gevonden. Dit is een belangrijke prestatie aangezien het tot nu toe niet eenvoudig was om porositeitsmetingen lokaal te verrichten.

In **Hoofdstuk 5** wordt een methode gepresenteerd om functionele plasmonisch-poreuze nanomaterialen in 3D te onderzoeken. Vanwege hun zacht-harde structuur is de karakterisering van deze hybride nanodeeltjes zeer uitdagend. Een voorbeeld van een hybride nanostructuur is een Au-nanodeeltje bedekt met mesoporeus silica ( $\text{SiO}_2$ ). Vanwege het grote verschil in atoomnummer van de verschillende componenten, moeten zowel de acquisitie als de reconstructie worden geoptimaliseerd om

beide componenten op een betrouwbare manier te karakteriseren. Ik heb daarom een benadering voorgesteld waarbij gelijktijdig 2 ADF detectoren gebruikt worden. Daarnaast heb ik een nieuwe benadering voor de 3D reconstructie voorgesteld zodat de overblijvende artefacten overwonnen kunnen worden. De ontwikkeling van deze nieuwe methode was noodzakelijk om de nanostructuren in Hoofdstuk 6 te onderzoeken, wat het belang van deze methode aantoont.

In **Hoofdstuk 6** gebruik ik de techniek uit Hoofdstuk 5 om de groei van verschillende door SiO<sub>2</sub> bedekte Au morfologien beter te begrijpen. Door de geoptimaliseerde karakterisering konden we een beeld vormen van de overgang tussen de zachte en harde materie. Hiernaast konden we de invloed bepalen van de oppervlakte-actieve stof op de groei van ZIF-8 op Au@Ag nanostaven. Door de anisotrope aard van de hybride deeltjes kan deze informatie niet verkregen worden door conventionele microscopie.

In **Hoofdstuk 7** wordt een methode voorgesteld om betrouwbare 3D reconstructies op basis van tiltseries met een zeer beperkt aantal projectiebeelden te verkrijgen. Deze methode maakt gebruik van de eigenschappen van de Radonruimte, waarin een sinogram kan worden ontbonden in verschillende sinusgolven. Deze methode is uiterst belangrijk om bundelgevoelige materialen te onderzoeken, zoals de hybride deeltjes in dit proefschrift. Binnen de elektronentomografie is deze methode erg nuttig omdat normaal gezien een groot aantal projectieafbeeldingen nodig zijn voor een 3D reconstructie. Deze nieuwe benadering kan deze beperking overwinnen.



# Contents

<b>1</b>	<b>Introduction to Transmission Electron Microscopy and Electron Tomography</b>	<b>1</b>
1.1	Introduction . . . . .	2
1.2	Introduction to electron tomography and transmission electron microscope . . . . .	3
1.2.1	Imaging in a TEM . . . . .	4
1.2.2	Electron Diffraction . . . . .	6
1.2.3	Spectroscopy in a TEM . . . . .	7
1.3	Electron tomography . . . . .	9
1.3.1	General aspects of electron tomography . . . . .	9
1.3.2	History of electron tomography . . . . .	10
1.4	Practical tomography . . . . .	11
1.4.1	Acquisition . . . . .	11
1.4.2	Alignment . . . . .	15
1.4.3	Reconstruction . . . . .	17
1.4.4	Visualization of electron tomography 3D tomogram . . . . .	24
<b>2</b>	<b>Application of Electron Tomography for Characterization of Plasmonic Nanoparticles</b>	<b>27</b>
2.1	Introduction to Plasmonic nanoparticles . . . . .	28
2.2	Encapsulation of Au nanostars via seeded growth . . . . .	31
2.2.1	SERS performance of coated Au nanostars . . . . .	38
2.2.2	Growth of Diverse Au nanostructures . . . . .	39

2.3	Conclusions . . . . .	42
<b>3</b>	<b>Structure and Vacancy Distribution in Copper Telluride Nanoparticles Influence Plasmonic Activity</b>	<b>43</b>
3.1	Introduction to Copper Telluride nanoparticles . . . . .	44
3.2	Investigation of Structure and Vacancy distribution of CuTe nanoparticles . . . . .	44
3.2.1	Structural Characterization . . . . .	46
3.2.2	Structure property correlation . . . . .	54
3.3	Conclusions . . . . .	57
<b>4</b>	<b>Characterization of Porous Pt Nanoparticles using Electron Tomography</b>	<b>59</b>
4.1	Introduction to Porous nanomaterials . . . . .	60
4.2	3D Porosity investigation of Pt nanoparticles . . . . .	61
4.2.1	2D Characterization . . . . .	63
4.2.2	3D Characterization . . . . .	65
4.2.3	Growth mechanism of electrodeposited Pt nanoparticles . . . . .	68
4.2.4	Investigation of Electrocatalytic Stability of Pt nanostructures using Electron Tomography . . . . .	70
4.3	Conclusions . . . . .	72
<b>5</b>	<b>Combination of HAADF-STEM and ADF-STEM Tomography for Core-Shell Hybrid Materials.</b>	<b>73</b>
5.1	Introduction to Multi-functional nanoparticles . . . . .	74
5.1.1	Experimental Details . . . . .	76
5.1.2	Conventional Reconstruction . . . . .	77
5.1.3	Optimization of acquisition of tilt series . . . . .	80
5.1.4	Optimization of the 3D reconstruction procedure . . . . .	80
5.2	Conclusions . . . . .	84
<b>6</b>	<b>Characterization of Plasmonic-Porous Hybrid Nanostructures</b>	<b>85</b>
6.1	Introduction . . . . .	87

6.2	Introduction to Au / Au-Ag nanoparticles encapsulated with mesoporous silica . . . . .	92
6.2.1	Growth of mesoporous silica on Au nanoparticle . . . . .	93
6.2.2	Overgrowth of Ag through the pores . . . . .	96
6.2.3	Overgrowth of Au through the pores . . . . .	97
6.2.4	SERS performance of branched Au nanoparticle . . . . .	101
6.2.5	Conclusions on silica coated Au / Au-Ag nanostructures . .	102
6.3	Introduction to MOF coated Au-Ag nanomaterials . . . . .	103
6.3.1	CTAB mediated ZIF-8 growth . . . . .	104
6.3.2	CTAB/TRIS mediated ZIF-8 growth . . . . .	108
6.3.3	Conclusions . . . . .	111
<b>7</b>	<b>Artifact Reduction Based on Sinogram Interpolation for the 3D Reconstruction of Nanoparticles</b>	<b>113</b>
7.1	Introduction . . . . .	114
7.2	Methodology . . . . .	115
7.2.1	Radon space and sinogram . . . . .	115
7.2.2	Preselection of single sine waves . . . . .	116
7.2.3	Interpolation of a sparse sine wave . . . . .	118
7.2.4	Reduction of missing wedge artifacts . . . . .	120
7.3	Experimental Results . . . . .	123
7.3.1	Qualitative and quantitative comparison . . . . .	123
7.3.2	NaYF <sub>4</sub> Hexagonal plates . . . . .	127
7.4	Discussion . . . . .	127
7.5	Conclusions . . . . .	129
<b>8</b>	<b>Conclusions and Outlook</b>	<b>131</b>
8.1	Conclusions and Outlook . . . . .	132
	<b>Bibliography</b>	<b>134</b>

# List of abbreviations

2D	Two dimensional
3D	Three dimensional
ADF	Annular dark field
BDT	1,4-benzenedithiol
BET	BrunauerEmmettTeller
BF	Bright field
CCD	Charged couple device
CTAB	Cetyltrimethylammonium bromide
CTAC	Cetyltrimethylammonium chloride
CuTe	Copper Telluride
DFT	Density functional theory
EDX	Energy dispersive X-ray
EELS	Electron energy loss spectroscopy
FT	Fourier transform
FIB	Focused ion beam
HAADF	High angle annular dark field
LSPR	Localized surface plasmon resonances
MOF	Metal Organic Framework
ORR	Oxygen Reduction Reaction
PEMFC	Polymer electrolyte membrane fuel cells
PVP	Poly vinyl pyrrolidone
RED	Rotation electron diffraction
SAED	Selected area electron diffraction
SBA	Santa Barbara Amorphous type
SBU	Secondary building units
SEM	Scanning electron microscope
SERS	Surface Enhanced Raman Scattering
SIRT	Simultaneous iterative reconstruction technique

STEM	Scanning transmission electron microscope
TEM	Transmission electron microscope
TRIS	Tris(hydroxymethyl) Aminomethane
TVM	Total variation minimization
VW	Volmer-Weber
WBP	Weighted backprojection

# Chapter 1

## Introduction to Transmission Electron Microscopy and Electron Tomography

## 1.1 Introduction

Materials which have at least one dimension ranging from 1 to 100 nm are referred to as “nanomaterials”. Depending on the number of dimensions in the nanometer range, they are categorized as 2D, 1D and 0D nanomaterials or nanoparticles. Nanoparticles with three confined dimensions are of specific interest since they exhibit unique size dependent properties which serve as the basis for their applications. For example, an inactive metal, such as Au, is catalytically active for CO oxidation when it is present in the form of a nanoparticle with a size of 2-3 nm and dispersed on TiO<sub>2</sub> or CeO<sub>2</sub> [1]. Larger Au nanoparticles can, for example, be used in applications such as cancer treatment and biomedical imaging. The optical absorption as a physical property of the Au nanoparticles is highly shape dependent and is different in comparison to the bulk property [2]. Here, the size and shape of the nanoparticles are of great importance since these will determine the resonance energy and hence the wavelength of the laser that should be used to excite the nanoparticles for these applications. In Figure 1.1 a and b, surface plasmon extinction spectra of Au nanorods with different aspect ratios together with a representative image of a Au nanorod are displayed. It can be observed that depending on the aspect ratio, the absorption maximum varies. For instance, Au nanorods with an aspect ratio of 3.9 have an absorption maximum of 800 nm, this range overlaps with the minimum of extinction of human tissues [3] which is important for applications such as imaging of a cancer cell in living organisms.

Different functional nanomaterials are often combined in so-called multi-functional nanoparticles. For instance, porous materials such as mesoporous silica or metal organic frameworks (MOF) are used in combination with Au nanoparticles for optimized drug delivery due to their tunable pore sizes in nanometer-scale, and well-defined surface properties [4-9]. Moreover, due to their high surface to volume ratio, porous materials are of great importance for catalytic purposes. Especially, Pt nanoparticles with a dendritic morphology are ideal candidates for highly efficient fuel cells.

The physical properties of nanoparticles are closely related to their composition,

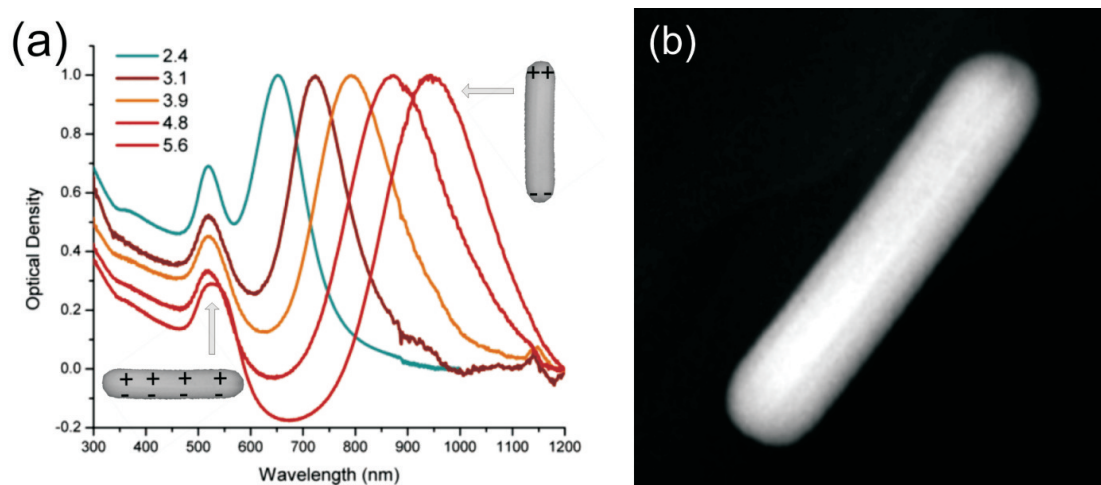


Figure 1.1: (a) Surface plasmon extinction spectra of Au nanorods of different aspect ratios, showing the dependence of the strong longitudinal band on the aspect ratios of the nanorod. The weaker transversal band can also be observed which depends less on aspect ratio [3]. (b) A Au nanorod with an aspect ratio of 4.8.

size and shape. It is therefore of crucial importance to understand the structure-property relationship in order to provide input for predicting their properties and to guide the synthesis towards novel nanomaterials with specific properties. For this purpose, transmission electron microscopy (TEM) is one of the most suitable techniques. In the remainder of this chapter, an introduction to TEM is provided.

## 1.2 Introduction to Transmission Electron Microscope

The first TEM was built by Ernst Ruska in the 1930s. From top to bottom, a TEM consists of an electron gun, condenser lens system, specimen stage, objective lens and projection lens system. In a TEM column, electrons which are emitted from a source are first accelerated and then directed to an electron transparent specimen (thickness  $< 100$  nm). Before reaching the specimen under investigation, the

desired size, intensity and convergence angle of the electron beam are obtained by the lenses of the condenser system. A condenser aperture can be inserted to select the electrons that follow a trajectory close to the optical axis of the microscope in order to minimize the effect of the aberration caused by the condenser lenses. Next, the electrons of the electron beam interact with the specimen, which is mounted in a dedicated specimen holder. The objective lens, which is located close to the specimen focuses the electrons after interaction with the specimen and generates a diffraction pattern in the back focal plane of the objective lens (see Figure 1.2). Afterwards, the diffracted beam disperses and forms the magnified image in the image plane of the objective lens. Further magnification is achieved by the projection lens system. The transmitted electrons are collected on a charged coupled device (CCD) or a spectrometer which yields projections or spectra of the investigated object.

In physical sciences, the electrons are accelerated to several hundred kV. Under perfect conditions (without any lens aberrations), as the acceleration of the electrons increases, the wavelength of electrons decreases. Therefore, the resolution of the microscope increases. The relation between the wavelength and resolution  $d$  is given by:

$$d = \frac{\lambda}{2NA} \quad (1.1)$$

with NA being the numerical aperture (dimensionless number which defines the range of angles that an optical lens can receive or emit light) of the objective lens. For a wavelength of 2-4 pm (300kV), a resolution in sub-angstrom levels is reachable. However, due to existing aberration in the lens systems, the resolution is limited to approximately 1 Å for a non-aberration corrected microscope. Therefore, TEM is an excellent instrument to study nanomaterials at the nanometer and atomic scale.

### 1.2.1 Imaging in a TEM

In a TEM, several imaging methods are present. All the techniques depend on the type of interaction between the incoming electron beam with the investigated spec-

imen. Selecting the proper imaging mode for an electron tomography experiment is of crucial importance. Therefore, this section describes the different imaging modes in a TEM.

### 1.2.1.1 Bright-field TEM

When using bright field (BF)TEM imaging, the sample is illuminated with a parallel electron beam (see Figure 1.2) and mainly elastically scattered electrons are collected. BF imaging is dominated by two different contrast mechanisms: mass-thickness contrast and diffraction contrast. For mass-thickness contrast, denser regions of the sample or regions with heavier elements present will scatter incoming electrons to higher angles. As shown in Figure 1.2, electrons scattered to high angles are cut off by an objective aperture and therefore these regions appear dark in the final image. When the sample is crystalline, scattering of the electrons follows Bragg's law [10]:

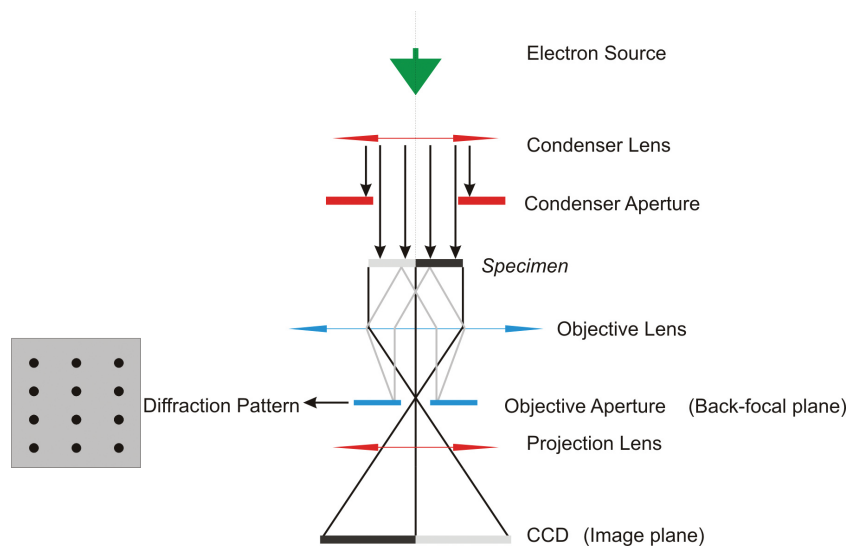


Figure 1.2: Illustration of mass-thickness contrast mechanism. The dependency of the signal on the mass (thickness) from a sample with regions in different density is shown. More scattering for the higher mass (thicker) regions results in darker regions in the projection image.

$$\lambda = 2d\sin\theta \quad (1.2)$$

where  $\lambda$  is the wavelength of the incoming electrons,  $d$  is the inter-planar spacing of the atomic planes and  $\theta$  is the angle of the incident electrons with respect to the lattice planes. Depending on the angle ( $\theta$ ) between the electron beam and the lattice planes, destructive or constructive interference may occur. A polycrystalline sample with grains of similar thickness, but with a different crystal orientation, yields very different intensity levels in a BF-TEM image depending on their zone axis orientation. This is useful to distinguish different regions of a sample with different crystallinity.

### 1.2.1.2 High angle annular dark field - scanning transmission electron microscopy

In high angle annular dark field scanning transmission electron microscopy (HAADF-STEM) mode, the electron beam is focused into a probe using the condenser lens system. The probe is scanned across a region of interest and the scattered electrons are integrated using a scintillation annular detector for each probe position (see Figure 1.3). Nuclear scattering (incoming electron-nucleus interaction) establishes the base of this imaging mode. Hence, the intensity of HAADF-STEM imaging depends on variation in thickness and atomic number ( $Z^{1.6-2}$ ) [11]. Depending on the scattering angle, the electrons can be detected using different detectors. Electrons scattered to low angles are collected ( $< 10$  mrad) using a BF detector, between 10 and 50 mrad using an annular dark field (ADF) and electrons scattered to angles higher than 50 mrad are detected using a high angle ADF (HAADF) detector. Light elements such as B or O can be detected using the ADF detector. To image heavier elements such as Ag and Au the HAADF detector can be used.

## 1.2.2 Electron Diffraction

To obtain a diffraction pattern, a small region on a thin film or nanoparticle is selected using a selective area electron diffraction (SAED) aperture. The diffraction pattern can be acquired by projecting the back-focal plane (see Figure 1.2)

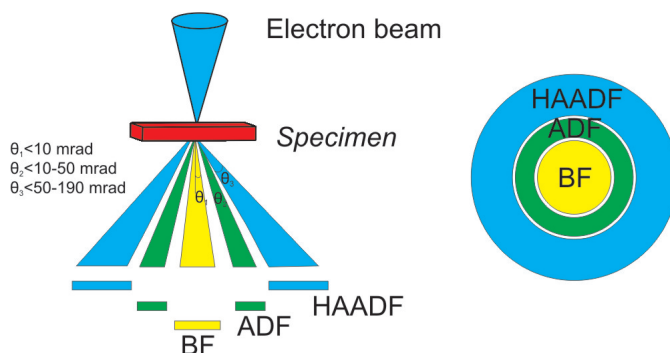


Figure 1.3: Schematic illustration of STEM imaging. A focused electron beam is scanned over the sample and using the different detectors which are located below the sample, electrons scattered to different angles are collected.

of the objective lens on a CCD camera. A diffraction pattern is formed when the scattering of electrons from the lattice planes occurs in a constructive manner. The electrons which are scattered from a crystal lattice generate a diffraction pattern as schematically illustrated in Figure 1.2. The spacing between the spots in a given pattern corresponds to the inter-planar distances ( $d$  value in Equation 1.2) in the crystalline material.

### 1.2.3 Spectroscopy in a TEM

In order to reveal chemical information about the investigated specimen, spectroscopy is performed using mainly two different methods, explained in the following sections.

#### 1.2.3.1 Energy Dispersive X-ray spectroscopy

Energy dispersive X-ray (EDX) spectroscopy is based on the interaction of incoming electrons with inner-shell electrons of the specimen. This interaction results in an excitation of an inner shell electron of an atom in the specimen to higher energy levels, creating an electron hole. This hole can be filled by a higher energy electron, which results in generating X-rays, Auger electrons and/or visible light. Next, the hole is filled by a higher energy electron. The energy difference between

two electrons is emitted as an X-ray [10, 12]. The generated X-rays are used in EDX, which are characteristic for each atom type. Therefore, the use of EDX enables elemental identification of nanomaterials. The emitted X-rays are measured with an EDX spectrometer. Quantification of the intensities from X-rays from different elements yields the elemental concentration of the sample. Until recently, the technique was not suitable for the detection of light elements ( $Z < 8$ ). However, with the advances of new equipment, the detection range has enlarged which allows one to acquire information from even lighter elements [13]. A new EDX detector, ChemiSTEM SuperX, was introduced by Thermo Fisher company and consists of four silicon drift detectors located in the specimen plane around the specimen. A high count rate and resolution in comparison to conventional Si(Li) detectors yield faster acquisition of the elemental maps.

### 1.2.3.2 Electron energy loss spectroscopy

Another analytical technique used in electron microscopy is electron energy loss spectroscopy (EELS). The energy loss of the transmitted electrons can be detected by the spectrometer which is located at the end of the TEM column. The electrons scattered from the sample are directed into a magnetic field (see Figure 1.4), which disperses the electrons based on the energy and a spectrum is recorded. Typically, there are three different regions on the recorded spectrum: the zero-loss, low-loss (2-50 eV) and core-loss region ( $> 50$  eV) [10, 12, 14]. The zero-loss peak consists of nuclear and quasi-nuclear scattered electrons. The full width half maximum of the zero-loss peak can be used to determine the energy resolution during the experiment. The low-loss region yields information on the plasmon oscillation of the valence electrons in the sample. The core-loss region of the spectrum, contains information on the electron-electron interaction from the inner shells. Chemical information on the sample is obtained using core-loss spectra. EELS with a good energy resolution 150 - 200 meV yields information about the surface plasmon of a metallic nanostructure in low-loss region [15] and valency states of the elements in the nanostructure in the core-loss region [16].

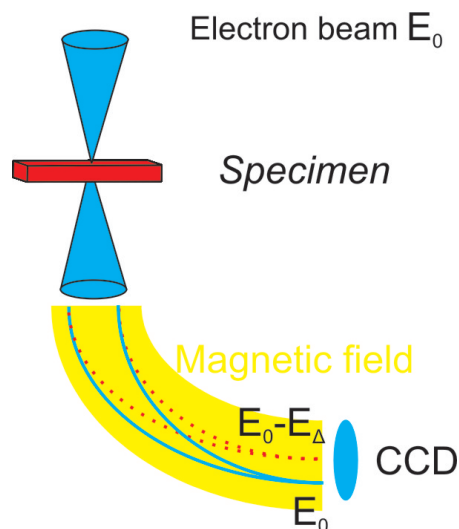


Figure 1.4: Schematic visualization of EELS where electrons with different energy is dispersed using a magnetic field.

## 1.3 Electron tomography

### 1.3.1 General aspects of electron tomography

TEM is an ideal technique to study the structure and morphology of nanomaterials. However, by using conventional TEM, only two dimensional (2D) projections of a 3D object are obtained. 2D projections may be sufficient for the investigation of symmetric nanostructures, but may lead to unreliable results for highly asymmetric nanostructures. For instance, the pore network, distribution and size of porous nanomaterials needs to be investigated in 3D. To perform such 3D studies, electron tomography is required. Electron tomography is a technique where a 3D reconstruction can be retrieved using a tilt series of 2D projection images. In general, an electron tomography experiment consists of four steps: (i) the acquisition of a tilt series of 2D projections, (ii) the alignment of the series, (iii) the reconstruction, (iv) visualization and/or quantification of the 3D structure.

In the first step, a tilt series of projection images of the investigated object is acquired over an angular range that is as large as possible with an acquisition every

$1^\circ$  or  $2^\circ$ . The acquisition is followed by the alignment of the successive images with respect to a common tilt axis. In this step, the relative shifts and rotations between successive images are reduced as much as possible. Afterwards, a mathematical reconstruction algorithm is used to compute the 3D reconstruction. In the last step, the result of the electron tomography experiment is visualized and analyzed. A schematic illustration of electron tomography experiment and reconstruction procedure is presented in Figure 1.5.

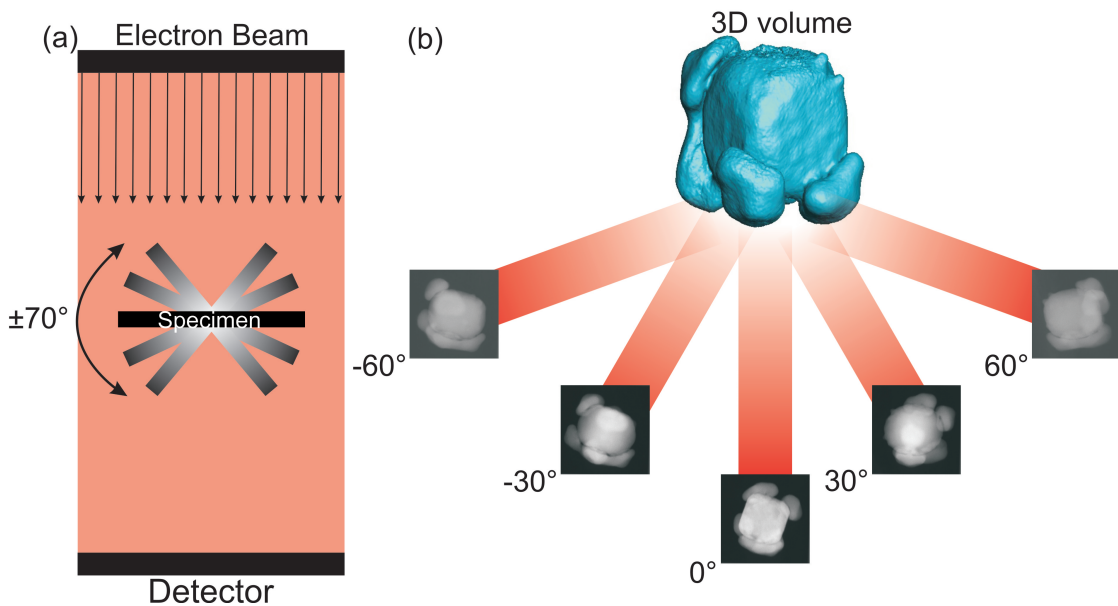


Figure 1.5: (a) Illustration of the tilting procedure (b) the visualization of the 3D reconstruction from an object, the reconstruction is obtained by re-projecting the tilt series using a mathematical algorithm.

### 1.3.2 History of electron tomography

The first study of electron tomography was demonstrated in late 1960s in a paper by Derosier and Klug [17]. In this study, 3D morphological information was retrieved from a single 2D projection. Later, Hoppe [18] showed that the combination of multiple projections from different orientations can be used to reconstruct the morphology. Thereby, the idea of tilt series was introduced where one acquires

a projection around a tilt axis. Since then, electron tomography was developed first in biological applications and later on in materials science. The first application of electron tomography was developed in biology by reconstructing biological macromolecules [19]. The application in physical science is more complicated due to additional problems such as the “projection requirement”. The projection requirement states that to reconstruct the 3D structure of an object from its 2D projections, a monotonic relationship is required between the image intensity and mass-thickness of the investigated sample [20]. In crystalline samples, the presence of diffraction contrast in the projections violates the projection requirement. Hence, BF-TEM imaging is avoided and HAADF-STEM imaging is preferred when investigating nanostructures [20]. A more detailed explanation on the applicability of the image modes which were introduced in section 1.2.1, is presented in the following section.

## 1.4 Practical tomography

### 1.4.1 Acquisition

In the first section, the applicability of different imaging techniques is discussed. Next, different tilt schemes utilized in an electron tomography experiment will be explained.

#### 1.4.1.1 Imaging methods utilized in electron tomography

As discussed in the previous section, the images of a tilt series need to fulfill the projection requirement in order to carry out a reliable electron tomography experiment. Therefore, only a few techniques can be applied. In this thesis, two methods were used and will be explained below.

#### **ADF-STEM and HAADF-STEM imaging**

(HA)ADF-STEM imaging is used extensively in electron tomography when investigating nanostructures [20]. As discussed in section 1.2.1, annular detectors

with different collection angles can be used. In HAADF-STEM imaging, electrons scattered to higher angles are collected, typically with a range of inner and outer collection angle between 50-190 mrad. The intensity of the images is not dependent on the crystallographic orientation, but is thickness and composition dependent and therefore fulfills the projection requirement. Therefore HAADF-STEM became the most commonly used imaging mode in electron tomography experiments of nanostructures. If the detector collects electrons which are scattered between 25-50 mrad, this imaging mode is known as ADF-STEM imaging. This method can be an ideal tool to study amorphous materials or non-crystalline materials such as C-based materials or mesoporous silica in 3D since they cannot be visualized using HAADF detector due to a low scattering to higher angles.

#### 1.4.1.2 Tilt schemes

As discussed in section 1.3.1, during the first step of an electron tomography experiment, a tilt series of projection images is acquired. Therefore, the nanostructure under investigation is tilted with respect to the electron beam by the use of a dedicated tomography holder. The limited space between the pole pieces of the objective lens hinders the tilt range of conventional TEM holders. Projections over  $\pm 40^\circ$  can be recorded using such holders which results in a large “missing wedge” of information. Each projection in a tilt series corresponds to part of the object in Fourier space, hence missing wedge of information leads to under-sampled Fourier transform which results in degraded reconstructions. A more detailed explanation of the relation between the Fourier transform of an object and reconstruction will be provided in section 1.4.3. The presence of missing wedge should be minimized during the acquisition. Therefore, dedicated electron tomography holders are designed which enable one to tilt over  $\pm 80^\circ$ . A comparison between a conventional TEM holder and a tomography holder is presented in Figure 1.6. The holder depicted in Figure 1.6 b enables one to tilt over  $\pm 80^\circ$  which results in a small missing wedge of information. The tilt interval in a tilt series is determined by the beam sensitivity of the investigated material. Typically, a tilt interval of 2-4° is used in electron tomography experiment. The influence of missing wedge on a

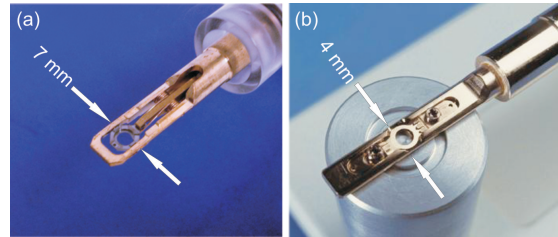


Figure 1.6: (a) A conventional TEM holder and (b) a Fischione model 2020 a single tilt tomography holder.

reconstruction is shown in Figure 1.7 by using a 2D Shepp-Logan phantom. The Shepp-Logan phantom is a standard test image which serves as the model of a human head in the development and testing of image reconstruction algorithms. Phantom objects in different shapes can also be generated using MatLab. Due to the presence of the missing wedge, an elongation of the features in the vertical direction can be observed in the reconstruction. Using dedicated holders, the missing wedge can be minimized down to  $\sim 20^\circ$  and therefore the elongation is reduced in the reconstruction (cf. Figure 1.7 c and d). The acquisition of the tilt

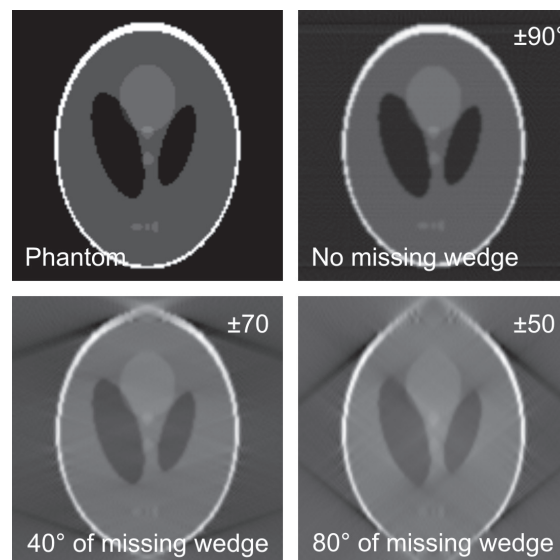


Figure 1.7: Influence of missing wedge in the quality of reconstruction. The tilt range is depicted in the right top edge on the reconstructions.

series can be performed: (i) automatically by the use of a software program or (ii) manually. Explore3D is a commercial software which is used for the acquisition of tilt series. Also different softwares have been developed for this purpose [21–24].

### **Single tilt axis acquisition**

The most commonly used acquisition scheme is the single tilt axis acquisition. Here, a constant angular tilt increment is used over an as large as possible angular range. In some cases, however, thickness variation in slab geometries in the tilt series are corrected by the use of a Saxton step increment where the tilt increment is not constant through the tilt series. In Saxton schemes, the tilt interval is smaller at higher tilt angles and larger at low tilts. Usually less projections are acquired in Saxton scheme which can be an advantage for the characterization of electron beam sensitive materials [25].

### **Dual tilt axis acquisition**

A dual tilt axis acquisition scheme can be used to decrease the missing wedge. After the acquisition of a first tilt series, a second tilt series from a tilt axis orthogonal to the first series is recorded (see Figure 1.8) [26, 27]. Merging the series or reconstructions results in a missing pyramid of information instead of a missing wedge in Fourier space (see Figure 1.8 b) which results in lesser prominent artifacts [26]. In practice, a dual axis acquisition can be obtained by the use of a dedicated holder which can rotate its sample plane. The limitation of this approach is the increase of beam induced damage on the specimen since two tilt series need to be acquired.

### **On-axis tilt axis acquisition**

An alternative acquisition method is called “on-axis tilt”, where a needle shaped sample is tilted over a full range of  $\pm 90^\circ$  by the use of an on-axis tomography holder [28, 29]. The preparation of such needle-shaped sample is performed by the use of a focused ion beam (FIB). The possibility of the acquisition of a full

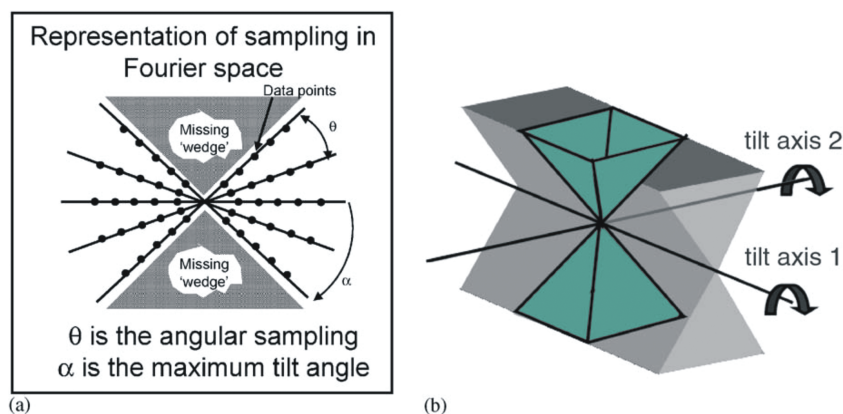


Figure 1.8: (a) The illustration displays the sampling of data in Fourier space. The limited range of tilt leads to a missing wedge (displayed in gray),  $\theta$  here represents the tilt interval and  $\alpha$  the tilt range, (b) the missing wedge is reduced by dual axis tomography to a missing pyramid (shown in green).

range tilt series eliminates any missing wedge artifact and severely improves the quality of the 3D reconstruction. However, the main challenge for this technique is the sample preparation where one needs to avoid ion beam damage during FIB milling. Additionally, the preparation of needle-shaped samples for nanoparticles remains challenging [24].

## 1.4.2 Alignment

After the acquisition of the tilt series, the projections need to be aligned with respect to a common tilt axis. Since tilting the tomography holder during the acquisition is obtained by mechanical rotation, the object may shift vertically and horizontally in the field of view. The investigated structure is therefore tracked back into the field of view after each tilt, which results in remaining shifts between the successive projection images. The alignment procedure after the acquisition includes two steps.

The first step is to correct the lateral and vertical shifts of the object between consecutive projections. This can be done by cross-correlation which is a degree of resemblance of two image as a function of the alteration of one relative to the

other. In Figure 1.9, two successive HAADF-STEM images from a tilt series and their corresponding cross-correlation are depicted. The position of the maximum intensity peak in the cross-correlation image corresponds to the relative shift between the two projections. Usually, this peak intensity is blurred due to noise in the images (see Figure 1.9 c) and therefore applying a filter is useful to extract its position. The cross-correlation peak after image filtering is presented in Figure 1.9 f.

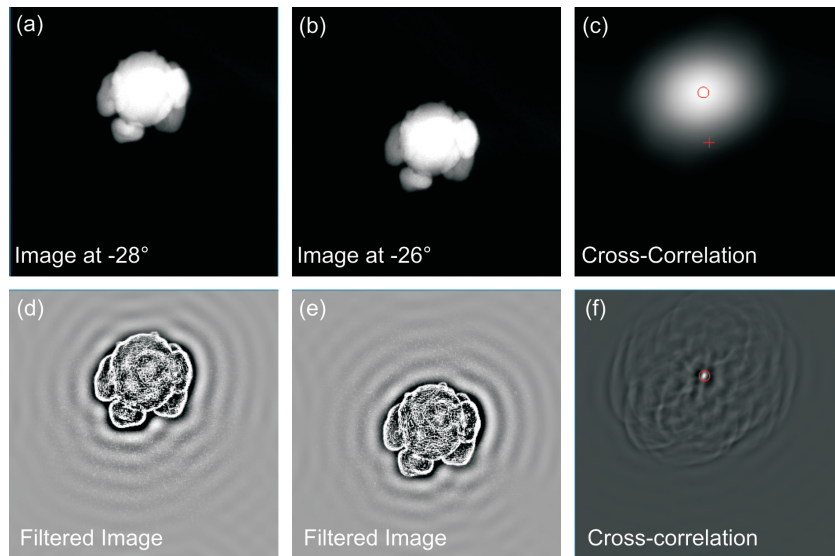


Figure 1.9: Schematic visualization of the cross-correlation process. Two consecutive images of a tilt series are depicted in (a) and (b) and the corresponding cross-correlation peak is presented in (c). The use of a Sobel filter (d-f) enables one to locate the cross-correlation peak in a more reliable manner.

The next step of the alignment is the so-called tilt axis adjustment. In this step, the direction of the tilt axis is adjusted in order to correspond to the experimental tilt axis and to reduce the arc-shaped artifacts in the final reconstruction. In each experimental case in this thesis, the alignment is performed using a commercial program, FEI Inspect3D. Slices through a reconstruction of a misaligned and properly aligned tilt series are given in Figure 1.10. The arc-shaped artifacts are highlighted with blue arrows in (a) and (c).

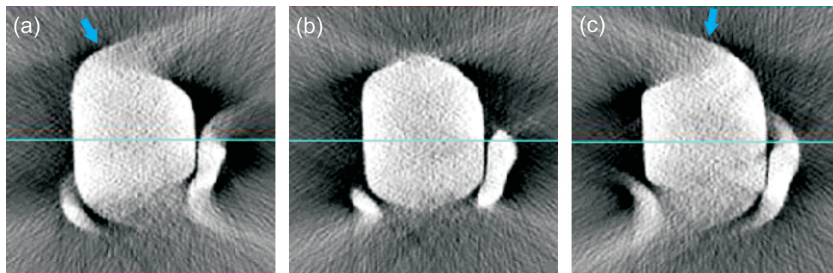


Figure 1.10: Illustration of the effect of misalignment of the tilt axis, for the case of a Au nanoparticle. (a) and (c) slices through a reconstruction in which misalignment is present. (b) Slice through a reconstruction for which the tilt axis adjustment is properly aligned.

### 1.4.3 Reconstruction

Once the tilt series is aligned, it can be used as an input for a reconstruction algorithm. Many reconstruction algorithms are developed. Some of them are generic whereas others are material targeted [30–37]. In this section, first the fundamentals of tomography reconstruction are presented and then the most generic reconstruction algorithms which are used in this thesis are explained.

#### 1.4.3.1 Fundamentals of tomography

The mathematical fundamentals of tomography have been developed by Johan Radon. The Radon transform is explained in the following section.

#### Radon Transform

The Radon transform is the mathematical basis for the tomography techniques introduced in 1917 by Johan Radon [38]. A line integral denotes the integral of some property of an object along a line. In the transform, the object  $f$  is described by a two dimensional function  $f(x, y)$ . Each line integral is represented by  $(t, \theta)$ . The equation of the line  $L$  with a unit length of  $ds$  in Figure 1.11 is given by:

$$P_{\theta}(t) = \int_{L(t\theta)} f(x, y) ds \quad (1.3)$$

where distance to the origin of a line integral  $|t|$  can be expressed by  $|t| = x \cos \theta + y \sin \theta$ :

$$P_{\theta}(t) = \int_{-\infty}^{\infty} \int_{-\infty}^{\infty} f(x, y) \delta(x \cos \theta + y \sin \theta - t) dx dy \quad (1.4)$$

The function  $P_{\theta}(t)$  is the Radon transform of the object. The Radon transform of an object is often referred to as a sinogram because the transform of an off-center point source in real space corresponds to a sine wave in Radon space. The coordinates of the Radon transform of an object  $f(x, y)$  are  $\theta$  and  $|t|$  representing the projection angle and the distance of the projection line with respect to the origin. The turquoise line profile acquired from an arbitrary angle  $\theta$  is shown in Figure 1.11. By acquiring more projection images, a higher sampling of the sinogram is achieved. The stack of all projections from different tilt angles is presented in Figure 1.11 b. If the object is imaged along all projections, then the inverse Radon transform yields the original object.

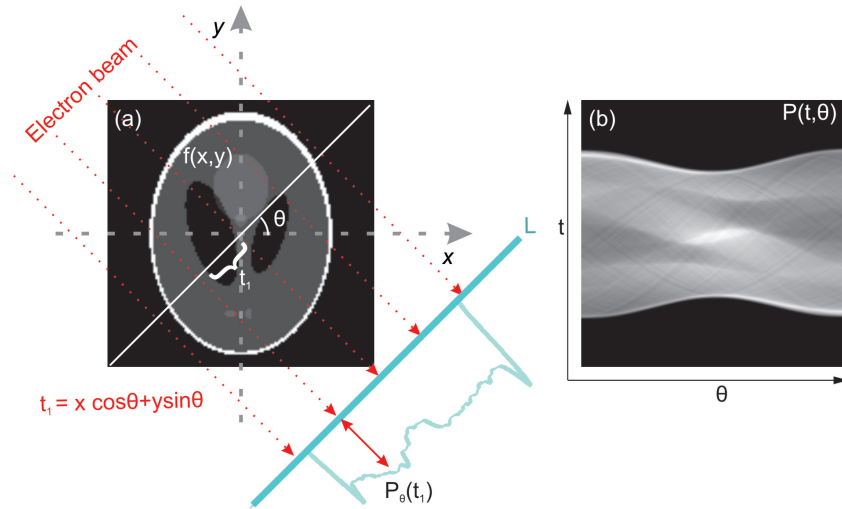


Figure 1.11: (a) An object and its line integral is given, (b) the stack of Radon transforms of the object for a given projection angle  $\theta$ .

**The Fourier slice theorem**

The Fourier slice theorem states that the 1D Fourier transform of a projection of a 2D object equals a line through the 2D Fourier transform of the imaged object [39]. By summing all these lines in Fourier space, and calculating the inverse Fourier transform the tomographic reconstruction of the object is obtained [39]. The Fourier transform of a 2D object  $f(x,y)$  equals:

$$F(u, v) = \int_{-\infty}^{\infty} \int_{-\infty}^{\infty} f(x, y) e^{-2\pi i(ux+vy)} \quad (1.5)$$

where  $u = w \cos \theta$  and  $v = w \sin \theta$ , likewise a projection at angle  $\theta$  can be defined as  $P_{\theta}(t)$  and its Fourier transform is:

$$S_{\theta}(w) = \int_{-\infty}^{\infty} P_{\theta}(t) e^{-2\pi i w t} dt \quad (1.6)$$

A simple case is obtained when the projection angle is  $\theta = 0$ . The Fourier transform of the object along the line in the frequency domain is given by  $v = 0$ :

$$F(u, 0) = \int_{-\infty}^{\infty} \int_{-\infty}^{\infty} f(x, y) e^{-2\pi i u x} dx dy \quad (1.7)$$

Since the phase factor no longer depends on  $y$ , the integral can be written as:

$$F(u, 0) = \int_{-\infty}^{\infty} \left[ \int_{-\infty}^{\infty} f(x, y) dy \right] e^{-2\pi i u x} dx \quad (1.8)$$

The term in the brackets equals to a projection along lines of constant  $x$ :

$$P_{\theta=0}(x) = \int_{-\infty}^{\infty} f(x, y) dy \quad (1.9)$$

Substituting Equation 1.9 in Equation 1.8 leads to:

$$F(u, 0) = \int_{-\infty}^{\infty} P_{\theta=0}(x) e^{-2\pi i u x} \quad (1.10)$$

Since the right hand side of the equation Equation 1.10 depicts the one dimensional Fourier transform of the projection  $P_{\theta} = 0$ , the following correspondence between the projection and the 2D Fourier transform of the object is obtained:

$$F(u, 0) = S_{\theta=0}(u) \quad (1.11)$$

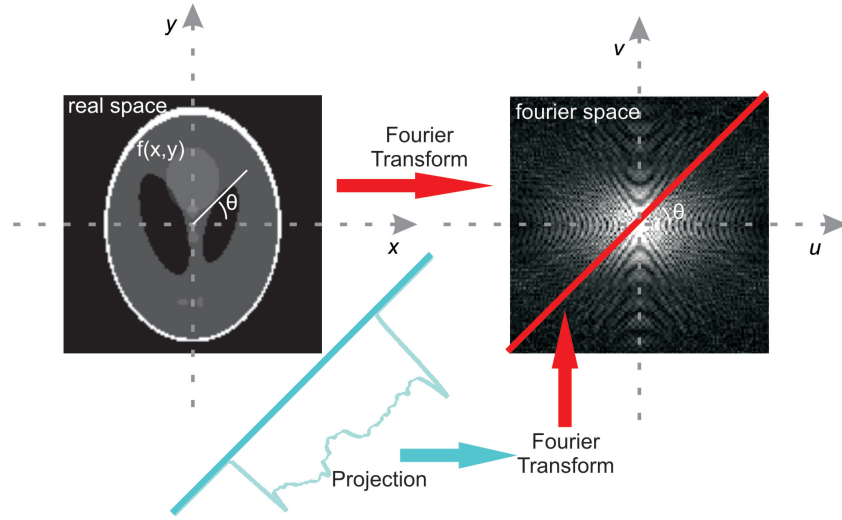


Figure 1.12: Schematic illustration of Fourier slice theorem.

Since the result is independent of the orientation between the object and the coordinate system, this result establishes the basis of the Fourier slice theorem. An object can be reconstructed using:

$$f(x, y) = \int_{-\infty}^{\infty} \int_{-\infty}^{\infty} F(u, v) e^{-2\pi i(ux+uv)} dudv \quad (1.12)$$

For a reconstruction in Fourier space, an infinite number of projections or interpolation in Fourier space is required which is both practically very difficult [40]. The application of this methodology is therefore limited. A schematic illustration of the Fourier slice theorem is presented in Figure 1.12.

### 1.4.3.2 Reconstruction algorithms

#### Back-projection

A common reconstruction method that is often used in biology and materials is “back-projection”. The basic concept of back-projecting is smearing out the intensity distribution of a projection along the angle under which it was acquired [41]. The summation of the back-projected lines (rays) leads to a reconstruction

of the original object if a sufficient number of projections is available. Unfortunately, back-projection results in blurry reconstructions due to the enhancement of the low frequencies (see Figure 1.13 b). In this reconstruction, 180 projections were acquired from the phantom image, shown in Figure 1.13 a. The blurring can be overcome by filtering each projection column with a ramp-like filter in Fourier space. This procedure is called weighted back-projection (WBP) [42]. The resulting reconstruction obtained using WBP reconstruction is presented in Figure 1.13 b.

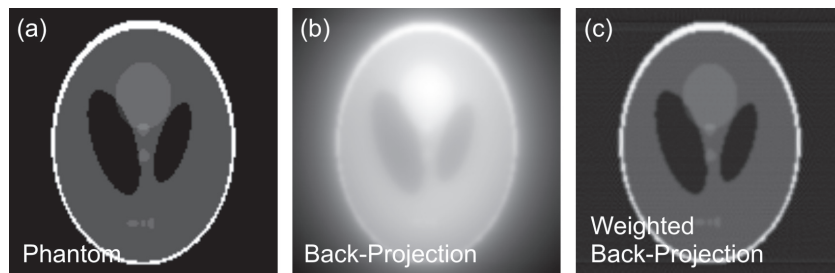


Figure 1.13: (a) the phantom object (b) reconstruction using back-projecting and (c) WBP.

### Simultaneous Iterative Reconstruction Technique

In practical electron tomography, a limited number of projections is acquired, with an acquisition of a projection image typically every  $2^\circ$  or  $3^\circ$ . Therefore, the use of back-projection is less favorable since a high sampling of the object is required. Instead, iterative reconstruction methods are used and the most common one is the simultaneous iterative reconstruction technique (SIRT) algorithm. SIRT is preferred in materials science although it requires higher computational weight in comparison to WBP due to its robustness to noise in the projections. The projection equation is given by:

$$Ax = b \tag{1.13}$$

Here, the projection matrix is denoted by  $A$ ,  $x$  is the object to be reconstructed and  $b$  is the measured projections:

$$\hat{x} = \operatorname{argmin}_x \left[ \frac{\mu}{2} \|Ax - b\|_2^2 \right] \quad (1.14)$$

The difference of forward projection of an intermediate reconstructions and the measured projections is minimized using iterative methods [42]. In the first iteration, a reconstruction using the BP principle is performed, then the obtained reconstruction is reprojected along the original projection angles. These re-projections are compared to the measured projection images and used to improve the reconstruction. Subtracting the re-projections from the measured projection images yields “difference projections”. Based on the difference projections, a difference reconstruction is calculated which is then added (or multiplied) to the first reconstruction (as it is the first iteration). This procedure is repeated iteratively until the difference between a reconstruction and the original projections reaches a minimum. A schematic flowchart of SIRT method is displayed in Figure 1.14. A recent study showed that 30 iterations are typically required to reach this minimum [43]. SIRT is one of the most broadly used reconstruction algorithm in materials science and it establishes the basis of different reconstruction algorithms such as discrete algebraic reconstruction algorithm [31] and total variation minimization [34].

### Total Variation Minimization

Total variation minimization (TVM) is an iterative method which is based on compressed sensing where it is assumed that the signal (object) to be reconstructed has a sparse representation in some basis [34, 44, 45]. The algorithm attempts to find a solution to the reconstruction problem  $Ax = b$  by minimizing the total variation. This is achieved by minimizing the norm of the total variation and minimizing the total projection distance simultaneously [34, 44]:

$$\hat{x} = \operatorname{argmin}_x [\lambda TV(x) + \|Ax - b\|_2^2] \quad (1.15)$$

Here  $TV(x)$  is a particular l1-norm applied to the gradient of the reconstructed object,  $\lambda$  is the regularization parameter and  $\|Ax - b\|_2^2$  is the projection distance

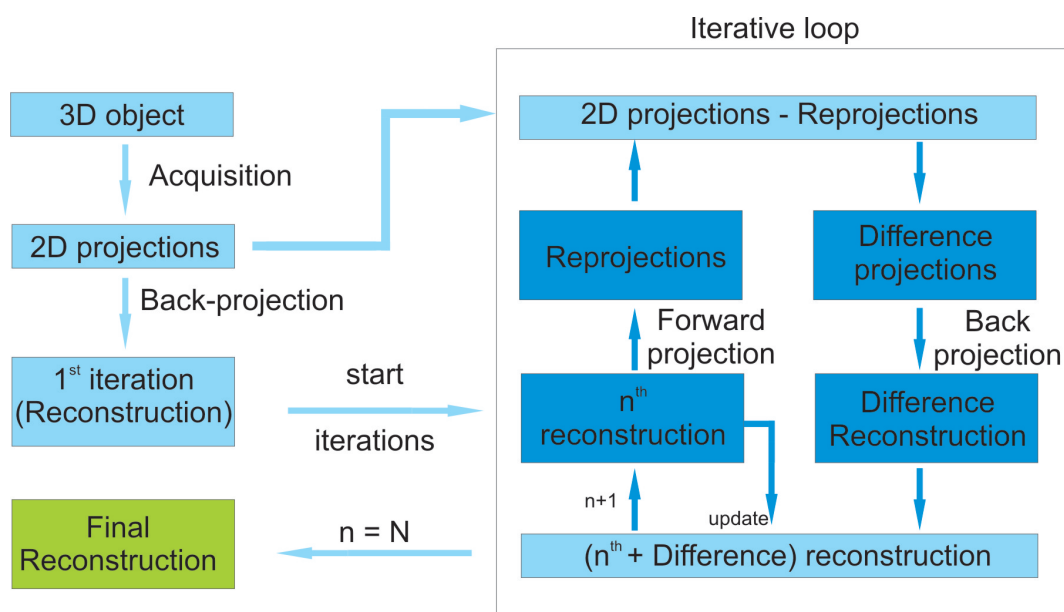


Figure 1.14: Flowchart displaying the principle of the SIRT with N iterations.

which represents the difference between the experimental projection images and the re-projections of the intermediate 3D reconstruction. If  $\lambda$  is zero, the equation becomes identical to the Equation 1.14 which yields a SIRT reconstruction. Simulation studies showed that  $\lambda = 0.5$  is a good starting value [34]. An appropriate value of  $\lambda$  will reduce the missing wedge artifacts in a significant manner. Figure 1.15 shows a comparison between different reconstruction algorithm.

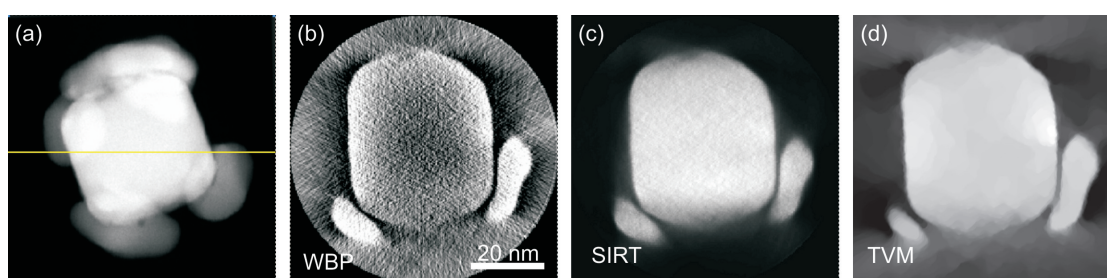


Figure 1.15: (a) HAADF-STEM image of a Au nanoparticle, the line indicates where the slices through the reconstruction were acquired. Slice through the 3D reconstruction of the object using (b) WBP, (c) SIRT, (d) TVM ( $\lambda = 0.5$ ).

## 1.4.4 Visualization of electron tomography 3D tomogram

In the final step of an electron tomography experiment, the 3D reconstruction needs to be visualized and interpreted. A reconstruction can be visualized using three main methods which are isosurface rendering, voltex rendering and orthoslices.

### 1.4.4.1 Isosurface Rendering

An isosurface rendering displays the surface of a 3D reconstruction by connecting the voxels with a similar gray value. A voxel corresponds to a single data point on a 3D grid. The general morphology of the investigated object can be visualized in this manner. In Figure 1.16 examples of two isosurface renderings using the opaque (a) and the transparent (b) visualization mode.

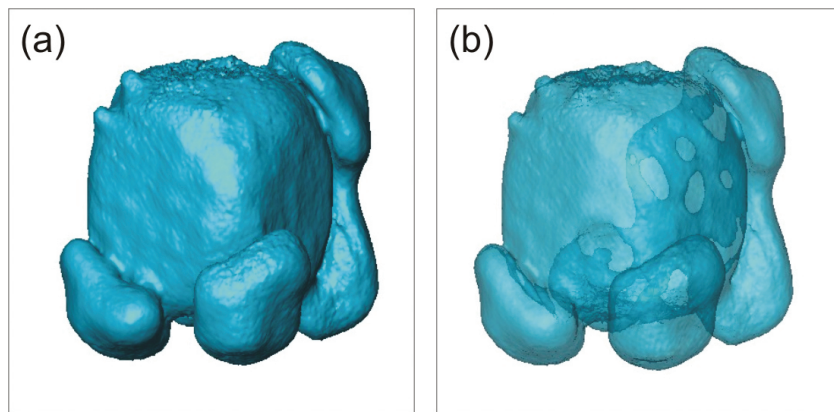


Figure 1.16: Isosurface rendering of an Au nanoparticle showing an (a) opaque and a (b) transparent isosurface.

### 1.4.4.2 Voltex Rendering

An advantage of voltex rendering over isosurface rendering is that instead of visualizing a constant intensity value, a range of intensity values is presented on the screen. This yields a global overview of the morphology of the specimen and visualizes the internal intensity variations. Visualizations of reconstructions from

different multi functional nanoparticles are displayed in Figure 1.17. The plasmonic Au nanoparticles at the cores are displayed in isosurface mode and the shells are displayed using vortex rendering.

#### 1.4.4.3 Orthoslice

A 3D reconstruction of an object corresponds to a stack of 2D slices. It is therefore possible to visualize and analyze single 2D slices through the reconstructed object. These slices are called “orthoslices”. Orthoslice visualization is the most objective way of visualizing the reconstruction in comparison to the rendering methods, since no parameter or threshold has to be defined. Examples of orthoslices obtained using different reconstruction algorithms were for example presented in Figure 1.15 b-d.

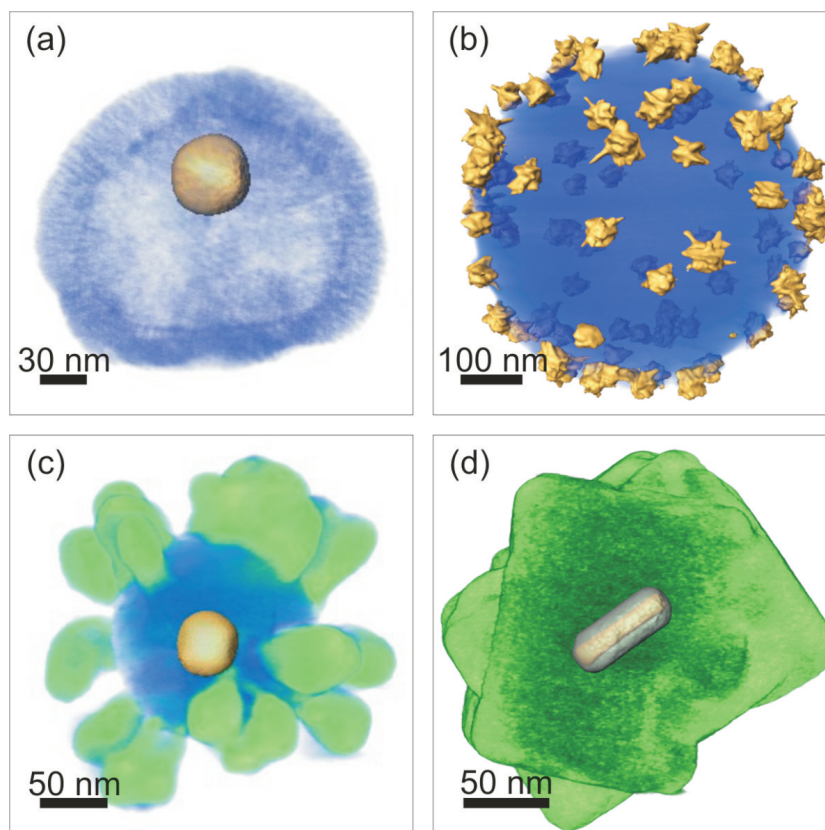


Figure 1.17: Isosurface rendering and voltex visualization of nanoparticles made of different components. a) Au-polystyrene-mesoporous SiO<sub>2</sub>, b) Au nanostars dispersed on polystyrene, c) Au nanoparticle encapsulated with polystyrene and SiO<sub>2</sub>, d) Au@Ag@ZIF-8 nanoparticle.

## Chapter 2

# Application of Electron Tomography for Characterization of Plasmonic Nanoparticles

**This chapter is based on:**

Y. Wang, A.B. Serrano, K. Sentosun, S. Bals, L.M. Liz-Marzan, Stabilization and Encapsulation of Gold Nanostars Mediated by Dithiols, *Small*, 11(34), (2015), 4314-4320

Y. Wang, K. Sentosun, A. Li, M. Coronado-Puchau, A. Sanchez-Iglesias, S. Li, X. Su, S. Bals, L.M. Liz-Marzan, Engineering structural diversity in gold nanocrystals by ligand-mediated interface control, *Chemistry of Materials*, 27(23), (2015), 8032-8040

In this chapter, the structural characterization of plasmonic Au nanoparticles is presented. The synthesis of the samples and optical characterization is carried out at Bionanoplasmonics Laboratory, CIC biomaGUNE in Spain. I was responsible for all 2D and 3D TEM investigations.

## 2.1 Introduction to Plasmonic nanoparticles

Plasmonic properties are observed mainly in metals where their interaction with electromagnetic radiation leads to a collective oscillation of conductive electrons at resonant frequency. When the wavelength of the incoming light is at the order of the metallic nanoparticle size and the oscillations are confined on the metal surface at a metallic-dielectric interface, local free electron oscillations occur, which are known as localized surface plasmon resonances (LSPR) [46]. Thanks to their particular characteristics, plasmonic nanoparticles are of interest for a broad range of applications, from optoelectronics to biomedicine [47]. Plasmonic nanoparticles can absorb or scatter light depending on their shape and size [48]. The optical properties of these nanostructures can be measured using an UV-Visible spectroscopy and Fourier-transform infrared spectroscopy. In general, when the diameter of a spherical nanoparticle is smaller than 40 nm, the nanoparticle absorbs the electromagnetic radiation. This results in elevation in local temperature due to electron phonon interactions. Hence, such nanoparticles can be used for the destruction of cancer cells known as hyperthermic cancer therapy (bottom row left and right side in Figure 2.1) [49]. On the other hand, for larger nanoparticles, scattering dominates over absorption. The incoming light is scattered from the Au nanoparticles with a certain wavelength [47]. In this manner, the tracking of individual Au nanoparticles is possible [50, 51]. Such nanoparticles with scattering property can be used as contrast agents in imaging applications (top and bottom right side in Figure 2.1) [50]. Moreover, nanoparticles with large scattering cross-sections are used to enhance the Raman signal of molecules in their proximity (Figure 2.1 center and top left) which is known as surface enhanced Raman scattering (SERS) [52–54]. The SERS enhancement is based on two mechanisms: a chemical and an electromagnetic mechanism. The chemical enhancement is obtained by chemisorption of the molecule on the metal surface and typically increases the signal by a factor of  $10^2$ . The electromagnetic enhancement is wavelength dependent, arising from the excitation of LSPRs, which yields a SERS enhancement factor of approximately  $10^6$  to  $10^8$  for a variety of molecules. This significant SERS enhancement

can be exploited for biomedical applications. Au and Ag nanoparticles are suitable candidates since they exhibit an increased SERS intensity by an electromagnetic enhancement due to LSPR at the metal surface which is coupled with the molecule. The electric field enhancement is most effective at sharp corners, edges and narrow gaps [55, 56] and also in so-called hot spots [57]. Hot spots are generated when two plasmonic nanostructures are in close interaction or form a junction or a dimer. SERS enhancement based on hot spots yields an intensity increment by a factor of  $10^6$ . In particular, Au nanoparticles with sharp tips (i.e. Au nanostars) or particles in close contact are particularly suitable for SERS. Since the plasmonic properties are highly dependent on the morphology and composition, a thorough structural characterization in 3D is of utmost importance. Metals such as Au, Ag, Cu, Al but also semiconductors, chalcogenides and graphene exhibit plasmonic properties [58–62]. In this thesis, Au, Au-Ag and CuTe nanoparticles are studied. A brief introduction for Au nanoparticles is provided in the following section. An overview of CuTe nanoparticles is discussed in chapter 3 and Au-Ag nanoparticles in chapter 6.

### **Au nanoparticles**

Au nanoparticles are particularly suitable candidates for applications such as bioimaging and photo-thermal therapy (see Figure 2.1). The synthesis of Au nanoparticles is mainly carried out by a two step procedure which is referred to as “seed mediated growth” [63, 64]. During the nucleation step, uniform, mainly spherical Au seeds are obtained, which will serve as nucleation points for further growth. This first step occurs very fast and therefore limited control over the shape is obtained. In the next step, the reaction conditions are opposite to the nucleation step, since a high control over the shape is desired [65]. Hereby, Au ions, reductants and surfactants are added to the solution. The growth of Au nanoparticles with different shapes is controlled by using different surfactants which will promote a particular shape. For instance, cetyltrimethylammonium bromide (CTAB) is particularly efficient as directing agent for the synthesis of Au nanoparticles with different shapes, such as nanorods, stars, and plates [65].

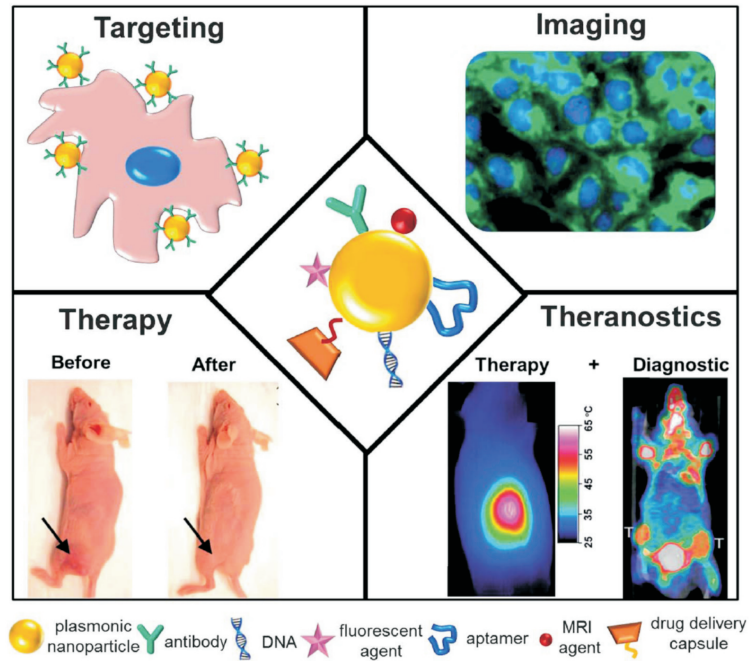


Figure 2.1: Illustration of multiple therapeutic and diagnostic applications using plasmonic nanoparticles (center) for targeting cancer cells via antibodies on the nanostructure surface (top left), for cancer cell imaging (top right), for cancer treatment showing complete eradication of tumor in mice after photothermal therapy (bottom left), and for theranostics which enables a single plasmonic entity to deliver both therapeutic and diagnostic functionalities (bottom right) [49].

CTAB's chloride counterpart, cetyltrimethylammonium chloride (CTAC) has also been implemented in the synthesis of Au particles, which resulted in morphologies such as concave cubes, trisoctahedra, or rhombic dodecahedra [66–70]. In Figure 2.2 an overview of different morphologies of Au nanoparticles is presented.

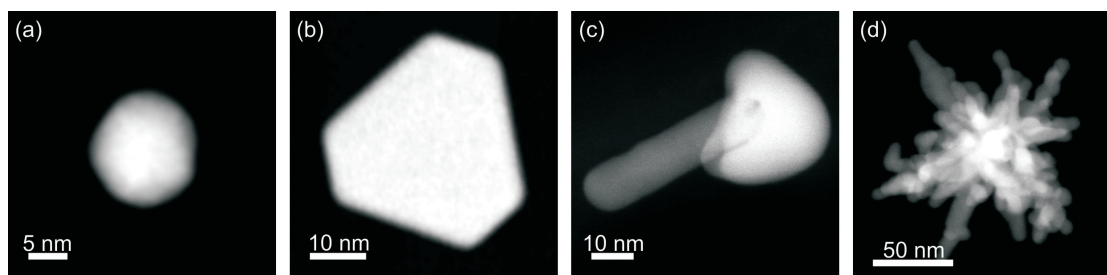


Figure 2.2: Anisotropic Au nanoparticles in different morphology which are recorded using a TEM.

Although Au nanoparticles can be prepared with almost any desired shape, the fundamental mechanisms behind the shape control are not well understood. Therefore, different synthesis methods and their obtained growth mechanism are studied. In this chapter, Au nanoparticles for SERS application are investigated. As explained in section 2.1, the plasmonic properties are dependent on the shape and size of the nanoparticles. TEM images only form a 2D projection of a 3D object, and may in some cases be misleading. Hence, 3D characterization by electron tomography is required.

## 2.2 Encapsulation of Au nanostars via seeded growth

Colloidal metal nanoparticles with various shapes are of interest for applications exploiting their plasmonic properties. Among a variety of possible nanoparticle morphologies, colloidal Au nanostars comprising a central core from which multiple sharp branches protrude, have been pinpointed as highly efficient SERS substrates due to their tunable LSPR and nanoantenna effects by controlling core size, along with tip length and sharpness [55, 56, 63, 64, 71–74].

A number of methods have been reported for the synthesis of Au nanostars, through either seedless or seed-mediated approaches, using capping molecules such as poly( N-vinylpyrrolidone) (PVP) or CTAB, but also under surfactant-free conditions [63, 64, 75–77]. Whereas PVP-capped Au nanostars can be synthesized with tailored dimensions and optical properties [63, 78], and used for ultrasensitive SERS detection [79], the SERS signal is affected by hindered analyte chemisorption due to the adsorbed polymer, which can be removed only via a time consuming process [56]. As an alternative, surfactant-free Au nanostars are of high interest considering that their cleaner surfaces are more suitable for surface functionalization, additionally avoiding toxicity issues derived from the surfactant [77, 80]. However, these Au nanostars typically display poor stability, resulting in changes of morphology and corresponding LSPR blue-shifts, which has also been reported for other nanostructures with sharp tips [81, 82]. In the absence of capping molecules, colloidal stability is also compromised, as Van der Waals attractions become dominant, eventually leading to particle aggregation [83]. These observations clearly indicate that the surface properties of Au nanostars play a critical role on the colloidal and chemical stability, which is crucial for SERS relevant applications [84].

Various strategies have been developed to functionalize the Au nanostar surface, so as to mediate the interaction of the nanoparticles with target analytes toward practical SERS applications [84]. For instance, the introduction of capping molecules such as polymer stabilizers [63], thiolated polyethylene glycol [77], surfactants [85, 86], and proteins such as bovine serum albumin [86], as well as protective inorganic shells [87, 88], were used to improve colloidal stability prior to eventual application. A conceptually different strategy concerns the use of reduced graphene oxide as support, with no need for additional polymer stabilizer or surfactant during Au nanostar synthesis [83]. Alternatively, an additional near infrared dye layer and bovine serum albumin coated on the Au nanostar surface has been recently employed to develop stable SERS probes [85]. In addition, nanostar templated Ag overgrowth produces hybrid particles and enables stronger SERS signal upon adsorption of Raman tags on the outer surface. However, few attempts have

been directed towards incorporating the Raman tag between metal layers within the same particle, so as to generate plasmonic hot spots for the development of highly efficient SERS probes [89, 90].

Here, high resolution HAADF-STEM and electron tomography are used to study the growth mechanism of a new synthesis approach further explained in Wang et al. [91], a Raman tag 1,4-benzenedithiol (BDT) is used together with CTAC to stabilize the Au surface. Au nanoparticle seeds with different size and shapes and varying  $R = [\text{Au}^{3+}] / [\text{Au}^0]$  ratio are investigated with the aim of enhancing the Raman scattering. The  $R$  value here corresponds to the ratio of  $\text{Au}^{3+}$  ions added to the solution during the synthesis and metallic  $\text{Au}^0$  corresponds to the seeds. For each type of seed, three samples were prepared with different  $R$  values.

BDT-modified Au nanostars are used as seeds to direct further encapsulation within Au shells, considering that the strong binding between thiol groups and reduced Au atoms should affect the shell growth mode. A schematic overview of the synthesis procedure is presented in Figure 2.3 a. First, a Au nanoparticle is capped with CTAC and BDT. Then, the overgrowth of a Au shell around the seed is performed by chemical reduction of different amounts of  $\text{HAuCl}_4$  using ascorbic acid leading to different  $R$  values.

In Figure 2.3 b-d, BF-TEM images of Au nanostructures with 3 different concentration ratios  $R$  of 4.8, 9.6, 19.1, respectively are shown. From these images, it is clear that standard seeded growth did not occur but instead a series of exotic Au nanostructures are obtained. The Au nanostar which is used as a seed is highlighted with an arrow in Figure 2.3 b and c. The growth characteristic of the Au nanostructure seems to be different for larger  $R$  values. Indeed, the corresponding TEM images in Figure 2.3 b, c and d indicate that for increasing  $R$  values the Au nanostars seem to be gradually encapsulated within an external Au shell. Furthermore, the particles are investigated using HAADF-STEM imaging, of which the results are presented in Figure 2.4. Investigating these nanostructures with HAADF-STEM shows the presence of low intensity regions, which are highlighted with arrows in Figure 2.4 b and c.

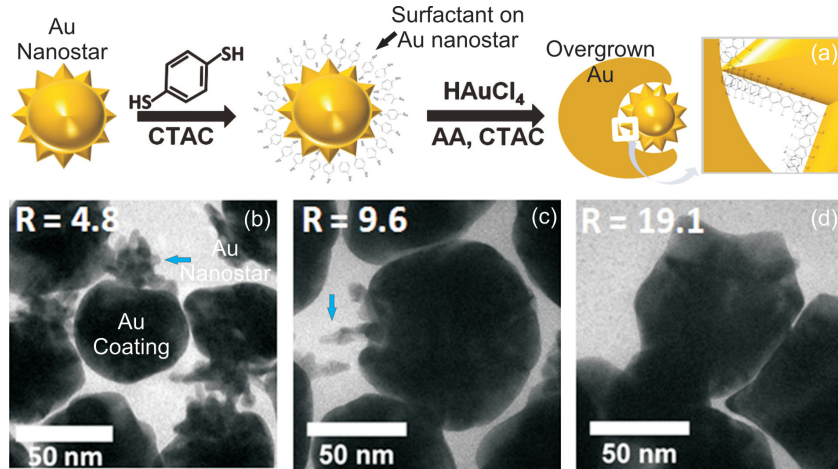


Figure 2.3: (a) Schematic illustration of the expected seeded growth, where CTAC acts as surfactant. (b-d) BF-TEM images of representative Au nanostructures formed by reduction at different R values.

For  $R = 4.8$  (Figure 2.4 a), the nanostructure is attached to the Au nanostar from one side and forms a quasi-spherical nanoparticle resulting in a dimer morphology. When the  $\text{Au}^{3+}$  ion concentration ( $R$ ) in the colloidal solution is increased, the volume of the shell also increases. The shell partially encapsulates the Au nanostar for  $R = 9.6$  (Figure 2.4 b) and an entire encapsulation is observed for  $R = 19.1$  (Figure 2.4 c), resulting in semi-shell and full-shell morphologies, respectively. Since the intensity of a HAADF-STEM image scales with the variation in thickness, the low intensity regions could indicate the presence of internal gaps in the nanostructures. As the observed morphologies are quite intriguing, HAADF-STEM tomography was performed to reveal the 3D morphology of the coated particles, so as to discern potential internal gaps and connecting bridges between the Au nanostar seed and the shell.

For each sample with different R value, three electron tomography experiments were performed by acquiring projections over a tilt range of  $\pm 74^\circ$  with a tilt increment of  $3^\circ$ . A FEI Tecnai G2 microscope operated at 200kV and Fischione 2020 single tilt tomography holder were used for the experiment. The tilt series were aligned using FEI Inspec3D [21] and were reconstructed using the SIRT im-

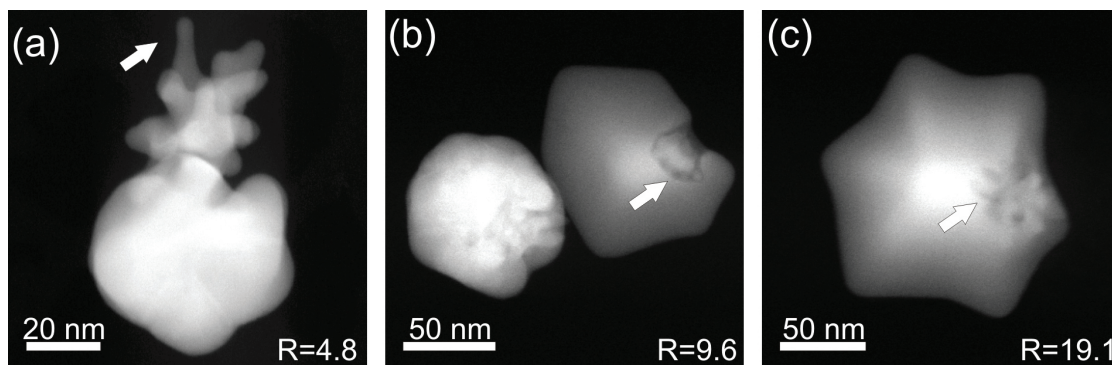


Figure 2.4: HAADF-STEM images from Au nanoparticles showing the influence of the different ratio of reduced Au atoms on shell morphology. (a) Au nanostar with a quasi-spherical nanoparticle is shown. The arrow shows a spike from the Au nanostar, (b) and (c) Au nanoparticles with different R value, the arrows highlight the low intensity regions on the nanocrystal.

plementation of the ASTRA-Toolbox [92]. Representative visualizations from the 3D reconstructions for three samples with increasing R values are shown in Figure 2.5, which confirms the exotic shape of these nanostructures. Investigating the visualization of the 3D reconstruction and the orthoslices from the reconstruction of the sample with  $R = 9.6$  and  $19.1$  confirms the presence of internal gaps (see Figure 2.5 b and c). Moreover, the visualization of the reconstruction displays the internal gaps as bubble-like regions highlighted with an arrow (Figure 2.6 a). The internal gaps can be clearly observed in the 2D orthoslice, as dark regions between the seed and shell (Figure 2.6 b), while the same image also shows the presence of linking bridges between the Au nanostar seed and the shell. An estimate of the internal gap distances from electron tomography images yielded an average value of 4.5 nm. Furthermore, electron tomography confirmed that the seed was not located at the center of the encapsulated shell but rather at the edge, indicating that the shell growth started from one or more of the Au nanostar tips and then asymmetrically continued, gradually surrounding the seed. Further information regarding the growth pathway of the shell on Au nanostar was provided by the crystal orientation which was investigated by high resolution HAADF-STEM

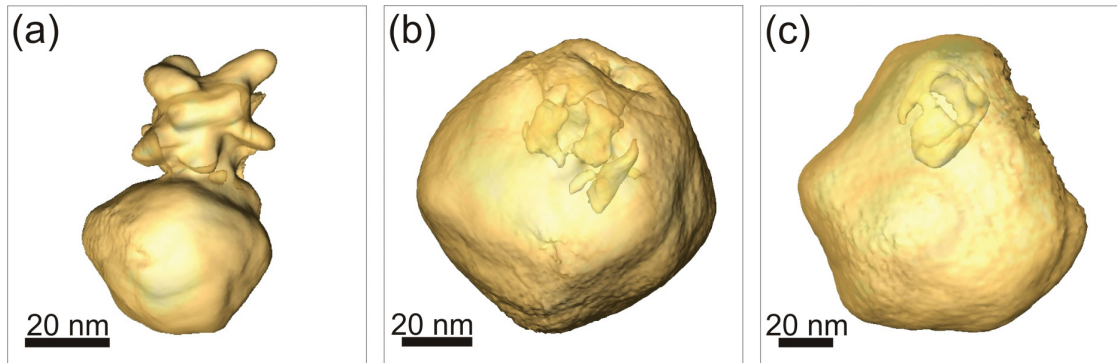


Figure 2.5: Visualization of 3D reconstructions of core-shell Au nanostars with increasing R values: (a) Au nanostar-sphere dimer ( $R = 4.8$ ), (b) semi-shell coated Au nanostar ( $R = 9.6$ ), (c) completely encapsulated Au nanostar ( $R = 19.1$ ).

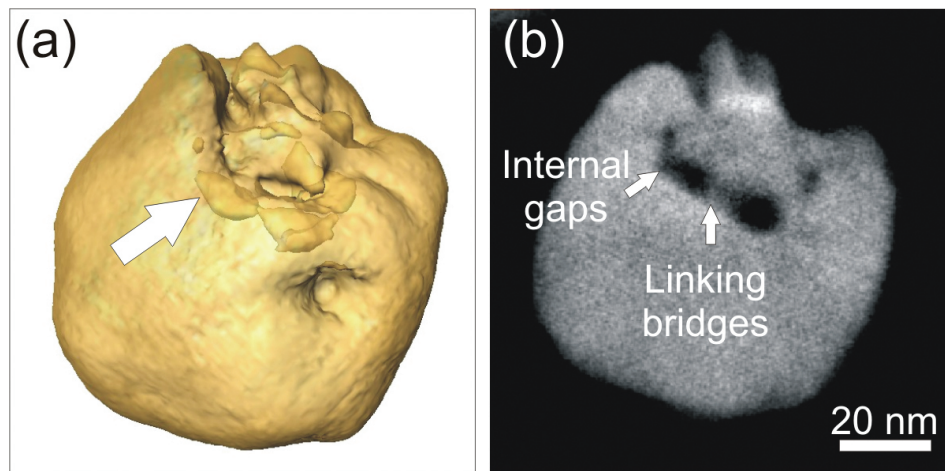


Figure 2.6: (a) 3D rendering of an electron tomography reconstruction for a semi-shell covered Au nanostar ( $\sim 23$  nm core size,  $R = 9.6$ ). The gaps between the nanostar seed and the semi-shell can be clearly identified (example indicated by an arrow). (b) A slice through the reconstruction reveals both the connections and gaps between seed and shell.

imaging. HAADF-STEM images were obtained using an aberration corrected FEI Titan 50-80 microscope operated at 300 kV. High resolution images and their corresponding Fourier transform (FT) patterns which are obtained from 6 different positions on a semi-shell coated Au nanostar (Figure 2.7), revealed that the crystal orientations are not identical, meaning that we tilted the particle to a different zone axis for each of the high-resolution image. This observation indicates that the growth of the shell may start from more than one spot on the original Au nanostar (likely several tips). It should however be noted that overlapping regions between parts of the seed and shell make it difficult to precisely determine where on the seed, the shell growth started. Compared with previous work on core-shell particles with internal gaps mediated by ligands, such as DNA [93–95], block copolymers [90] or other small molecules [89, 96], we show this type of seeded growth at atomic resolution and in 3D, which helps us to better understand this unusual growth mode.

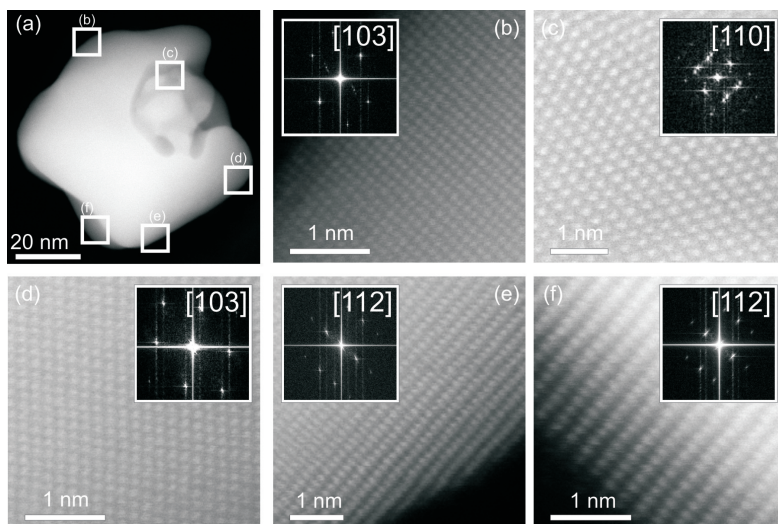


Figure 2.7: (a) HAADF-STEM image providing an overview of a semi-shell coated Au nanostar and (b-f) high-resolution HAADF-STEM images acquired from several regions are highlighted in (a). The corresponding FT patterns of the high-resolution HAADF-STEM images are displayed in the insets.

### 2.2.1 SERS performance of coated Au nanostars

One of the attractive features of this intriguing morphology is the presence of internal gaps. These are likely to display enhanced electric fields, thereby acting as intrinsic hot spots for SERS. Raman Tag BDT molecules should be located precisely at the gaps between the Au nanostar core and the outer shell. Since BDT has a reasonably high Raman scattering cross section [97], intensity increment in the SERS signal is expected. SERS spectra by our collaborators (CIC biomAGUNE, San Sebastian) are collected with an excitation wavelength of 785 nm. A gradual increase of the SERS intensity was observed up to an R value of 9.6, which yields a four-fold higher intensity as compared to the bare Au nanostar seeds (R = 0). For R = 4.8, a  $\sim 3$ -fold higher intensity in SERS is observed, while for R = 19.1 the enhancement is  $\sim 2.5$  fold is observed. Thereby, a clear decrease in SERS intensity is observed for R values above 9.6. Interestingly, the maximum SERS intensity does not correspond to fully coated Au nanostar, even though we should have the largest number of available molecular nanogaps between the core and the shell. This may be due to damping of light transmission through the outer shell or to additional contributions to E-field enhancement in anisotropic morphologies such as partly coated Au nanostar. It thus appears that the morphology yielding the highest SERS intensity is the semi-shell coated nanostar. It is well known that nanostructures comprising sharp tips generate intense electric near field by concentrating light onto the tips (“nanoantenna effect”), which leads to a significant SERS enhancement [55, 98, 99]. In the case of semi-shell coated Au nanostar, the semi-shell may direct the light toward the exposed core tips, further contributing to the overall near field enhancement.

The roles of bifunctional ligand and surfactant in the Au nanostar-seeded growth are thus: (i) protecting the initial Au nanostars from reshaping and aggregation, (ii) directing Au shell growth around the core, and (iii) generating significantly enhanced SERS activity.

## 2.2.2 Growth of Diverse Au nanostructures

To further understand the BDT-ligand mediated core-shell growth, BDT coated spherical, triangle and rod shape Au nanocrystals are used as seeds and overgrown at different R values. To study the morphology and to locate possible internal gaps, electron tomography experiments are performed on different Au nanostructures. In Figure 2.8, 2.9 and 2.10, the 3D visualizations and 2D orthoslices through the reconstructions of various Au nanostructures using different R values are displayed.

The seeded growth mediated by BDT leads to a structural evolution from quasi-spherical Au nanocrystals that are used as seeds and grown at different R ratios ( $R = 0.6, 2.3, 11.7$ ) are shown in Figure 2.8 a-f. When higher R values are used, an evolution of the nanoparticle morphology is observed including semi-shells ( $R = 2.3$ ) and full-shells ( $R = 11.7$ ). Interestingly, bubble-like regions are consistently found (especially for full-shells), indicating the presence of a gap between the seed core and the shell (highlighted with arrows in Figure 2.8 b and c). Such detailed 3D reconstructions obtained by electron tomography allowed us to obtain information on the inner part of the nanostructures (Figure 2.8 e), which clearly revealed the presence of such internal gaps between the BDT-modified seed cores and the grown Au shells. Whereas for  $R = 0.6$  core and shell is in full contact, for  $R = 2.3$  extensive contact but also small nanogaps are found, and for  $R = 11.7$  smaller contact areas and larger nanogaps are present.

Further inspection of the 3D reconstructions indicates that the Au shells are not homogeneously coated around the core, i.e. shell growth occurs in a non-conformal manner. As discussed in section 2.2.1, the presence of internal gaps can largely enhance Raman scattering. On the other hand, the fully coated particles also display lower SERS intensity than that of the semi-shell, in spite of containing more available plasmonic nanogap sites.

Considering that SERS is highly sensitive to the geometry of the plasmonic nanostructures, we extended the ligand-mediated interfacial control strategy to grow and characterize diverse Au nanostructures by using Au seeds with different sizes and shapes including Au nanotriangle and nanorods.

In Figure 2.9 a-f, visualizations of the 3D reconstruction of Au nanorods using

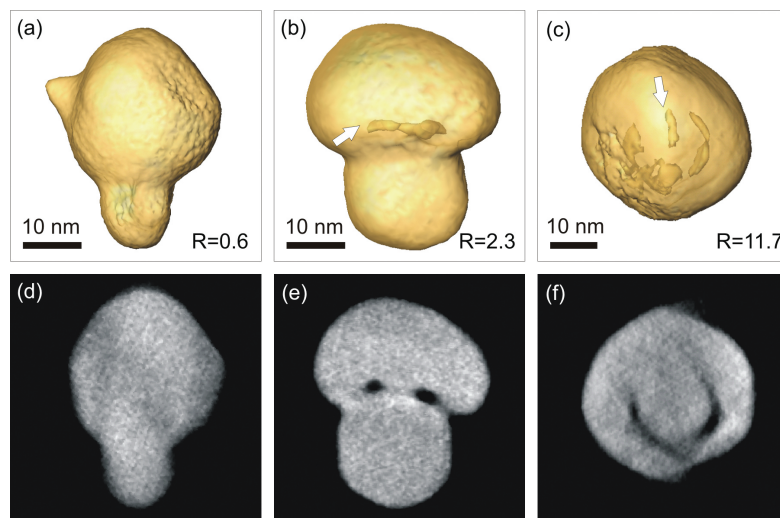


Figure 2.8: (a-c) The visualization of the 3D reconstruction of the Au nanospheres made with varying R values. (d-f) Orthoslices through the reconstructions shown in a-c, respectively.

different R values, are shown. When  $R = 1.4$ , the overgrowth of Au occurred only at the tip of the nanorod. Nanoparticles where Au growth started from both of the tips, were also observed. For higher concentration of Au ions ( $R = 28.7$ ), the tip growth continued asymmetrically. For larger R values ( $R = 115$ ), fully overgrown Au nanostructures are obtained. Similar to the nanostructures obtained from nanostar and nanosphere seeds, internal gaps are observed. These results indicate that the growth of Au follows a preferential direction, which may be due to two phenomena: (i) Using high resolution electron tomography study, Goris et al., have shown that the facets at the tips of a Au nanorod can be composed of high index  $\{520\}$  planes [36]. These planes are more reactive in comparison to  $\{110\}$  side facets, hence the overgrowth may initiate from the tips. (ii) It is reported that the mineralization mechanism involves a preferential interaction of surfactant molecules with the crystallographic facets along the rod site. Hence, providing the rod tips more access to the reaction medium to continue the growth [100].

A preferential growth direction can also be observed for the growth of Au using Au nanotriangles as seeds (Figure 2.10 a-f). Figure 2.10 a shows that most of the

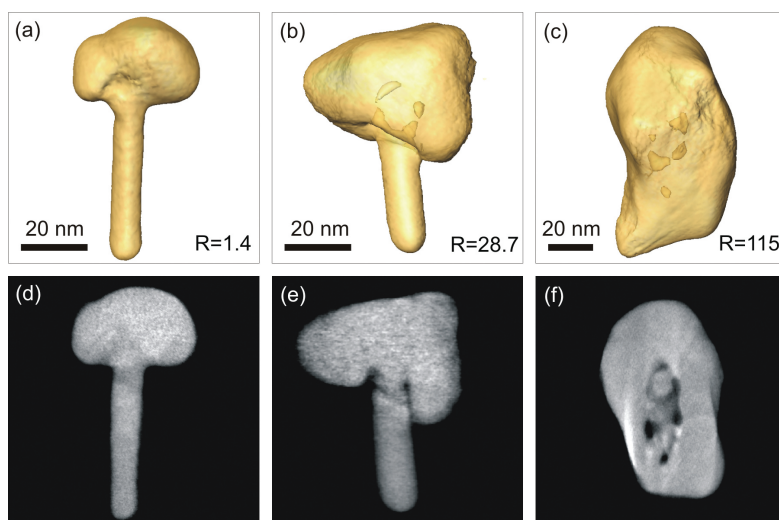


Figure 2.9: (a-c) Visualization of the 3D reconstruction of the Au nanorod for larger R values. (d-f) The orthoslices through the reconstructions shown in a-c, respectively.

islands grow at the side facets in comparison to the top and bottom surfaces of the Au nanoprism. This may be due to the faster decrease in the surface potential due to the surfactant at the side facets. As a result, the  $\text{Au}^{3+}$  flux becomes higher in these regions which facilitates the crystal growth rate in these regions [65].

Three principal growth models for the growth of a metal layer on a different metal (either as thin films or core-shell particles) have been reported, namely layered growth (Frank-van der Merwe mode), island growth (Volmer-Weber mode, VW), and an intermediate type (Stanski-Krastanow mode) involving an initial layer-by-layer growth followed by island growth mode [101, 102].

Based on 3D reconstructions, it is hypothesized that the Au shell growth starts from a few nucleation sites on the BDT-modified Au particle surface, then grows into a dimer-like nanostructure, and gradually encapsulates the rest of the BDT-modified seed. These results suggest that the VW island growth model appears to apply for each investigated nanostructure. Moreover, anisotropic Au nanoparticles show a preference towards growth on surfaces with high curvature, as exemplified by the semi-shell growth on one end of the nanorods and preferential growth along

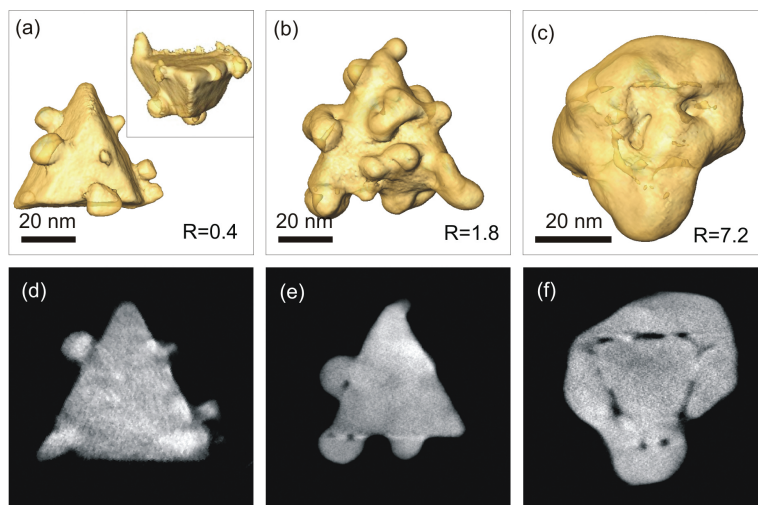


Figure 2.10: a) A visualization of 3D reconstruction is displayed from two different orientations. The image in inset displays the smaller amount of island growth on the surface of nanotriangle. (b-c) Visualization of the 3D reconstruction of the Au nanotriangles for larger R values. (d-f) Orthoslices through the reconstructions shown in a-c, respectively.

the edges of nanotriangles (Figure 2.9 and 2.10 a-f). This minimizes the contact area between core and shell and thus keeps the lowest interfacial energy during shell growth.

## 2.3 Conclusions

In summary, a systematic electron tomography study of the seeded growth of plasmonic Au nanocrystals containing internal nanogaps is presented. It is revealed that the seeded growth in the presence of BDT leads to a series of exotic nanostructures, in which internal gaps are consistently present. It is observed that these internal gaps with BDT leads to stronger SERS activity, especially for the semi-shell configuration. Additionally, based on 3D reconstructions, the VW type of growth mechanism is observed for each investigated morphology.

# Chapter 3

## Structure and Vacancy Distribution in Copper Telluride Nanoparticles Influence Plasmonic Activity

**This chapter is based on:**

T. Willhammar, K. Sentosun, S. Mourdikoudis, B. Goris, M. Kurttepli, M. Bercx, D. Lamoen, B. Partoens, I. Pastoriza-Santos, J. Perez-Juste, L.M. Liz-Marzan, S. Bals, G. Van Tendeloo, Structure and vacancy distribution in copper telluride nanoparticles influence plasmonic activity in the near-infrared, *Nature Communications*, 8, (2017)

In this chapter, structure-property relation of CuTe nanoparticles is investigated using TEM. The synthesis of the samples was carried out at the Bionanoplasmonics Laboratory, CIC biomaGUNE and Departamento de Quimica Fisica in Universidade de Vigo (Spain). TEM investigation and computational calculations are performed at EMAT, University of Antwerp. I was responsible for the high resolution electron tomography, EDX measurements and contributed to the diffraction tomography.

## 3.1 Introduction to Copper Telluride nanoparticles

To broaden the application field of plasmonic nanoparticles for SERS, other metals and various shapes and sizes of nanoparticles are also explored. To date, the application field of SERS is restricted to molecular families carrying functional groups such as  $-NH_2$  and  $-SH$  owing to their affinity for Au or Ag. In general, spherical Au and Ag nanoparticles present LSPR in the visible region. To detect biomolecules, the LSPR response needs to be shifted towards infrared wavelengths. Shifting the LSPR band from visible to infrared wavelengths is possible by optimizing the shape and the size of the nanoparticles towards the formation of nanostars. Unfortunately, this mostly results in an increased particle size, which limits the applicability of these particles in living organisms. Li et al. showed that copper based chalcogenides can be used as SERS probe due to their plasmonic properties [103]. Unlike Au and Ag nanoparticles for which the optical properties are mostly dependent on particle morphology, it is observed that the optical response of Cu chalcogenides consisting of Cu and Te can be tuned by optimizing Cu vacancies in the structure [103–106]. The vacancies in the structure not only regulate the charge transport properties, but also provide a composition-dependent LSPR in the near infrared [104–106]. Since these properties are not currently well understood, a compositional and structural analysis is required to relate the properties to the structure. In this chapter, the structure and vacancy distribution in CuTe nanoparticles is investigated. The outcome of these experiments is connected to the optical properties by DFT calculations.

## 3.2 Investigation of Structure and Vacancy distribution of CuTe nanoparticles

Although nanoplasmonics has been mostly restricted to the use of noble metal nanocrystals, several concerns regarding optical losses have promoted the study of

a variety of alternative plasmonic nanomaterials, including copper-deficient copper chalcogenides [58]. Most studies were carried out with copper sulfides and selenides, but plasmon tunability has also been demonstrated on CuTe nanocrystals, not only via carrier density but also via size and morphology control [107]. Interestingly, the Cu:Te ratio has been reported to affect the crystal structure. Indeed, the complex Cu-Te phase diagram reveals several phases such as orthorhombic CuTe, hexagonal Cu<sub>2</sub>Te and Cu<sub>3</sub>Te<sub>4</sub> phases as well as non-stoichiometric Cu<sub>2-x</sub>Te structures [108–110]. Recently, Li et al. [103] reported that CuTe nanocrystals, grown using a hot injection-like method, displayed a novel crystalline phase yielding interesting plasmonic properties towards sensing applications. Further progress in the optimization of the physical properties of the material requires an accurate determination of the local structure of the compound, which however has remained unknown so far because of its complexity.

Structure determination of complex nanomaterials is far from straightforward and is one of the main challenges in the field of crystallography. In addition, such studies become increasingly demanding for materials that lack perfect ordering or display disorder [111, 112]. For submicrometer-sized crystals, electron crystallography is often used and recent progress was initiated by the development of three-dimensional electron diffraction methods, such as rotation electron diffraction (RED) and automated diffraction tomography [113, 114]. These methods were successfully applied to unravel the structure of a broad variety of materials, including zeolites [115], MOF [116]. Although these techniques are at the forefront of structure characterization, major progress, especially for nanocrystals, is still required. Recently, the quality of the 3D reconstructions has been significantly improved through the use of advanced reconstruction algorithms and, as a result, 3D imaging with atomic resolution is now possible [36], thereby allowing monitoring and quantification of effects such as surface relaxation or strain in nanoparticles [117]. However, most of these atomic-scale 3D studies have so far been performed on noble metal nanoparticles, featuring a known and simple crystal structure.

We report here the solution of a much more challenging problem: the crystal structure of defective CuTe nanocrystals using a combination of electron diffrac-

tion tomography and high-resolution real-space tomography. This combination provides an exciting insight into the distribution of Cu vacancies within the framework of Te atoms. The characterization was complemented by EELS.

### 3.2.1 Structural Characterization

A HAADF-STEM overview of the resulting CuTe nanocrystals is shown in Figure 3.1 a . Using this technique, the image intensity scales with the atomic number  $Z$  of the elements present in the sample as well as with sample thickness. To investigate the morphology of the nanocrystals, a tilt series of HAADF-STEM images was acquired over a tilt range of  $\pm 72^\circ$  and used as an input for a SIRT 3D reconstruction algorithm. It is clear that the particles yield a cuboid morphology with two longer dimensions, referred to as  $a$  and  $b$ , and a third shorter dimension called  $c$ , see Figure 3.1 b. Interestingly, EELS measurements in the low-loss region demonstrate a plasmon resonance in the range of 1.1-1.7 eV (Figure 3.1 c).

A high-resolution HAADF-STEM image was acquired along one of the long directions,  $a$ , of the cuboid particle, see Figure 3.1 d. In this image, the brighter dots (indicated by red circles) correspond to Te ( $Z=52$ ) positions, whereas the less bright positions indicated by blue circles correspond to columns of Cu atoms ( $Z=29$ ). The pattern in the figure indicates a complex, modulated structure, suggesting the presence of vacancies at the Cu positions. An image acquired along the shorter direction,  $c$ , of the cuboid (Figure 3.1 d) does not show this modulation. To determine the structure of the nanocrystals, X-ray diffraction was applied. However, the pattern contains broad peaks, as can be seen in Figure 3.1 f, preventing direct structure determination from the data.

To investigate the atomic structure in more detail, a tilt series of SAED patterns are collected using the RED method in order to obtain a 3D data set with fine sampling of reciprocal space. The reciprocal space is sampled with a step of  $0.1^\circ$  over a tilt range of  $-62.9^\circ / 64.2^\circ$ . Next, this tilt series was combined into a 3D reconstruction of the reciprocal lattice, as shown in Figure 3.2 a. The pattern contains stronger reflections, which can be indexed in a primitive cubic unit cell with a cell parameter of 7.51 Å. These results are in good agreement with Figure 3.1

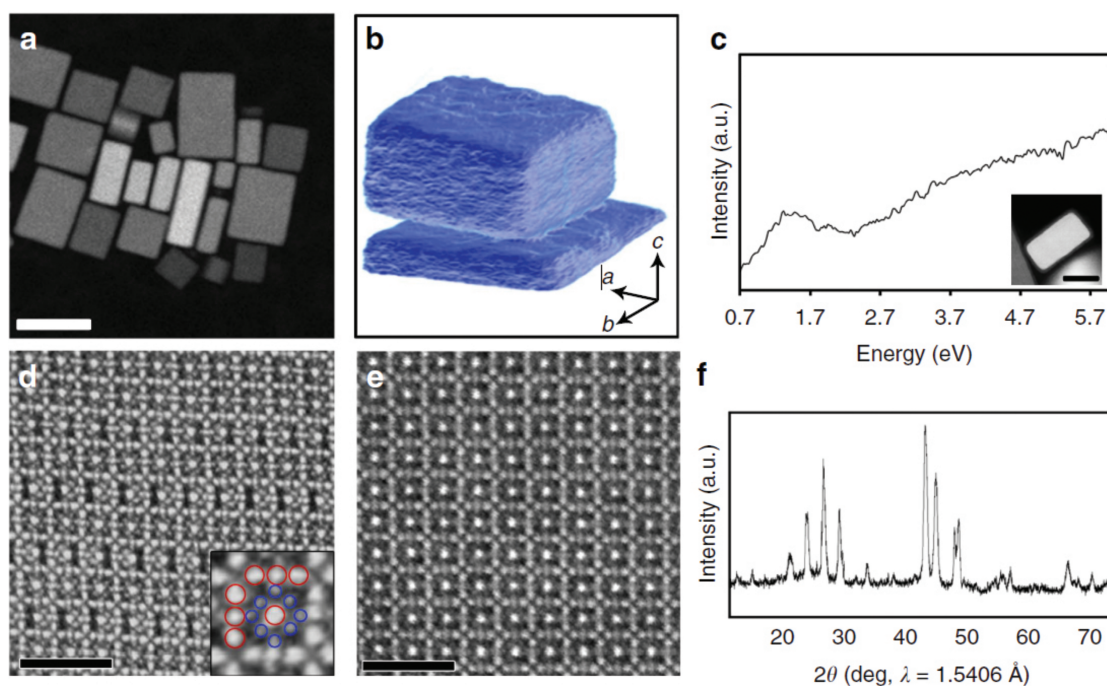


Figure 3.1: (a) HAADF-STEM overview showing the regular rectangular morphology of the particles. Scale bar, 50 nm. (b) Electron tomography reveals the cuboid morphology in three dimensions, with one dimension significantly shorter than the other two. The longer dimensions of the particles,  $a$  and  $b$ , are  $\sim 15$ – $40$  nm and the shorter,  $c$ , corresponds to  $\sim 15$ – $20$  nm. (c) EEL spectrum obtained from the low loss region after background subtraction showing a plasmon peak in the range of 1.1–1.7 eV. (d) High-resolution HAADF-STEM image acquired along the  $a$  direction. The projected distribution of heavier Te and lighter Cu atoms can be clearly observed. As an inset, the positions of Te (red) and Cu (blue) are marked. A modulation at the Cu sites can be clearly observed. The image was acquired with a long dwell time and hence sample drift gives rise to a slight geometric distortion. Scale bar, 2 nm. (e) High-resolution HAADF-STEM image acquired along the  $c$  direction does not show any obvious Cu-site ordering. (e) High-resolution HAADF-STEM image acquired along the  $c$  direction does not show any obvious Cu-site ordering. (f) X-ray diffraction pattern from the CuTe phase containing broad peaks.

c and d, where this unit cell can indeed be used to describe the contrast related to the Te lattice, observed along the [100] and [001] directions. An analysis of the reconstructed diffracted intensities suggests systematic absences for reflections within the (hhl) and (00l) groups with odd l indices. This leaves two possible space groups for the average structure: Pm-3n (No. 223) and P-43n (No. 218). Ab initio structure determination using direct methods in the space group Pm-3n resulted in a basic structure yielding eight Te atoms and 24 possible sites for Cu in one unit cell, which is illustrated in Figure 3.3 a. Both space groups Pm-3n and P-43n gave equivalent solutions; hence, the higher-symmetry space group Pm-3n was selected. To the best of our knowledge this structure is a novel phase within the Cu-Te system and it is not isostructural to any other crystalline phase with related composition. All Cu atoms are coordinated by four Te atoms with tetrahedral geometry. All Te atoms are coordinated by 12 Cu atoms, each of them with 0.5 occupancy, yielding an average coordination number of 6.

A high-resolution EDX map, see Figure 3.3 c, was acquired from the region indicated in Figure 3.3 b. It can be seen that the distribution of Te is in good agreement with the average structure model obtained by 3D electron diffraction. The distribution of Cu will be discussed in more detail below. In addition to the stronger reflections used for structure determination, weaker reflections can be observed. The reflections can be indexed using a superstructure with a four times larger unit cell along the c direction, the shorter direction of the particle, and three times longer along the a direction, see Figure 3.2 a. The modulation along the c axis often occurs as one reflection on each side of the stronger reflections of the substructure. In between the reflections, diffusely scattered intensities can be observed, indicating disorder along the c axis, see Figure 3.2 a, b. The three times modulation is significantly weaker compared to the modulation along the c direction and is consistent with observations by Tu et al. [118].

The results presented above demonstrate electron diffraction tomography yields some first insights in the average structure of the Cu-Te nanocrystals. However, more precise details on the complex distribution of the vacancies require the use of suitable imaging methods. In the HAADF-STEM images acquired along the

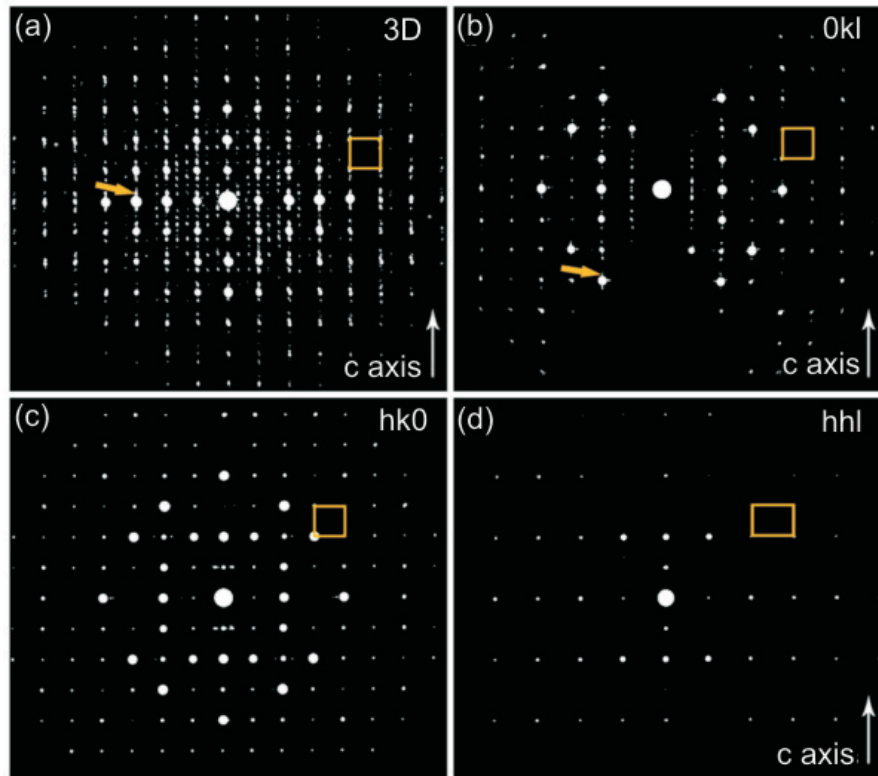


Figure 3.2: (a) Visualization of the reconstructed 3D reciprocal lattice obtained from a representative CuTe nanocrystal. The pattern contains stronger reflections, which can be indexed in a primitive cubic unit cell with a cell parameter of  $7.51 \text{ \AA}$ . In addition, weaker superstructure reflections can be observed with a periodicity of four times in the vertical direction and three times in the horizontal direction. In addition, diffusely scattered intensities are observed in between some reflections, marked by orange arrows in a,b. From the reconstructed 3D reciprocal lattice 2D sections can be visualized. (b) In the  $0kl$  section reflections from the four times superstructure can be observed. (c,d) The  $hk0$  and  $hhl$  sections reveal systematic extinctions for reflections with odd  $h$  within the  $0h0$  row and reflections with odd  $l$  indices within the  $hhl$  section. The projected unit cell is shown by an orange rectangle in each of the panels.

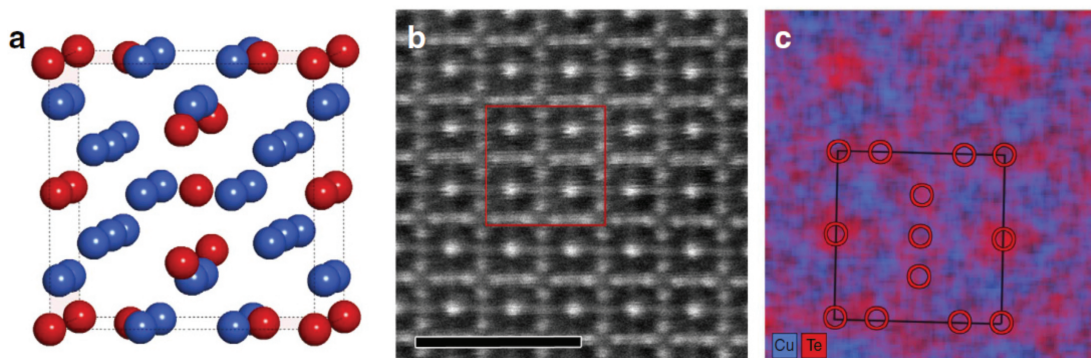


Figure 3.3: (a) Average cubic structure model obtained from the electron diffraction data (Te atoms in red, Cu atoms in blue). (b) HAADF-STEM image acquired along the  $[001]$  direction. The red square indicates the area for which an EDX map was collected. Scale bar, 2nm. (c) EDX map showing good agreement for the Te sublattice with the structure model obtained by electron diffraction.

$[100]$  direction the contrast distribution in between the Te atoms is clearly inhomogeneous (see Figure 3.4). An overlay with the average structure clearly shows fluctuations at the Cu positions. The image shows columns of the lighter Cu atoms, in accordance with the coordinates obtained from electron diffraction. However some of the Cu positions appear black; indicating vacant positions. The ordering of the Cu is clearly visible when the nanocrystals are imaged along either of the two longer dimensions, a or b. In order to determine the 3D distribution of the vacancies, high-resolution electron tomography is required.

A tomographic reconstruction is carried out based on five high-resolution HAADF-STEM images acquired with the rotation axis oriented along the short dimension of the cuboid nanocrystal, see the projection images (two representative projections are given in Figure 3.5). These five images were used as input for a tomographic reconstruction based on compressed sensing [44]. From the resulting tomographic reconstruction, the heavier Te atoms were found to be in good agreement with the atomic positions determined from 3D electron diffraction (Figure 3.6). However, the reconstruction does not yield any information concerning the presence of vacancies and is dominated by the intensities of the heavier Te atoms. In or-

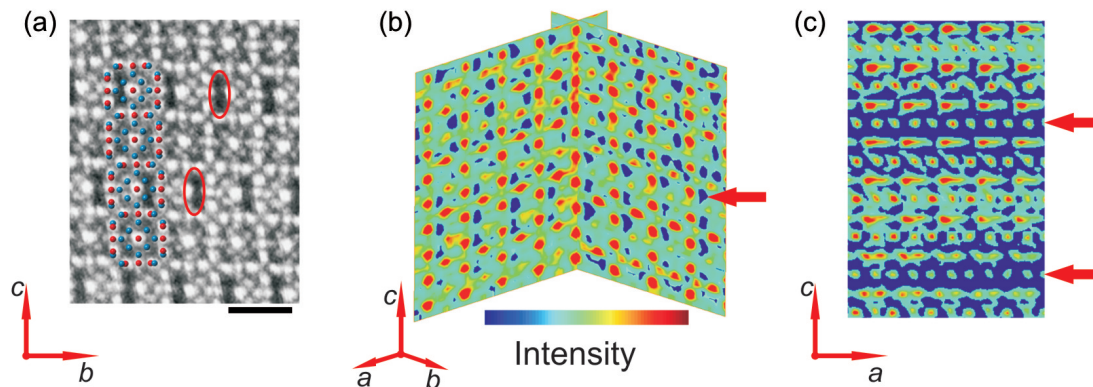


Figure 3.4: (a) HAADF-STEM image acquired along the  $[100]$  direction. The average structure model, including all possible Cu sites is superimposed with Te in red and Cu in blue. Some of the Cu-deficient domains are marked with red ellipses. Scale bar, 1 nm. (b) Perpendicular orthoslices through the electron tomography reconstruction perpendicular to the  $[100]$  and  $[010]$  directions reveal the inhomogeneous distribution of vacancies in 3D. The Te atoms are high-intensity (red) dots. In between the Te atoms, regions with a lower intensity (blue) show subvolumes inside the material with Cu deficiency (indicated by a red arrow). Long-range order of the Cu vacancies is present along the  $c$  axis. (c) An orthoslice sectioned perpendicular to the  $[010]$  direction reveals two channels of Cu deficiencies running along the  $a$  direction (marked by red arrows). In all panels the shorter dimension of the nanocrystal,  $c$ , is oriented along the vertical direction.

der to overcome this limitation, the positions of the Te atoms in one unit cell, as determined by 3D electron diffraction, were used as a template, which was fitted to the 3D reconstruction using the compressed sensing algorithm. Next, a continuous reconstruction algorithm was alternated with this template-matching method. Since the positions of the Te atoms can be refined using this procedure, the iterative coupling with the projection data leads to a gradually improving 3D reconstruction of the Cu distribution in between the Te atoms.

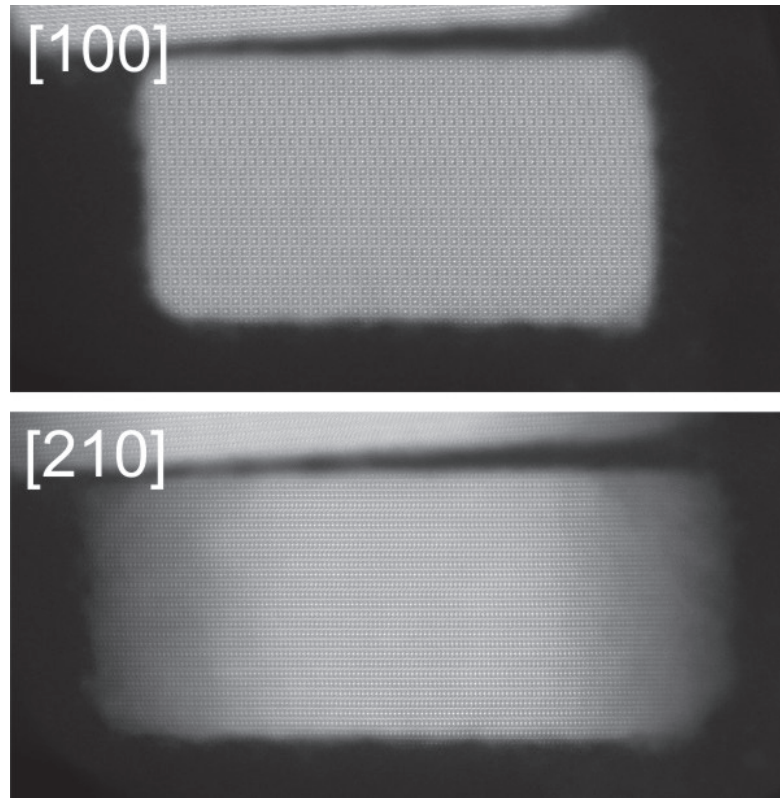


Figure 3.5: HAADF-STEM images, images were acquired along  $[100]$ ,  $[210]$  ( $26^\circ$ ) directions with tilt angles relative to the first zone axis in parentheses.

Orthoslices through the reconstruction, perpendicular to the  $[100]$  and  $[010]$  directions, are presented in Figure 3.4 b and enable a visualization of the distribution of vacancies in 3D. In this figure the low-intensity regions (blue) in between the Te atoms show the distribution of the Cu deficiencies. At this local scale, ordering along the shorter  $c$  dimension of the nanocrystal is clearly observed. The

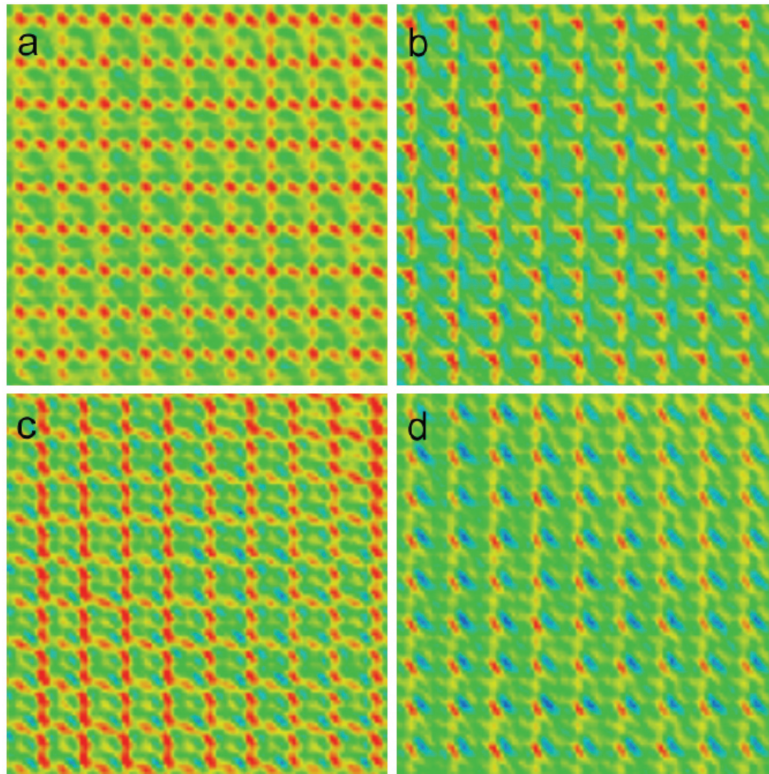


Figure 3.6: Orthoslices perpendicular to the  $[001]$  direction through the initial electron tomography reconstruction performed by compressed sensing. The orthoslices were obtained at an offset of (a) 0 (b) 0.25 (c) 0.5 and (d) 0.75 multiples of the unit cell ( $7.51 \text{ \AA}$ ). Red contrast is the highest intensity and resembles the positions of the heavier Te atoms as they were determined from electron diffraction.

order of the vacancies has a preference for a modulation of four average unit cells along the  $c$  axis. This behavior is further confirmed by a FT calculated from images acquired along the  $[100]$  direction (see Figure 3.7). This suggests that the superstructure can be described using a unit cell of  $7.51\text{\AA} \times 7.51\text{\AA} \times 30.04\text{\AA}$ . The ordering along one of the main crystallographic directions further explains the fact that the nanocrystals exhibit a non-isotropic cuboid morphology with one dimension different from the other two. As indicated in Figure 3.4 c, our results show that in local parts of the nanocrystal neighboring Cu sites are absent. This behavior creates “channels” of vacancies running through the nanocrystals along two crystallographic directions:  $[100]$  and  $[010]$ .

### 3.2.2 Structure property correlation

It is important to understand the correlation between structure and optical properties, including the effect of vacancies. The structural findings using electron diffraction tomography and high resolution electron tomography are used as an input for first-principal calculation and dielectric functions are calculated. Therefore, calculations of the dielectric properties were performed. The dielectric properties of the Pm-3n structure with all 24 Cu sites occupied were compared to the properties of the  $7.51\text{\AA} \times 7.51\text{\AA} \times 30.04\text{\AA}$  superstructure created by the presence of Cu vacancies. The distribution of the Cu vacancies is based on the findings from the electron tomography reconstruction, where vacant Cu sites form “channels” running through the nanocrystals.

In order to evaluate the importance of the vacancies, simulations of electron energy loss spectra based on the calculated dielectric properties were performed for cuboid-shaped particles with a size of  $25 \times 25 \times 15 \text{ nm}^3$  for both the structure with all Cu sites occupied and for a structure with half of the sites vacant. Whereas the energy loss spectrum from the structure without vacancies does not show any distinct maximum in the region between 0 and 2 eV, the model including vacancies predicts a distinct maximum in the low-loss function with a maximum around 1.35 eV (see Figure 3.8 a). This activity is consistent with the experimental EEL spectrum ( Figure 3.8 a) that shows a band in the range between 1.1 and 1.7 eV.

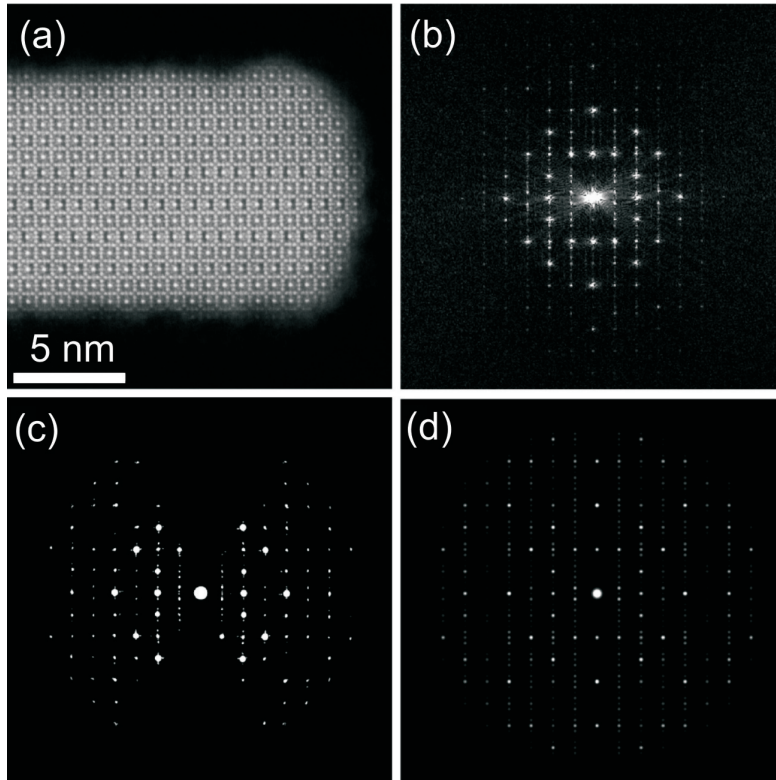


Figure 3.7: (a) HAADF-STEM image from a CuTe particle aligned along the  $[100]$  direction. (b) The corresponding FT calculated from (a). (c) Section from the reconstructed 3D reciprocal lattice perpendicular to the  $[001]$  direction and (d) simulated kinematical electron diffraction pattern along the same direction based on the structure including vacancies. In the FT a modulation can be observed running along the vertical  $c$  direction. In (a) the corresponding modulation of four times of the average unit cell along the  $c$  direction can be observed in some parts of the particle. The electron diffraction data as well as the simulated diffraction pattern exhibits the same modulation.

We additionally simulated the optical absorbance spectrum using the calculated dielectric properties, for cuboid-shaped particles with a size of  $25 \times 25 \times 15$  nm<sup>3</sup> dispersed in toluene. The calculated spectrum, with a maximum  $\sim 1,005$  nm, is in good agreement with the experimental one (maximum around 1,025 nm; Figure 3.8 b). The agreement between the dielectric function calculations and the experiments clearly demonstrates that the presence of the vacancies determines the optical properties of the nanomaterial.

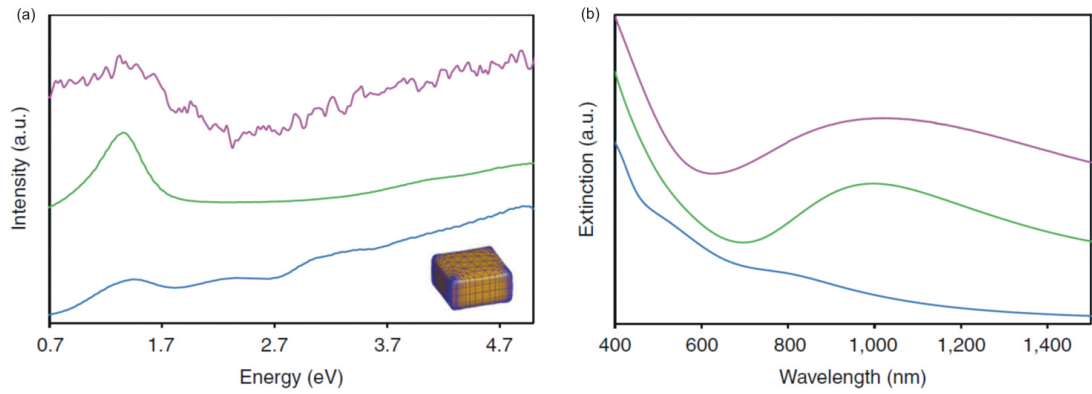


Figure 3.8: (a) Simulated electron energy loss spectrum calculated from the structure model with half of the Cu sites vacant (green) shows a distinct maximum, as compared to the calculated activity based on the structure with all Cu positions occupied (blue). The experimental EEL spectrum after subtraction of the carbon background is shown for comparison in red. As an inset, a visualization of the morphology of the particle used for the simulation is shown. (b) Corresponding calculation of the optical extinction spectra in the visible near infrared region shows that the structure with vacancies (green) has a significantly improved optical response compared to the model without vacancies (blue). The experimental spectrum is shown in red.

### 3.3 Conclusions

In summary, this work presents an accurate determination of the average structure of a previously unknown CuTe phase in a nanocrystalline form based on 3D electron diffraction data. A detailed study of the atomic structure using HAADF-STEM tomography revealed the presence of “channels” of vacancies running through the nanocrystals. The obtained structure was used to calculate the corresponding optical properties, which were found to be in good agreement with experimental data obtained from real nanocrystals. These results not only explain the plasmonic properties of copper-deficient copper chalcogenides, but also demonstrate the application of atomic resolution tomography to reveal an unknown crystallographic structure of complex nanocrystals containing defects.



## Chapter 4

# Characterization of Porous Pt Nanoparticles using Electron Tomography

**This chapter is based on:**

B. Geboes, J. Ustarroz, K. Sentosun, H. Vanrompay, A. Hubin, S. Bals, T. Breugelmans, Electrochemical Behavior of Electrodeposited Nanoporous Pt Catalysts for the Oxygen Reduction Reaction, *ACS Catalysis*, 6(9), (2016), 5856-5864

In this chapter, the structural characterization of porous Pt nanoparticles is presented. The synthesis of the samples is carried out by the Electrochemical and Surface Engineering Laboratory at the University of Brussels. I was responsible for all 2D and 3D TEM investigations.

## 4.1 Introduction to Porous nanomaterials

Porous nanomaterials have attracted much attention due to their interesting physical properties, such as a high surface-to-volume ratio, which is interesting for applications such as catalysis and drug delivery. According to the International Union of Pure and Applied Chemistry classification, porous nanomaterials can be divided into three classes depending on their pore sizes. Materials with a pore size of 50 to 1000 nm are referred as macroporous materials. Smaller pores with a diameter between 50 to 2 nm are called mesopores, whereas pores with a diameter between 2 to 0.2 nm are denoted as micropores. Depending on the size of the pores, the material is used for different application. In this thesis, both mesoporous (Pt nanoparticles) and microporous nanomaterials (metal-organic frameworks) are investigated. A brief explanation about Pt nanoparticles is given in this chapter whereas the introduction for metal organic frameworks is presented in chapter 6.

### Pt nanoparticles

Platinum nanoparticles are one of the most promising catalysts for hydrogen oxidation and oxygen reduction in polymer electrolyte membrane fuel cells (PEMFC) [119, 120]. The nanoparticles propel cathodic oxygen reduction reactions (ORR) in fuel cells where oxygen is reduced to water by the transfer of four electrons and four protons. However, the high cost of Pt constrains a broad deployment of Pt nanoparticles in fuel cells. Several approaches have been studied to develop high performance electro-catalysts, of which increasing the ratio of Pt surface atoms is a possible route [121]. By increasing the surface to volume ratio, the surface area increases and as a consequence the catalytic activity also increases. Another approach is increasing the number of dangling bonds by avoiding the formation of close packed, low index crystallographic facets at the surface. This yields an enhanced electro-chemical activity [122, 123]. The improved activity is mediated by alteration of the electronic structure of the surface atoms [124]. Moreover, due to the biocompatibility of Pt nanoparticles, they can be useful for biomedical applications, such as cancer therapy through photothermal treatment [125]. In

general, colloidal chemistry [126–129] and electrodeposition [130, 131] techniques are used for the synthesis of Pt nanoparticles. In this chapter, the porous structure of Pt nanoparticles which are electrodeposited on a C support is investigated. By using TEM and electron tomography, the surface area of single nanoparticles can be directly evaluated. These microscopically obtained values can be correlated to macroscopic properties. Hence, quantitative porosity estimation and pore size determination in 3D needs to be performed.

## 4.2 3D Porosity investigation of Pt nanoparticles

PEMFCs are promising for sustainable energy cycle application [132] where Pt nanoparticles are used both in the anode and cathode to split  $H_2$  and  $O_2$  molecules, respectively. However, the high capital cost of PEMFCs compared to conventional electricity production impedes their wide-spread implementation [133]. The high Pt loading required to achieve sufficient reaction rates at the cathode side in PEMFCs, is a result of the slow ORR kinetics. As mentioned previously, the majority of the investigated strategies are invested in improving the Pt efficiency. To increase the ORR activity, different strategies are proposed by increasing Pt efficiency: (i) generating small domains (nanopores), such that the reaction rate can be increased since these confined reaction surroundings lead to higher frequency attempts, (ii) increasing the surface to volume ratio, (iii) avoiding low-coordinate close packed facets and planes and obtain high-coordinate facets at the surface to increase the number of atoms and dangling bonds. In order to achieve these prerequisites, a profound understanding of the 3D morphology of Pt nanoparticles is crucial. Therefore, 3D characterization techniques should be applied.

Conventionally, porosity measurements are performed using a gas adsorption method which follows the BET theory. These methods aim to quantify the physical adsorption of gas molecules, such as N, O or H on a solid surface. When the pressure of the the gas molecules is increased in the chamber containing the solid which is originally kept at cryogenic temperature, the molecules start to condense on the solid surface. First, the small pores are filled, then by increasing the

gas pressure, all the accessible pores are filled up. By monitoring the change in gas pressure, the amount of absorbed molecules can be measured. This method provides information regarding the available pores and pore diameter of the solid [134]. On the other hand, the development of electron tomography also allows one to obtain information regarding the presence of pores and the surface area of a specimen. Using electron tomography, porosity and surface area measurements can be performed at the single nanoparticle level. An additional advantage of electron tomography is that by visualizing the pore network, one can also study the connectivity of pores.

In order to obtain highly porous Pt nanoparticles, two different routes are generally used: (i) synthesizing the particles with colloidal chemistry and (ii) electrodeposition of nanoparticles. Electrodeposition of Pt nanoparticles has numerous advantages over colloidal chemistry methods. For instance, for PEMFC applications, the Pt nanoparticles need to be grown on a C substrate [135]. Hence, after the synthesis, the Pt nanoparticles should be sputtered or sprayed on a C substrate. However, electrodeposition of Pt can be performed directly on the C substrate which decreases the processing time and thus the cost. More importantly, electrodeposited Pt is located in the regions where ionic and electronic conductivity is high. This results in the deposition of Pt nanoparticles located at electronically active regions, which increases the efficiency in comparison to sputtering and spraying where Pt nanoparticles are randomly dispersed on the C substrate.

In this study, the samples are prepared using a direct double-pulse electrodeposition procedure at room temperature. Using this method, nuclei formation and growth are separated in time, by first applying a short nucleation pulse of high over-potential, followed by a longer growth pulse of lower overpotential, in respect to the first pulse. Relatively mono-disperse metal nanoparticles have since been synthesized on several occasions [136, 137]. In this manner, two samples are prepared using different parameters. For the first sample, a double pulse deposition of Pt is performed with a nucleation pulse of -0.4 V for 50 seconds and a growth pulse of -0.1 V for 50 seconds. For the second sample, the deposition procedure

comprises a nucleation pulse of -0.6 V for 50 s and a growth pulse of -0.2 V for 100 s. These samples are referred to in the text as low and high over-potential deposits, respectively. The discussed deposition procedures are selected on the basis of nanoporosity from a prior parameter study. The results can be separated in two parts. In the first part, a morphological characterization of the Pt nanoparticles, which are electrodeposited at different conditions, is performed. In the second part, the stability of Pt nanoparticles morphology towards the ORR is investigated by electron tomography.

### **4.2.1 2D Characterization**

Field emission scanning electron microscopy (SEM) images were used to elaborate statistics of the particle distributions [131]. The average particle size of the low over-potential deposition is 89 nm compared to 116 nm for the high over-potential procedure. The difference in average particle size is a result of longer growth time (100 seconds) using the latter procedure. The histograms obtained from the SEM images for the low and high over-potential deposits are shown in Figure 4.1 a and b, respectively. In both a bimodal size distribution can be observed with a limited amount of smaller nanoparticles around 10 nm in diameter in addition to larger deposits. Such a bimodal size distribution is common in electrodeposition even when a double pulse procedure is used [138]. The fraction of small nanoparticles is limited to 3% and 8% in the low and high over-potential samples, respectively.

HAADF-STEM images of Pt nanoparticles from the high and low over-potential deposition are shown in Figure 4.2 a and b, respectively. The HAADF-STEM image indicates that the nanoparticles are formed by agglomeration of small (3-4 nm) Pt particles (highlighted by a red circle) in Figure 4.2 a. Spike formation at the edges is observed as illustrated in Figure 4.2 a. Moreover, low intensity regions are observed and indicated with a green arrow. Since the intensity of a HAADF-STEM image scales with the thickness, these areas correspond to a pore in the structure.

In Figure 4.2 b and c, representative HAADF-STEM images from the sample with low over-potential are presented. For this sample, the morphology is slightly

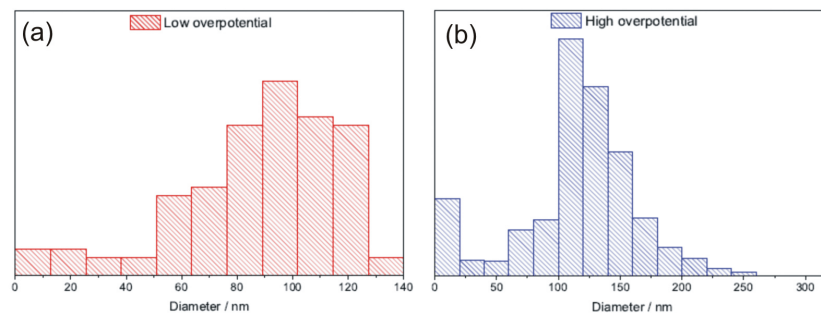


Figure 4.1: Histograms showing the particle size distribution calculated from SEM data of the low over-potential (a) and high over-potential (b) sample.

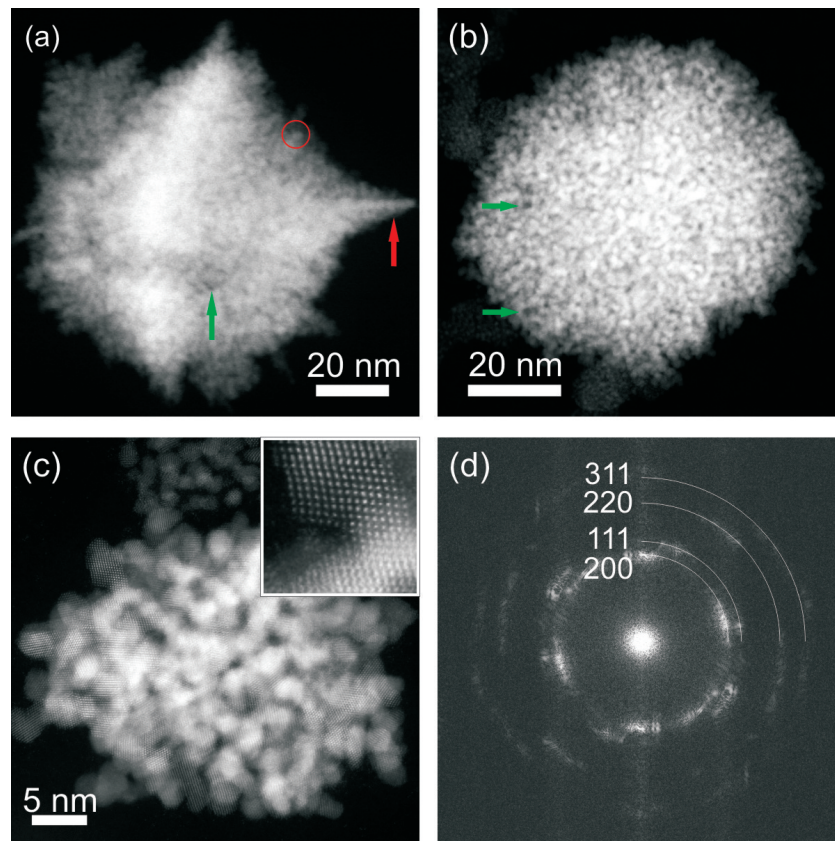


Figure 4.2: (a) HAADF-STEM image from a high over-potential nanoparticle, (b,c) a low over-potential nanoparticle in different particle sizes, (d) the FT of the image displayed in c.

different in comparison to high over-potential sample. Spike formation is not observed and a more spherical shape of the particles is found. Moreover, the number of low intensity regions, which are highlighted by green arrows, is increased. Therefore, the sample porosity is expected to be higher in comparison to the previous sample. Figure 4.2 c shows a smaller nanoparticle and the crystal structure of the agglomerate is revealed by high resolution HAADF-STEM imaging. These high resolution HAADF-STEM images are obtained using a cubed FEI Titan 60-300 microscope operated at 300 kV. A high resolution image from an agglomerate is shown in the inset of Figure 4.2 c and the FT is presented in Figure 4.2 d. The indexed planes clearly proves the poly-crystallinity of the sample and the presence of both low (200) and (111) and higher index (220) and (331) lattice planes. The presence of high index lattice planes are favorable for better catalytic activity since they yield a higher amount of dangling bonds and bonding energy is available if they are located in the surface [122, 123].

### **4.2.2 3D Characterization**

In order to gain better insight into the 3D morphology and thereby the porosity of the electrodeposited nanostructures, HAADF-STEM tomography experiments were performed for both high and low over-potential deposits. To obtain unbiased information, nanoparticles of different sizes were investigated. For each selected particle size, electron tomography is performed for two different nanoparticles. The electron tomography experiments were performed using a FEI Tecnai G2 microscope operated at 200 kV. A Fischione tomography holder (model 2020) is used and the tilt series were acquired over a tilt range of  $\pm 74^\circ$  with a  $3^\circ$  increment. The tilt series was aligned using FEI Inspec3D [21] and reconstructed using the SIRT implementation of the ASTRA-Toolbox [92]. The outcome of the electron tomography experiment for both high and low over-potential nanoparticles is presented in Figure 4.3.

A 3D visualization of the reconstruction and an orthoslice through the 3D reconstruction obtained from a 115 nm high over-potential particle (corresponding to the average particle size that was determined by SEM analysis) is presented in

Figure 4.3 a and b, respectively. It is clear that the surface area of the nanoparticles exhibits a dendritic morphology, which leads to an increased surface/volume ratio of the nanoparticle. However, a slice through the reconstruction, presented in Figure 4.3 b, clearly reveals that the small channels inside the nanoparticle are present.

The diameter of these pores are estimated from the 3D reconstruction and were found to be approximately equal to 3-4 nm. In previous work [34], it was shown that the missing wedge influences quantitative measurements from a 3D reconstruction. In case a missing wedge of  $\sim 40^\circ$  is present in a SIRT reconstruction (which corresponds to the missing wedge here), it is shown that elongated structures are obtained and the error bar for quantitative measurement is  $\pm 15\%$ .

These internal pores are of significant importance for catalytic activity since they yield increased surface area if they are connected to the outer surface. In order to understand whether these pores have a connection to the surface, an analysis of the 3D reconstructions is required. To perform this analysis, each slice of the 3D reconstruction is analyzed using a dedicated algorithm developed by Vanrompay et al. [139]. The algorithm requires a segmentation of the 3D reconstruction, where voxels are classified as Pt ( $V_{Pt}$ ) or pores in the Pt particle. Next, the voxels corresponding to empty space (pores) are analyzed and divided into two classes. The voxels that have a connection with the exterior ( $V_e$ ) are distinguished from the voxels that have no connection with the exterior ( $V_i$ ) and which therefore correspond to internal voids inside the Pt nanoparticle. Finally, the porosity  $P$  is defined using equation 4.1 as the volume ratio between the pores that have a connection with the exterior  $V_e$  and the entire volume of the Pt nanoparticle.

$$P = \frac{V_e}{V_{Pt} + V_e + V_i} \quad (4.1)$$

The analysis of the 2D orthoslices from the 3D reconstructions of high overpotential nanoparticles revealed that limited number of the internal pores have a connection to the outer surface of the nanoparticle which classifies them as a void or cavity within the structure. Such types of cavities are chemically inactive since they have no connection to the outer surface of the nanoparticle. An internal cavity is highlighted with a green arrow in Figure 4.3 b. However, we have to emphasize

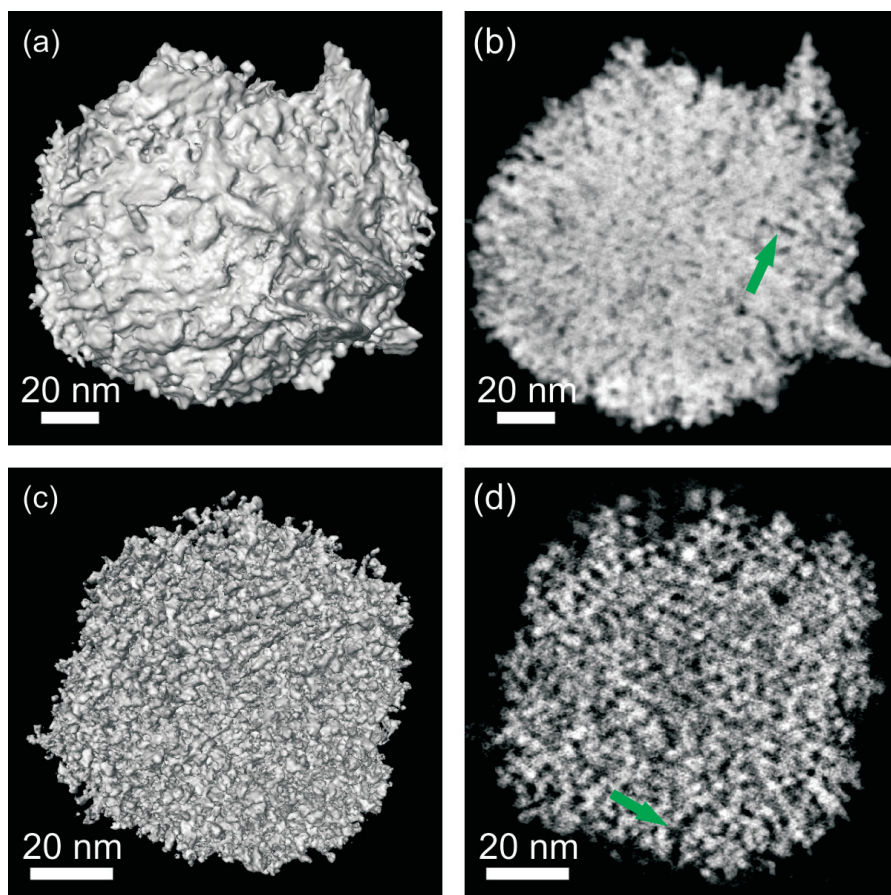


Figure 4.3: 3D visualization of the electron tomography reconstruction and a slice through the 3D data set are depicted for high over-potential (a,b) and low over-potential particles (c,d), respectively. The dendritic morphology of the low over-potential particle can be clearly observed from the 3D visualization. The red arrow indicates a dendrite on the surface while the green arrows indicate pores.

that we can only conclude that this pore is a cavity based on the 3D analysis of the all the orthoslices. The porosity extracted from the 3D reconstruction of several nanoparticles is plotted in function of particle size in Figure 4.4.

Based on this analysis, the high over-potential catalyst has a porosity of ca. 5% in the entire measurement range of particle size (black circles). The porosity in these particles is mainly formed through surface roughness, while almost no internal pores are accessible. A similar investigation is also performed on the low over-potential sample. A 3D visualization of the reconstruction and a slice through the 3D reconstruction of a low over-potential particle is presented in Figure 4.3 c and d, respectively. The particle has a diameter of ca. 88 nm which corresponds to the average particle size calculated from SEM images. Figure 4.3 c confirms the highly dendritic morphology which is present in the nanoparticle (c.f. Figure 4.3 c and a). Compared to the first sample, the highly dendritic morphology of the sample drastically increases the surface area which should improve the catalytic efficiency of these nanostructures for catalytic activity. The analysis of the 2D slices through the 3D reconstruction revealed the quasi-spherical protuberance of ca.  $2.5 \pm 0.4$  nm at the outer edges of the nanostructure which are highlighted with a circle in Figure 4.3 d. These spherical structures are linked to the rest of the nanoparticle by narrower necks which are depicted with an arrow. For each selected nanoparticle, the porosity is calculated as explained by Equation 4.1 and plotted in function of particle size (red circles in Figure 4.4). In the low over-potential particles a clear size dependency of porosity is visible. Although with porosities between 17 and 28 % for all measured low over-potential particles, there is a significant difference compared to the values of the high over-potential catalyst particles.

### 4.2.3 Growth mechanism of electrodeposited Pt nanoparticles

The growth of nanoparticle or thin films on a substrate consists of 6 main steps. *(i)* Adsorption of atoms or molecules on substrate, *(ii)* surface diffusion, *(iii)* formation of molecule-molecule and substrate-molecule bondings, *(iv)* nucleation by

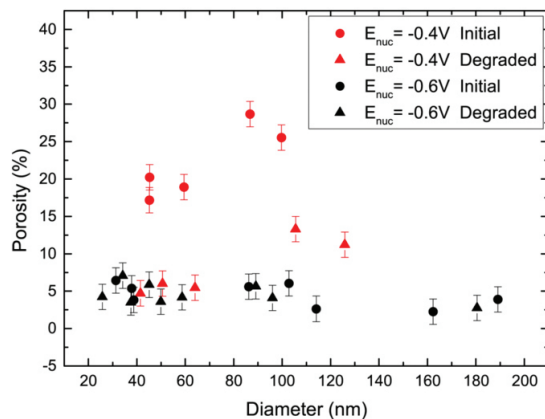


Figure 4.4: Porosity values calculated from the 3D tomography reconstruction for the as-deposited low (red circles) and high over-potential catalysts (black circles). Porosity values after catalyst degradation using 600 potential cycles between 0.1 and 1.5 V are shown for the low (red triangles) and high over-potential catalysts (black triangles).

means of aggregation of single atoms or molecules, (*v*) structure and crystal structure formation, (*vi*) further particle growth by means of diffusion or grain growth [140]. The growth mechanism in electrodeposition of Pt nanoparticles is explained in Ustarroz et al. [141]. In very early stages, by the application of a negative potential, small clusters of 2-4 nm are formed and randomly distributed on a C substrate. A representative high resolution HAADF-STEM image of such a small cluster is shown as an inset in Figure 4.2 c. These clusters are bonded to the substrate with weak Van der Waals bonds. By applying a negative potential (-0.4 V), the weak Van der Waals bonds break and surface diffusion of these clusters over the C substrate takes place. When the particles connect due to the particle-particle attractive Van der Waals forces, nanoclusters tend to coalesce. This results in aggregative nucleation events. Hence, particles form by aggregation of small clusters with high porosity as shown in Figure 4.3 c (low over-potential nanoparticles). After the nucleation pulse, the over-potential is changed to -0.1 V and growth of the nanoparticle continues with direct attachment of reduced Pt ions.

As shown in Figure 4.2 a and 4.3 a, when a higher over-potential is applied,

smoother and less porous nanostructures are obtained. This may be due to a second recrystallization because of the higher over-potential. As a consequence of the recrystallization the nanoparticle, the porous structure degrades and less porous particles are obtained.

#### 4.2.4 Investigation of Electrocatalytic Stability of Pt nanostructures using Electron Tomography

Although porous Pt nanoparticles may increase the ORR efficiency in the early life stages of the PEMFC's, their application is only possible if they can maintain their activity under the operative conditions of fuel cells. To investigate the stability of Pt nanoparticles towards the ORR efficiency under harsh fuel cell start-up conditions, electron tomography is carried out on the same sample batch before and after 600 oxidation/reduction cycles. The top row in Figure 4.5 shows the 3D morphology and a slice through the 3D reconstruction of the nanoparticles before electrochemical cycling. Figures on the bottom row show the 3D morphology of the nanoparticles after 600 potential cycles of oxidation/reduction. The first prominent result is that, for both electrodeposited samples, the morphology of the Pt nanostructures drastically changes after 600 cycles. A substantial collapse of the nanopores is clearly visible in the 3D particle reconstruction. The porosity of both as-prepared and degraded nanoparticle' as a function of particle diameter is shown in Figure 4.4. Porosity of the as-prepared low over-potential catalyst (red circles) around 100 nm is in the range of  $25\% \pm 3\%$ . After degradation through potential cycling (red triangles) the porosity is diminished to ca.  $10\% \pm 3\%$ . The high over-potential catalyst only has a porosity of ca.  $5\% \pm 3\%$  before and after degradation (black circles and black triangles in Figure 4.4, respectively) over the entire range of measured diameters. It appears that a semistable morphology is obtained. This is an indication that the collapse of nanopores is not a part of the degradation mechanism for the high over-potential catalyst.

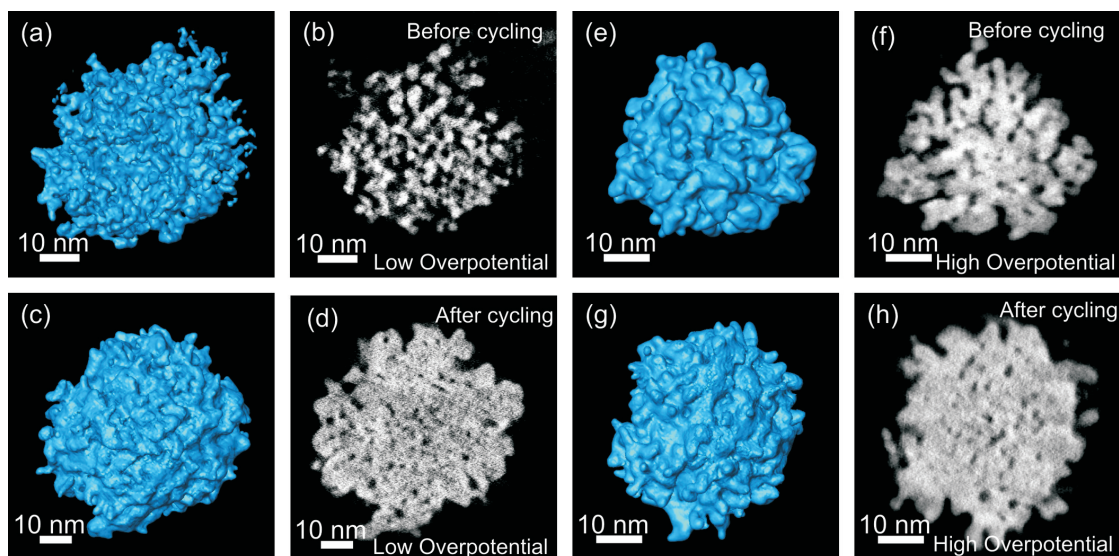


Figure 4.5: Representative visualization of a 3D reconstruction of a Pt nanoparticle electrodeposited with low over-potential (a) before and (c) after electrochemical cycling. Representative orthoslice of a Pt nanoparticle electrodeposited with low over-potential (b) before and (d) after electrochemical cycling. Representative visualization of a 3D reconstruction of a Pt nanoparticle electrodeposited with high over-potential (e) before and (g) after electrochemical cycling. Representative orthoslice of a Pt nanoparticle electrodeposited with high over-potential (f) before and (h) after electrochemical cycling.

## 4.3 Conclusions

The influence of high and low over-potential is investigated using 2D and 3D TEM methods. It is clearly observed that, in each case, the growth of polycrystalline Pt nanoparticles is obtained. Moreover, in the case of low over-potential, electron tomography showed that the Pt catalysts samples have a highly dendritic morphology with large surface to volume ratio and that the pores were accessible to oxygen species. As a result of the accessibility of the active sites inside the nanopores, an enhancement of the electrochemical surface area corrected ORR activity was observed at the highly porous structures. This is of great importance for the production of highly efficient Pt catalyst which may reduce the cost of PEMFC. Successive potential cycling of Pt nanoparticles in oxidation/reduction region leads to a significant reduction of the active surface area due to a partial collapse of the open nanopores. This results in more compact and smooth nanostructures.

## Chapter 5

# Combination of HAADF-STEM and ADF-STEM Tomography for Core-Shell Hybrid Materials.

**This chapter is based on:**

K. Sentosun, M.N. Sanz Ortiz, K.J. Batenburg, L.M. Liz-Marzan, S. Bals, Combination of HAADF-STEM and ADF-STEM Tomography for Core-Shell Hybrid Materials, *Particle & Particle Systems Characterization*, 32(12), (2015), 1063-1067

## 5.1 Introduction to Multi-functional nanoparticles

In chapter 2, 3D characterization of Au nanoparticles for SERS applications was presented. To increase their applicability and broaden the application field, such particles are combined with different functional nanomaterials [142]. This resulted in multi-functional nanoparticles. The plasmonic properties of Au nanorods make them a great candidate for light based imaging and therapeutic techniques. For instance, using the photothermal effect they can be used as a local heat source which can be applied in hyperthermal cancer therapy or they may trigger drug release for chemotherapeutics [143]. However, using these nanoparticles in such applications is not straightforward, since the surface area of such nanoparticles is low and the loading of the drug amount is limited. Another problem is the colloidal stability of these nanoparticles which needs to be increased since they tend to form clusters and aggregates. To overcome these problems, mesoporous silica can be used. The discovery and development of mesoporous silica attracted great interest in material science [144]. These nanomaterials possess narrow pore size which leads to large internal surface area. For instance, the high surface area of mesoporous silica grants high amount of drug load. Moreover, the silica coating prevents the aggregation of the Au nanoparticles. An efficient route to combine these nanostructures is encapsulating plasmonic nanoparticles such as Au with mesoporous silica which leads to core-shell type multi-functional nanostructures. As the nanostructure becomes more complex, 3D characterization also becomes more difficult. To perform an unambiguous characterization of such multi-functional nanoparticles, the development of novel techniques is necessary. A methodology to characterize core-shell nanostructures comprising both heavy and light elements in the same confined region is presented in this chapter. Here, a novel material targeted 3D characterization method was developed to characterize functional nanoparticles which have components made of heavy and light atoms in the same confined region is presented.

Over the last decades, electron tomography has evolved into a standard tech-

nique to investigate the 3D structure of a broad range of (nano)materials [20, 64, 145–148]. To reconstruct the 3D structure of an object from its 2D projections, a monotonic relationship between image intensity and mass-thickness is required [20]. When applying electron tomography to crystalline solids, diffraction contrast must therefore be avoided [149]. Indeed, diffraction contrast depends on the orientation of the object with respect to the electron beam and therefore the projection requirement for electron tomography is not fulfilled [20]. As a consequence, artefacts will occur in the final 3D reconstruction [150, 151]. This is one of the main reasons why electron tomography in materials science is mostly based on HAADF-STEM [20, 152]. For each composition, the intensity of the HAADF-STEM images changes monotonically with specimen thickness thus fulfilling the projection requirement. To obtain 3D reconstructions from HAADF-STEM tilt series, reconstruction algorithms such as the SIRT [42], TVM [34, 44] and the discrete algebraic reconstruction technique [153] are currently used. Also for samples that consist of more than one type of element, HAADF-STEM tomography is very valuable since not only morphological, but also chemical information can be extracted [152]. However, for samples in which elements with a high and low atomic number ( $Z$ ) are simultaneously present, data acquisition becomes even more challenging. Since the intensity is strongly dependent on the atomic number [152], a high difference in  $Z$  in the material leads to a large difference in the collected signal that is not always possible to cover with the detector's dynamic range. Therefore, some areas of the image can be either over - or under saturated. This situation is often encountered when investigating core-shell hybrid materials such as nanoparticles encapsulated by a lighter matrix. In this chapter, we propose an improved approach to obtain reliable 3D reconstructions for these systems, which requires optimization of both the acquisition technique and the reconstruction algorithm. During the acquisition, HAADF-STEM images are acquired using different collection angles through the simultaneous use of different (HA)ADF detectors. Prior to the reconstruction, advanced masking and interpolation will be applied. As an example, we focus here on the reconstruction of a pentatwinned Au nanorod coated with a mesoporous silica shell. These types of materials are of great interest due to

applications in catalysis, bio-sensing and non-linear optics [154–157]. Our results are equally applicable to other hybrid nanosystems such as coated bio-templates, porous materials loaded with nanoparticles or carbon nanotubes that are covered with an inorganic layer.

### 5.1.1 Experimental Details

The synthesis of penta-twinned Au nanorods was carried out following a previously reported protocol [7]. Coating with mesoporous SiO<sub>2</sub> was obtained by a surfactant-templated synthesis adapted from the Stöber method where the penta-twinned nanorods acted as the nucleation site. CTAB was used as surfactant and tetraethoxysilane as the silica source [158]. Samples for TEM were prepared by casting drops of ethanol suspension containing the penta-twinned Au@SiO<sub>2</sub> nanoparticles on a quantifoil carbon TEM grid. The grid was placed in a model 2020 Fischione Instruments tomography holder. Tilt series were recorded using a FEI Tecnai Osiris electron microscope at an operating voltage of 120 kV. The probe convergence semi-angle equaled 7 mrad and a camera length of 34 mm was selected to obtain incoherent image formation using a HAADF-STEM detector corresponding to inner and outer collection semi-angles of 150 mrad and 220 mrad, respectively. ADF-STEM images were acquired using a different detector present in the column. A camera length of 34 mm was used yielding inner and outer semi-angles of 35 mrad and 125 mrad, respectively. Tilt series of HAADF-STEM and ADF-STEM images were simultaneously recorded at angles ranging from +74° to -73° with a 3° increment. The projection images were aligned using a cross-correlation algorithm together with a manual tilt axis adjustment implemented in the FEI Inspec3D software [21]. Both tilt series were aligned using the same shifts and tilt axis adjustments. After additional processing, the tilt series were reconstructed via SIRT implementation of the ASTRA tomography toolbox [92, 159] with 100 iterations. For 3D visualizations, the Amira software was used. For the Au nanoparticle an iso-surface rendering was used and in order to visualize the silica a volume rendering was applied. Hereby, a low alpha-scale was used in order to obtain sufficient transparency such that the Au nanoparticle remains

visible.

### 5.1.2 Conventional Reconstruction

Investigation of the interface between the Au nanorod and the SiO<sub>2</sub> shell and determination of the size and the orientation of the pores, requires 3D characterization by electron tomography. Therefore, tilt series of HAADF-STEM images were acquired. Figure 5.1 a, presents a representative 2D HAADF-STEM image from the tilt series. When using HAADF-STEM, the signal is proportional to  $Z^n$  ( $1.6 < n < 2$ ),  $n$  depending on the collection angle of the (HA)ADF-STEM detector [11]. In practice, the collection angle can be tuned within a specific range by changing the camera length of a given detector. Even more flexibility is provided in modern TEM instruments in which more than one (HA)ADF detector is often available. It is therefore possible to optimize the contrast between different elements through a careful selection of the collection angles. In Figure 5.1 a,

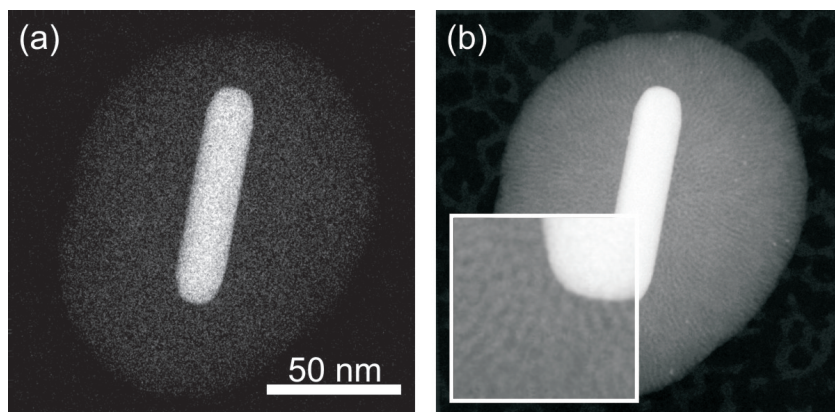


Figure 5.1: TEM image of a penta-twinned Au@SiO<sub>2</sub> particle. (a) The micrograph was acquired using HAADF-STEM. The core can be clearly seen but the intensity from the shell is too low. (b) The micrograph was acquired using ADF STEM, showing that the intensity from the SiO<sub>2</sub> shell becomes prominent.

the signal from the Au core is clear, but the intensity obtained from the shell is very weak due to the relatively low atomic number elements contained in SiO<sub>2</sub>. The inner and outer collection angles of the HAADF detector used during the

acquisition of the tilt series for electron tomography were 150 mrad and 220 mrad, respectively. The collection angle was optimized to avoid diffraction effects, but clearly no information on the SiO<sub>2</sub> shell can be obtained when using these images as an input for 3D reconstruction. In order to obtain information from Au and SiO<sub>2</sub> simultaneously, smaller collection angles should be used. In Figure 5.1 b, an ADF-STEM image is depicted, which was acquired using an ADF detector resulting in inner and outer collection angles of 35 mrad and 125 mrad, respectively. It is clear that using this set-up, both the Au core and the SiO<sub>2</sub> shell can be visualized. The Au nanorod appears to be homogeneously coated with the silica shell and one can observe that the shell has a porous morphology. A full tilt series of ADF-STEM images was acquired under the same conditions and used as an input for 3D reconstruction. A 3D visualization of the reconstruction, as well as an orthoslice through the reconstruction, is presented in Figure 5.2. Orthoslices through the 3D reconstruction along the XZ and XY orientations (Figure 5.2 a, b) clearly show the presence of artifacts, which can be seen as dark areas and streaks in the vicinity of the Au nanorod. Also in the 3D visualizations (Figure 5.2 c, d), the artefacts are obvious. These artefacts appear due to a combination of the reasons listed below.

1- Diffraction contrast: artefacts originate because of the crystalline nature of the penta-twinned Au nanorod. Such type of metal streak artefacts are also encountered in X-ray computed tomography [150, 151] and caused by non-linear attenuated projection data.

2- High contrast in 2D projection images: high contrast artefacts are often encountered when using fiducial Au markers in biological tomography series. These artefacts were already described in a previous study [160]. Here, a high contrast difference is present between the Au nanorod and SiO<sub>2</sub> in the HAADF-STEM images. Since the observed artefacts may cause loss of information or may lead to misinterpretation, it is extremely challenging to obtain reliable 3D results for core-shell hybrid materials using conventional electron tomography. When selecting an optimal value for the collection angle, a compromise is needed between optimal contrast, produced by the atomic number of coexisting elements, and the

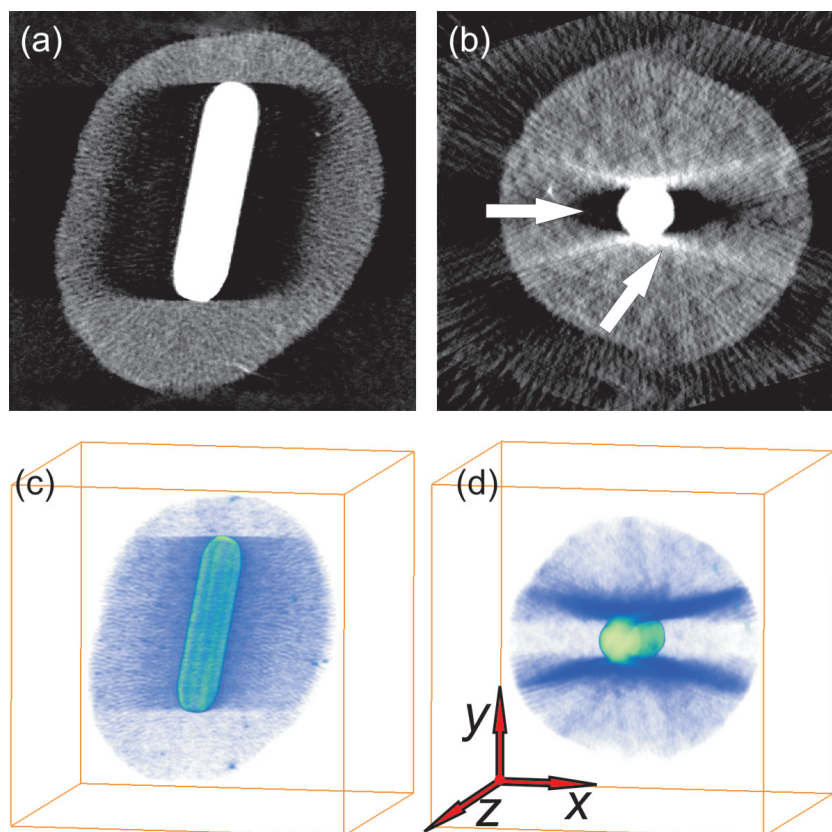


Figure 5.2: Reconstruction of a penta-twinned Au@SiO<sub>2</sub> particle, using an ADF-STEM tilt series. (a,b) Slices through the silica coated penta-twinned Au nanorod viewed in XZ (a) and XY (b) orientations. Dark and streaking artefacts can be observed in the vicinity of the Au nanorod and are highlighted with white arrow. (c,d) Volume renderings of the ADF-STEM reconstruction viewed along XZ and XY orientations. The Au nanorod is depicted in light green and the surrounding silica is shown in blue. Although information from silica is present in the reconstruction, the resolution of the reconstruction is limited by the artefacts.

minimization of diffraction contrast.

### 5.1.3 Optimization of acquisition of tilt series

A possible approach to solve the problem is the acquisition of two tilt series for this type of core-shell nanoparticles: one series with a low collection angle to obtain information from the part of the sample containing low atomic number elements and a second series at higher collection angle such that diffraction effects are removed. However, such an experiment would acquire double the amount of incoming electrons and as a consequence, the morphology of the hybrid structure might be different during the acquisition of the first and second tilt series because of electron beam damage. This will be especially problematic in the case of sensitive materials, such as the mesoporous shell surrounding the Au nanorod. We here overcome this limitation by exploiting the flexibility of modern TEM instruments that enable one to collect multiple (HA)ADF-STEM series simultaneously, by using different (HA)ADF detectors at the same time. In this manner, one is able to simultaneously collect two tilt series while keeping the necessary electron dose the same. As such, this multi-mode approach is very dose-efficient. This multi-mode approach is very dose-efficient, as one is able to collect 2 images while keeping the necessary electron dose the same. Tilt series were simultaneously acquired using an ADF detector with inner and outer collection angles of 35 mrad and 125 mrad and a HAADF-STEM detector using inner and outer collection angles of 150 mrad and 220 mrad, respectively.

### 5.1.4 Optimization of the 3D reconstruction procedure

To remove the artefacts that appear in the ADF-STEM tilt series, we propose an approach in which the complete Au nanoparticle is removed from the ADF-STEM projection images. First, the pixels corresponding to the Au nanorod were selected in the projection images of HAADF-STEM by applying a threshold. According to their histograms, the projection images were segmented into 3 regions; the core, the shell and the surrounding C grid. As expected, the intensity values

of the core were found to be higher in comparison to the shell. The threshold for masking was set to a value slightly higher than the intensity of the areas consisting of  $\text{SiO}_2$ . For other types of hybrid materials, this threshold value can be similarly determined, based on the compound with lowest intensity. Subsequently, the selected pixels for the Au core were removed from the projection images (Figure 5.3 b) and replaced by a new intensity value as described below. In order to

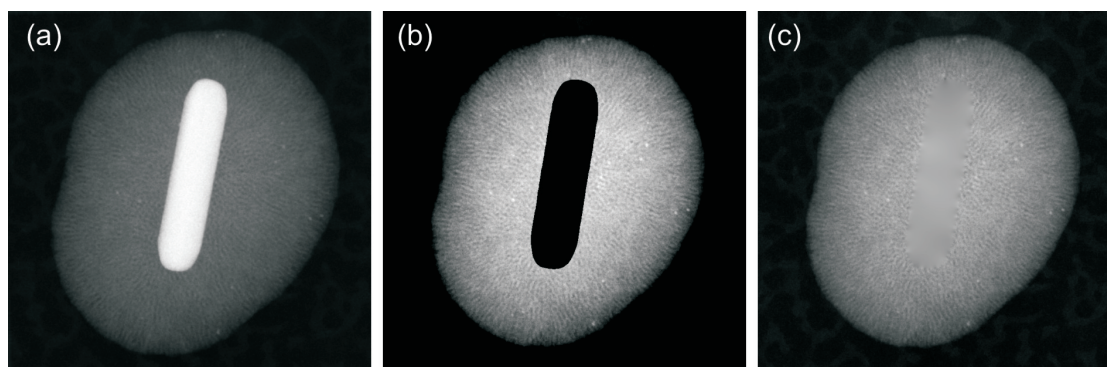


Figure 5.3: Different steps toward the optimization of the reconstruction of a ADF-STEM tilt series. (a) Micrograph acquired using ADF-STEM (b) After image segmentation, the pixels corresponding to the Au nanorod in  $\text{SiO}_2$  were removed. (c) Final image after the inpainting procedure. The removed pixels were replaced by the surrounding texture.

achieve maximum correspondence between the selected (removed) region for the Au nanorod and its surrounding in each of the projection images, a technique known as inpainting was applied. This approach replaces the absent information by a continuation of the texture of the surrounding area. Inpainting has already been applied successfully in the field of X-ray tomography [161, 162] and during cryo electron tomography experiments in order to reduce metal originated artifacts [161]. In this paper, we focus on the inpainting method implemented in the MatLab software package. More technical details can be found in [163, 164]. This function fills the missing data (represented by a pixel mask) by iteratively propagating the available information at the boundaries into the area in which data are missing. In order to obtain a good correspondence between the recreated (inpainted) region

and the SiO<sub>2</sub> shell, 200 inpainting iterations were applied. This procedure was performed for each projection image of the tilt series separately, one representative image being depicted in Figure 5.3 c.

The processed tilt series was then used as an input for 3D reconstruction using the SIRT algorithm implemented in the ASTRA toolbox. Slices through the 3D reconstruction based on the modified ADF-STEM series are presented in Figure 5.4 a, b, along the XZ and XY orientations, respectively. From these reconstructions, the porous structure of the shell is clearly observed and artefacts are greatly reduced as compared to Figure 5.2. Finally, the 3D HAADF-STEM and ADF-STEM reconstructions are combined into one single visualization using the AMIRA software. The result of this procedure is presented in Figure 5.4 c and d. In Figure 5.4 c, the reconstruction of the Au nanorod was obtained via HAADF-STEM tomography. The surrounding SiO<sub>2</sub> was reconstructed using ADF-STEM tomography with an optimization of reconstruction algorithm. After careful investigation, we conclude that the pores are mainly originating from the surface of the Au nanorod and the pore channels are oriented in a radial manner. Furthermore, the quality of the reconstruction enables us to estimate the average pore size, which was determined to be 2.5 nm ( $\pm 0.4$  nm). Using the optimized approach for electron tomography that we present here, we were able to minimize the loss of information in the vicinity of the Au nanorod, yielding a full characterization of the 3D structure of the Au-SiO<sub>2</sub> hybrids. Such 3D investigation could not be obtained using conventional tomography. One can expect missing information in the final SiO<sub>2</sub> reconstruction because of the removal of the Au nanorod from the projection images. Indeed, due to the overlap of Au and SiO<sub>2</sub> in the 2D HAADF-STEM projection images, the removed pixels contain information from both Au and SiO<sub>2</sub>. Nevertheless in the final reconstruction the effect of such missing information was not prevalent. A likely explanation is that the removed intensity values were strongly dominated by the contribution of the intensity originating from the Au nanorod and a minor contribution from SiO<sub>2</sub> expected to be present. In addition, when the nanoparticle was tilted to higher/lower tilt angles, the previously removed information could be retrieved in the subsequent projections. We could consider that the effect of

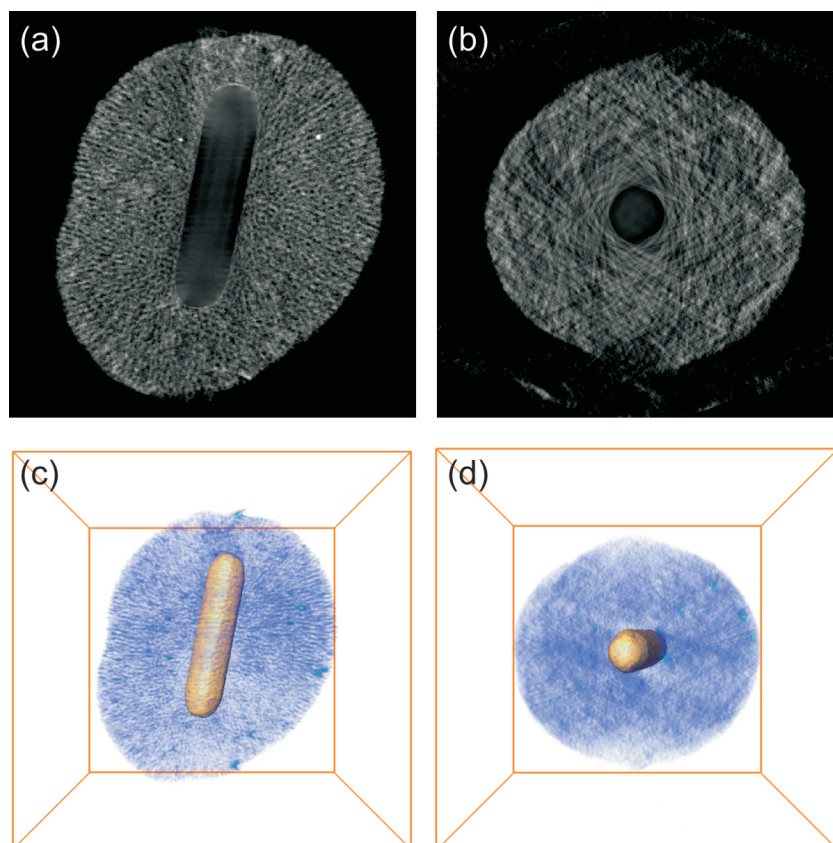


Figure 5.4: 3D reconstruction of penta-twinned Au@SiO<sub>2</sub> using ADF-STEM and HAADF-STEM tomography. The Au nanorod and silica shell are displayed in yellow and blue, respectively. The reconstruction was obtained using HAADF-STEM tomography for the Au core and by ADF-STEM for the silica shell. (a) Orthoslices through the mesoporous silica shell, viewed in XZ and XY orientation. After optimization of reconstruction, dark and streaking artefacts (see Figure 5.2 a, b) were eliminated. (c,d) Volume renderings of the ADF-STEM reconstruction viewed along XZ and XY orientations. The pores and channels can be clearly visualized.

the procedure we propose here is equivalent to the effect of a small missing wedge. Given the dominant nature of the artefacts as presented in Figure 5.2, the effect of removing pixels that contain intensity from the  $\text{SiO}_2$  is much less significant.

## 5.2 Conclusions

In this study we proposed a novel approach to reconstruct the structure of hybrid core-shell nanomaterials. Both the acquisition and reconstruction during an electron tomography experiment were hereby optimized. Tilt series were acquired in a dose-efficient manner by simultaneously collecting images using 2 different (HA)ADF-STEM detectors. Furthermore, an advanced masking and inpainting procedure was applied to remove artifacts that are present in a conventional tomography reconstruction. In this manner, we were able to reliably characterize the structure of mesoporous silica coated penta-twinned Au nanorods. It must be noted that the methodology we propose here is generally applicable to a broad range of core shell hybrid nanostructures, each structure in Figure 1.17 was reconstructed using the proposed methodology.

## Chapter 6

# Characterization of Plasmonic-Porous Hybrid Nanostructures

**This chapter is based on:**

M.N. Sanz-Ortiz, K. Sentosun, S. Bals, L.M. Liz-Marzan, Templated growth of surface enhanced raman scattering-active branched gold nanoparticles within radial mesoporous silica shells, *ACS nano*, 9(10), (2015), 10489-10497

G. Zheng, S. de Marchi, V. Lopez-Puente, K. Sentosun, L. Polavarapu, I. Perez-Juste, E.H. Hill, S. Bals, L.M. Liz-Marzan, I. Pastoriza-Santos, Encapsulation of Single Plasmonic Nanoparticles within ZIF-8 and SERS Analysis of the MOF Flexibility, *Small*, 12(29), (2016), 3935-3943

G. Zheng, Z. Chen, K. Sentosun, I. Perez-Juste, S. Bals, L.M. Liz-Marzan, I. Pastoriza-Santos, J. Perez-Juste, M. Hong, Shape control in ZIF-8 nanocrystals and metal nanoparticles@ ZIF-8 heterostructures, *Nanoscale*, 9(43), (2017), 16645-16651

In this chapter, structural characterization of plasmonic Au nanoparticles coated

---

with mesoporous SiO<sub>2</sub> and ZIF-8 is presented. The synthesis and the optical characterization of the samples was carried out at the Bionanoplasmonics Laboratory, CIC biomaGUNE and Departamento de Quimica Fisica in Universidade de Vigo (Spain). I was responsible for the 2D and 3D characterization and hereby used the technique that I developed in chapter 5.

## 6.1 Introduction

The characterization of hybrid core-shell nanoparticles consisting of plasmonic and porous components using 2D and 3D TEM techniques is discussed in this chapter. First, a brief explanation on the investigated nanostructures (Au-Ag nanoparticles, mesoporous silica and metal organic frameworks) is presented. Results are discussed in two parts. In the first part, the characterization of mesoporous SiO<sub>2</sub> (silica) encapsulating Au or Au-Ag nanoparticles is discussed. The results of TEM characterization of ZIF-8 coated Au-Ag nanoparticle is presented in the second part.

### Au-Ag nanoparticles

Both Au and Ag exhibit plasmonic properties and by combining both metals, the LSPR response can be tuned [165, 166]. Since the plasmon resonance of Ag can be engineered to any wavelength in the visible spectrum by varying the shape, the use of Ag for plasmonic applications is of great value [167, 168]. The structure of bimetallic nanoparticles is determined by the distribution of the two components either corresponding to alloys or core-shell structures [169]. In particular, bimetallic nanoparticles which are formed with a core-shell structure often display improved physical properties [170]. Representative Au@Ag core-shell type nanoparticles are presented in Figure 6.1.

Nanoparticles with LSPR in the near-infrared (680-900nm) are of special interest since they allow applications in deep-tissue imaging due to low absorption of near infrared light by biological fluids [49, 171]. The combined properties of Au-Ag leads to enhanced shape control of the particles due to the presence of Au and plasmonic properties due to the presence of Ag. Hence, Au-Ag nanostructures are extensively studied because of their possible applications in SERS [172]. Here, both the structure and the growth mechanisms of bimetallic nanoparticles combined with mesoporous silica and metal organic frameworks is investigated. Given the often anisotropic and complex nature of the particles, the need for a characterization in 3D is obvious.

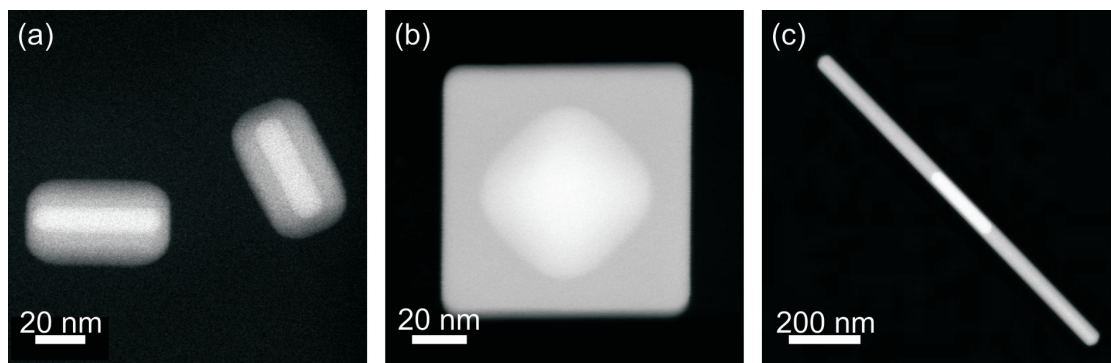


Figure 6.1: TEM images from Au@Ag nanoparticles. The Au nanoparticles yield higher intensity.

### Mesoporous silica

Silica is an attractive material for biomedical applications due to its chemical and physical stability and low cost. Porous silica nanoparticles with varying pore diameter and a hexagonal arrangement were synthesized for the first time at the University of California in Santa Barbara. These particles contain a connective pore system that enhances the surface area and the diffusion within the nanoparticle. Mesoporous silica was mainly designed to be a molecular sieve with well-adjusted pore diameter and pore channels which controls the diffusion of certain sizes of molecules. The most common types of mesoporous silica nanoparticles are known as SBA-X. SBA is an abbreviation of Santa Barbara Amorphous type materials and X refers to a specific pore structure and diameter [173, 174]. For SBA-type nanoparticles, a hexagonal pore structure is achieved for different pore diameters ranging between 2 and 30 nm.

Due to its adjustable pore size and structure, mesoporous silica is also used as a template for the growth of different metals and metal oxides [175, 176]. Moreover, filling the channels with a drug or cytotoxin or with methanol also led to their use as a drug carrier in biomedical applications [177–179] and in storage of methanol [180]. Mesoporous silica is furthermore applied in colloidal chemistry to enhance the colloidal stability of nanoparticles such as Fe [181] and Au (see Figure 6.2) [182] by encapsulating the nanoparticles.

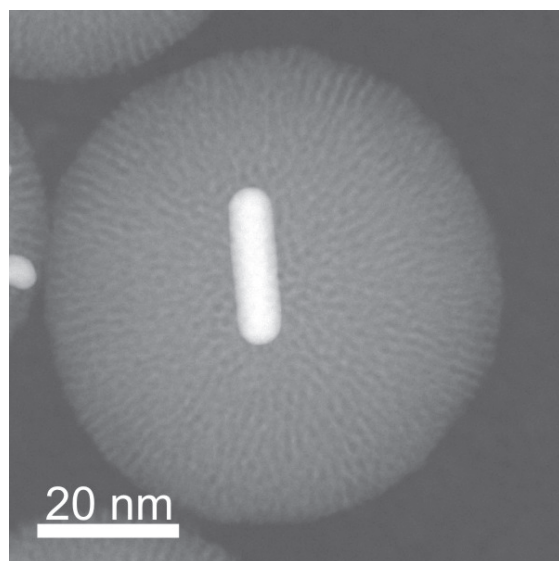


Figure 6.2: TEM image of a mesoporous silica with a Au nanorod.

The combination of mesoporous silica with plasmonic nanoparticles in a core-shell structure, is studied in this chapter. The characterization of the combination of an organic compound (silica) with an inorganic nanoparticle (Au or Au@Ag) is far from straightforward. A methodology to study both components in these complex nanostructures in a reliable manner is discussed in chapter 5.

### **Metal organic frameworks**

MOFs are open crystalline frameworks with permanent porosity, consisting of joined secondary building units (SBU) containing transition metal ions (connectors) with strongly bonding organic linkers (Figure 6.3). By combining different SBUs with organic linkers, thousands of different compounds can be synthesized [183]. Depending on the metal oxidation state, coordination numbers may vary between 2 and 7 which gives rise to coordination networks with different geometries. Combination of coordination networks in 3 dimensions yields a nanoparticle which is called a MOF. MOFs are studied because of their ultra-high porosity and extraordinary large pore opening which yields a very large surface area. Combining multi-functional MOFs into a single framework offers many opportunities for

the design of complex pores. By varying the SBUs or the organic linkers, different types of MOFs have been designed of which HKUST [184], MIL [185], UiO [186] and the zeolitic imidazolate framework (ZIF) [187] are most studied. MOFs, are generally, named by the department where they were synthesized, therefore, the MOF names do not represent a particular abbreviation. The SBU unit, organic linker, pore size and surface area of the aforementioned MOF types are presented in Table 6.1. Among them, ZIF is a well-known and broadly studied MOF subcategory. They are of special interest due to their high chemical stability in water, aqueous alkaline solution and organic solvents [188–191]. For the synthesis of the ZIFs, the zeolite structure is imitated. Zeolites are crystalline microporous aluminosilicates based on  $\text{AlO}_4$  and  $\text{SiO}_4$  tetrahedra that are connected by shared oxygen atom bridges. For the synthesis of ZIF-8, Si-O-Si bonds in zeolites are imitated by generating Metal-imidazolate ligand-Metal bonds (usually a  $\text{Zn}^{2+}$  or  $\text{Co}^{2+}$  are used as metal). A difference of ZIFs in comparison to zeolites is that the metal centers in ZIFs are stable, however, the imidazolate ligands are not. They can flip and rotate which determines the pore size. This brings extra flexibility for modification of pore size of the MOF nanocrystals in comparison to zeolites.

Table 6.1: Comparison of different MOF types in terms of organic-inorganic compounds and pore size and surface area.

	SBU unit	Organic Linker	Pore size(Å)	*BET surface area $\text{m}^2/\text{g}$
HKUST-1	$\text{Cu}_3$	Benzenetricarboxylic	9.0	692.2
MIL-53	$\text{Al}(\text{OH})$	Benzenetricarboxylate	7.1	1203
UiO-66	$\text{Zr}_6\text{O}_6$	Benzenetricarboxylate	6.0	833.4
ZIF-8	Zn	2-methylimidazolate	11.6	1413

\*Brunauer-Emmett-Teller (BET) is a measure that explains the physical adsorption of gas molecules on a solid surface and establishes the basis for an analysis technique for the measurement of the specific surface area of materials.

The adjustable porous structure has made MOFs perfect candidates for fuel

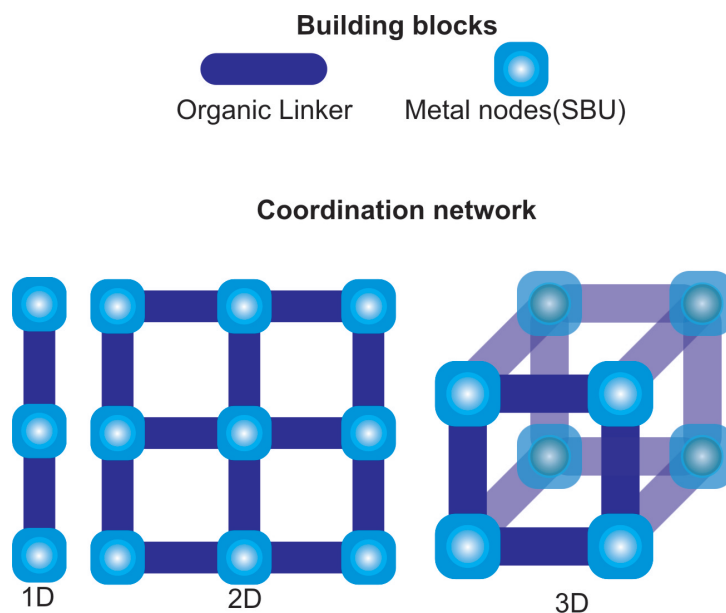


Figure 6.3: Build-up of a 3D MOF showing the building blocks and coordination network.

storage and gas molecule adsorption. Kitagawa et al. reported in 1997 the reversible adsorption of gas molecules such as  $\text{CH}_4$ ,  $\text{N}_2$  and  $\text{O}_2$  in MOF structures, which was exclusively known in zeolites and organic porous materials [192]. Moreover, ZIF-8 can be used in gas phase catalysis applications such as CO oxidation. As mentioned previously, small Au nanoparticles with a size of 2-3 nm can be used in oxidation of CO. Therefore, such small nanoparticles can be embedded in ZIF-8 structure. In this manner, the aggregation and migration of Au nanoparticles is prevented by the ZIF-8 structure and as a consequence, these combined nanostructure can be used in the aforementioned catalysis applications [187]. Combination of functional nanomaterials is hence an efficient route to increase the application field of nanostructures. In section 6.3, the combination of ZIF-8 nanoparticles with plasmonic Au-Ag nanoparticles is discussed. The growth of ZIF-8 on Au-Ag nanoparticle is investigated using different surfactants and the resulting morphology is studied by TEM.

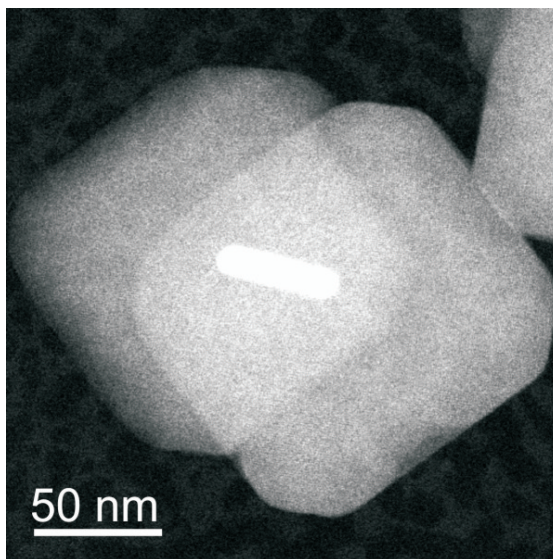


Figure 6.4: A ZIF-8 nanoparticle in cubic morphology with a Au nanorod.

## 6.2 Introduction to Au / Au-Ag nanoparticles encapsulated with mesoporous silica

As discussed previously, noble metal nanoparticles such as Au and Ag are extensively used as substrates for SERS applications because of their plasmonic properties [55, 193–196]. The plasmonic performance largely depends on various factors, such as the composition of the nanoparticles, their size and shape, the surrounding medium and its aggregation state. Aggregated nanoparticles are often used to improve plasmonic enhancement through hot spot formation, but the aggregation process is often uncontrolled and results in poor reproducibility [197], so the use of nanoparticles with an optimized and uniform morphology is highly preferred [72, 198]. On the other hand, improving the colloidal stability of these plasmonic nanoparticles (even for clusters) is typically achieved via encapsulation of the nanoparticle within an oxide (silica, titania) or polymer shell [199]. Moreover, by covering each particle with a (porous) shell, hot spot formation may consequently be carried out in a more controllable manner. This may have the additional advantage of trapping analyte molecules inside the shell during synthesis,

improving control over their location around the particle [200]. The drawback in this case is again that the synthesis must be designed for each specific measurement. A more versatile family of SERS probes can be obtained by the use porous coatings [201], so that the metal particles remain protected from aggregation while their surface is still accessible to the analytes. This approach widens the potential applications of these plasmonic particles, since the porosity of the shell may lead to a size-selective detection of analytes. Importantly, biocompatible mesoporous coatings such as silica have been widely proposed for drug delivery applications [9, 143].

With the aim of improving both the enhancement efficiency, the reliability and reproducibility of SERS measurements, branched Au nanoparticles coated with a mesoporous silica shell are synthesized, which are used both as templates for seeded growth of branches from the Au cores and traps for analyte adsorption. Such nanoparticles provide unique properties since they consist of different functional nanomaterials and understanding the morphology and growth mechanism of each component is essential for further engineering. Using 2D and 3D electron microscopy methods the conformity of the coating, pore size and distribution of the different components of the mesoporous silica coated plasmonic Au / Au-Ag is investigated.

### **6.2.1 Growth of mesoporous silica on Au nanoparticle**

In this study, Au nanoparticles with different morphologies of spheres, single-crystal nanorods, pentatwinned nanorods, and nanotriangles, capped with CTAB are used as nucleation sites. Representative BF-TEM images of the different nanoparticles after growth of mesoporous silica shells are displayed in Figure 6.5 a-d. From these images, it is clear that the individual Au nanoparticles are covered by silica. However, from these images we cannot investigate structural aspects such as the pore distribution and size as well as the interface between the Au and the silica.

Further characterization of the 3D morphology of silica-coated Au particles is therefore performed using electron tomography. The core-shell structure of the

particles can be visualized by 3D HAADF-STEM [202]. However as discussed in chapter 5, for samples containing elements with both high and low atomic number  $Z$ , e.g. Au nanoparticles encapsulated by a mesoporous silica shell, artefacts are expected in the 3D reconstruction [203]. We therefore applied the methodology explained in the previous chapter. The tilt series for electron tomography in this section are acquired using a FEI Osiris electron microscope, operated at 120 kV, since silica is a beam sensitive material.

Visualizations of the 3D reconstruction of the silica-coated Au nanoparticles are presented in Figure 6.5 e-h. Analysis of the 3D reconstruction confirmed that the individual Au particles are uniformly covered by silica for each type of nanoparticle morphology. In all cases, non-aggregated nanoparticles with a homogeneous silica coverage and shell thickness are obtained (Figure 6.5). These results confirm that the conformal encapsulation of these structures by mesoporous silica is successful for different morphologies. Moreover, the 3D reconstructions revealed the radial orientation of the pores in the silica shell. The pore size, pore diameter and interpore wall thickness of the silica shell is determined by analyzing 2D slices through the 3D reconstructions. In total, 200 measurements based on 4 different reconstructions are performed to obtain statistically relevant results, yielding an average pore size of  $2.1 \pm 0.3$  nm and an average silica wall thickness of  $2.4 \pm 0.4$  nm. The histograms of the measurements are shown in Figure 6.6. In addition, EDX mapping revealed that no residual Au is dispersed in the channels of the mesoporous silica and thereby confirming a perfect separation between the Au core and the silica shell (see Figure 6.7).

It can be concluded that the silica pores can be used as a molecular sieve where molecules larger than  $2.1 \pm 0.3$  nm are not able to penetrate towards the Au nanostructure. It is reported that such type of properties are useful for controlled drug delivery [177–179]. A clear advantage of the accessibility of the Au nanoparticle through the radial pores is that Au-catalyzed chemical reactions can take place selectively at the cores.

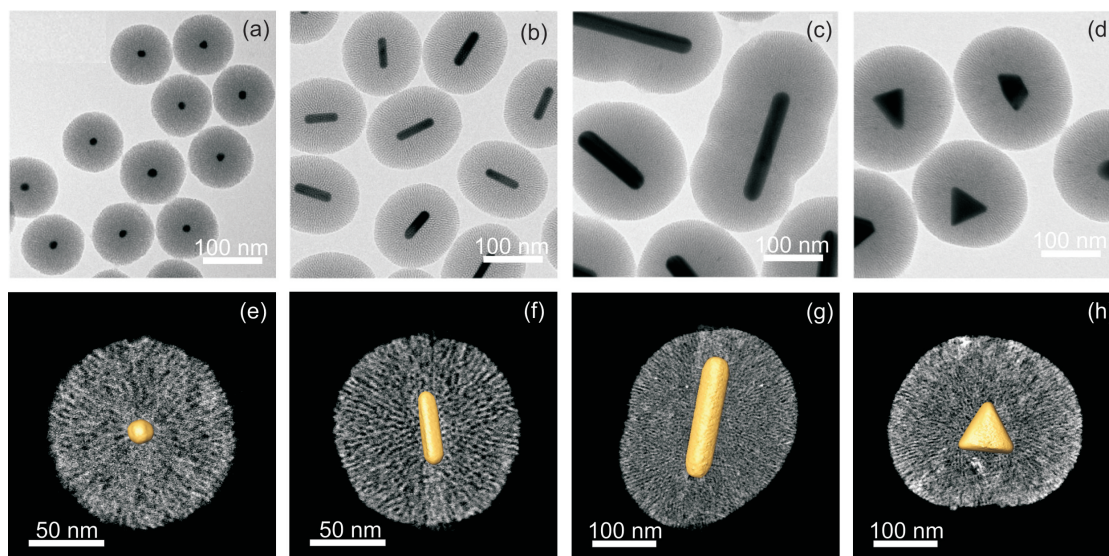


Figure 6.5: 2D and 3D TEM characterization of hybrid nanostructures containing Au nanoparticles with various shapes: nanospheres (a, e), single-crystal nanorods (b, f), penta-twinned nanorods (c, g), and nanotriangles (d, h). The radial mesopores in the silica shells can be observed in the visualizations of the 3D reconstructions in the bottom row (the Au nanoparticle and the silica shell are displayed in yellow and white, respectively).

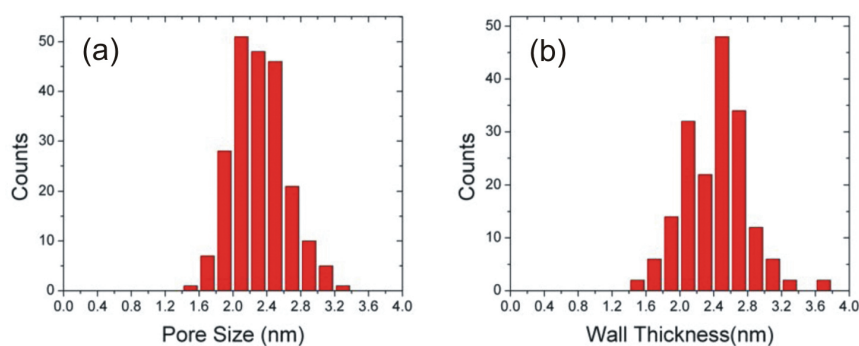


Figure 6.6: Pore size (a) and wall thickness (b) histograms for the mesoporous silica shells obtained from 200 measurements based on 4 different reconstructions. The average silica pore size is  $2.1 \pm 0.3$  nm and the average silica wall thickness is  $2.4 \pm 0.4$  nm.

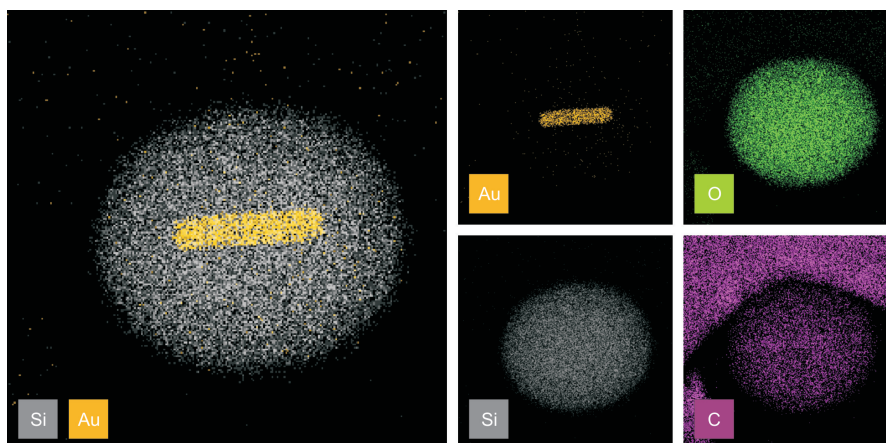


Figure 6.7: Qualitative analysis of the core-shell structure via EDX mapping. Evidence is obtained of the presence of Si, Au and O and in addition perfect separation between Au and silica is observed in complimentary to electron tomography results.

## 6.2.2 Overgrowth of Ag through the pores

In this section, the overgrowth of Ag layer over the Au cores through the radial pores of the silica is aimed. This is of great interest because of the superior plasmonic performance of Ag. Ag coating is performed by in situ reduction of  $\text{Ag}^+$  ions by ascorbic acid, a resulting nanostructure is shown in Figure 6.8 a. Here, EDX mapping is performed to investigate the presence and location of Ag after the in situ reduction. The EDX map presented in Figure 6.8 b confirms the presence of Ag in the nanostructure which suggests a Au/Ag core-shell type structure. However, in order to confirm this hypothesis, a 3D investigation by HAADF-STEM needs to be carried out. In Figure 6.8 c, a 3D visualization of the nanostructure is shown (Au nanorod, Ag coating and mesoporous silica is in green, blue and red, respectively) from which we can confirm the Au-Ag core-shell morphology. The overgrowth of  $\text{Ag}^+$  on Au is further investigated by the use of high resolution HAADF-STEM imaging to study the interface of Au and Ag. Perfect epitaxial growth of Ag on the Au nanorod is observed since the d values of Au and Ag are very close to each other which is clearly shown in Figure 6.8 d, in

which both the Au core and Ag shell are oriented along the [110] zone axis (the  $d$  values in the literature for [111] planes of Au is 2.355 Å and for Ag is 2.3591 Å). The corresponding optical changes are shown in Figure 6.8 e and are in agreement with previous observations using non-silica coated nanorods [204]. A blue shift of the longitudinal surface plasmon mode is observed for the silica coated Au-Ag nanorod in comparison to silica coated Au nanorods due to the overgrowth of Ag.

### 6.2.3 Overgrowth of Au through the pores

Next, it is aimed to grow Au tips from the central Au cores, using the radial mesopores as templates, which are expected to enhance the SERS performance through the formation of regions with high electric field enhancement at sharp features, while localizing analyte molecules at such hot spots. The use of mesoporous silica as a template to grow metal branches from nanoparticles has been previously demonstrated for Au nanoparticles embedded in mesoporous silica films [156]. The overgrowth reaction is based on a modification of a synthesis method for Au nanostars, which involves the reduction of  $\text{HAuCl}_4$  in the presence of Ag ions [77]. By using the silica-coated particles as seeds, the radial silica channels could act as templates, so that thin and short Au wires would branch out from the surface of the Au cores, regardless of the initial core shape.

In Figure 6.9 a-d, BF-TEM image of the resulting nanostructure after the overgrowth are shown. From these 2D images, it is clear that the overgrowth resulted in tip formation at the starting Au nanoparticle regardless of the initial core shape (a:sphere, b:rod, c:pentatwinned, d:nanotriangle). In order to study the pores of the resulting nanostructures, electron tomography needs to be applied. The way the Au branches grow their way out of the cores through the silica channels can be clearly appreciated from 3D visualizations of different structures after tip growth (Figure 6.9 e-h). The tip width of the branches could be extracted from the 3D reconstructions and is estimated to be  $3.5 \text{ nm} \pm 1.0 \text{ nm}$ , i.e., slightly larger than the pore size, probably because the Au branches push their way through the channels during growth. However, it can also be observed that pores remained stable after Au branching.

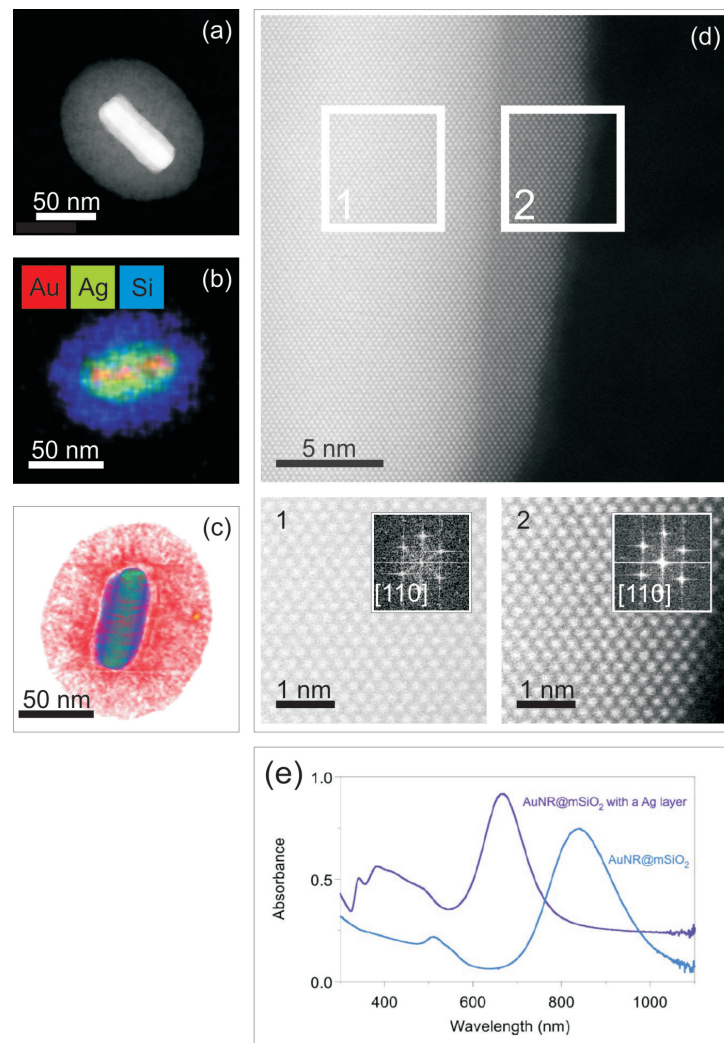


Figure 6.8: Single-crystal Au nanorods covered with a mesoporous silica layer with radial pores, after in situ growth of a Ag layer through the silica pores. (a) a HAADF-STEM image, (b) EDX map, (c) Visualization of 3D reconstruction, (d) high resolution HAADF-STEM image showing epitaxial growth of the Ag layer on the Au core. The crystallinity and the epitaxial relation of the Au core and the Ag shell can be observed in the high-resolution images and corresponding FT (acquired from the areas labeled as 1 and 2 in panel d). (e) Extinction spectra of single crystal Au nanorods coated with mesoporous silica, before and after growing a Ag layer over the Au cores.

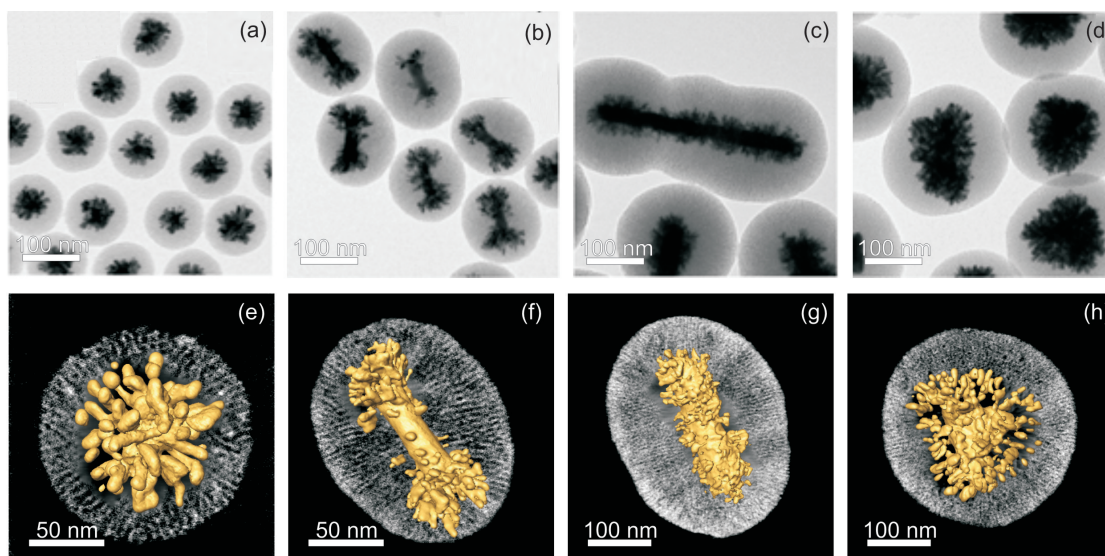


Figure 6.9: BF-TEM and 3D TEM characterization of hybrid nano structures containing different Au nanoparticles coated with mesoporous silica, after growing Au tips through the silica channels: nanospheres (a, e), single-crystal nanorods (b, f), penta-twinned nanorods (c, g), and nanotriangles (d, h). All the images in the left panel are obtained at the same magnification. In the right panel, a visualization of the 3D reconstructions for a representative nanoparticle of each type is displayed, where the radial nature of both the channels and the Au branches can be observed.

Although branching is achieved on various types of nanoparticle cores, a significant difference is noticed between the single crystal nanorods and other morphologies. In the case of spheres, penta-twinned nanorods, and nanotriangles, branching occurred uniformly from spots on the entire particle surface which can be observed in Figure 6.9 e, g, h. For single crystal Au nanorods, the branching mainly occurred at the tips, which can be observed in the visualization of the 3D reconstruction (Figure 6.9 b). This anomaly is however in accordance with the results shown in Figure 2.9 a, b and a report [205], regarding the growth of tips from bare (non-coated) single-crystal Au nanorods and is likely related to the presence of Ag or Ag bromide preferentially on the lateral facets of the nanorods which will hinder the Au overgrowth of these facets.

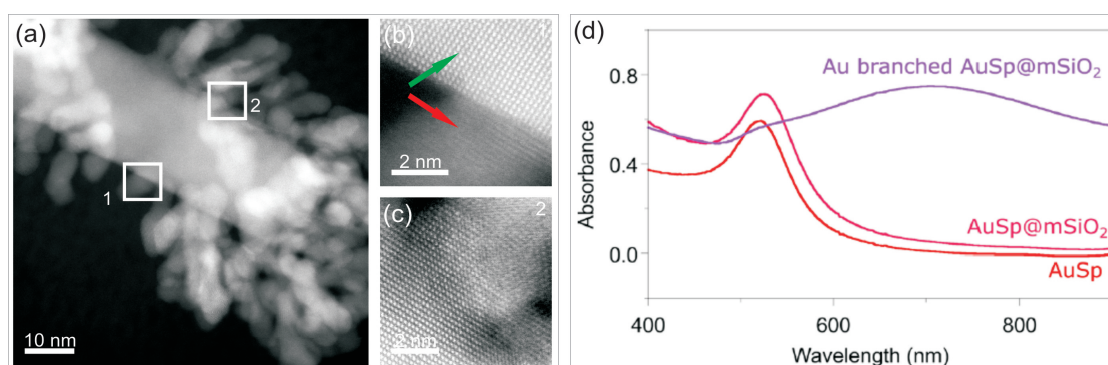


Figure 6.10: High resolution HAADF-STEM images after tip growth are acquired from the sample with (a-c) single crystal nanorod, (d) evolution of the extinction spectra for the sample with Au spheres stabilized in 0.1 M CTAB, after mesoporous silica shell growth, and after templated tip growth.

The growth mechanism is also investigated at the atomic scale using high resolution HAADF-STEM (the high resolution images are acquired using a FEI-Titan microscope operated at 300kV). In Figure 6.10 a-c, a Au nanorod after overgrowth is presented, which shows that the grown tips have a different crystal orientation in comparison to the seed Figure 6.10 b and c. In the high resolution image depicted in Figure 6.10 b, the green arrow depicts the seed nanorod which is oriented in [100] zone axis. The red arrow displays the grown tip which is clearly not in the

same zone orientation. Likewise in Figure 6.10 c, the grown tip is clearly in a different orientation in comparison to Au core. The same result is also observed for the nanosphere, penta-twinned nanorod and nanotriangle.

From the optical point of view, the growth of silica on bare Au nanospheres results in slight red shift of the LSPR in comparison to bare Au nanospheres since the surrounding dielectric has changed (see Figure 6.10 d, plotted in pink for Au@mSiO<sub>2</sub> and in red for bare Au nanosphere). Moreover, the growth of tips on a Au nanoparticles has been reported to result in the red shift and broadening of the corresponding LSPR [77]. This effect is indeed observed here, as exemplary shown for spheres in Figure 6.10 d. This effect has important consequences regarding potential applications of these nanoparticles in biological systems, as electromagnetic field enhancement can be achieved by irradiation in the near-infrared, i.e., in the biological transparency window. Here a question may rise why the overgrowth of Au resulted in tips and branches while the overgrowth of Ag yielded a Au@Ag nanorod. In the first case, before the overgrowth of Au, a thermal treatment was applied on Au-silica structures. This increased the stability of mesoporous silica therefore they can be used as a template during growth. In the latter case, thermal treatment for silica was not carried out on Au-silica structures, thus resulting in partial damage of the mesoporous silica structure, which is likely responsible for the uniform silver coating.

#### 6.2.4 SERS performance of branched Au nanoparticle

Finally, the SERS performance of branched mesoporous silica-coated Au spheres in solution is tested. Colloidal dispersions containing a fixed Au concentration ( $[Au^0] = 0.25 \text{ mM}$ ) are employed for SERS detection of two model analytes, which are specifically chosen not to chemically bind to Au: Crystal Violet and Nile Blue. It is observed that the detection of concentrations as low as  $10^{-9} \text{ M}$  for crystal violet and  $10^{-8} \text{ M}$  for Nile blue. Moreover, the superior performance of branched nanoparticles for SERS detection in water is obtained, where SERS spectra of crystal violet ( $10^{-6} \text{ M}$ ) in the presence of nanospheres with and without tips are compared, using in both cases a Au<sup>0</sup> concentration of 0.25 mM. Even though (for

the same concentration of metal) the number of branched nanoparticles per unit volume is estimated to be  $\sim 6$ -fold smaller than that of spherical particles, the signal obtained from the former is 1 order of magnitude more intense than that from the latter.

### **6.2.5 Conclusions on silica coated Au / Au-Ag nanostructures**

Advanced electron tomography is used to investigate hybrid silica - Au/Au-Ag nanostructures. The mesopores in the silica shells are used as templates for the seeded growth of Au tips branching from the surface of the Au cores which is clearly revealed by electron tomography reconstructions. Furthermore, the method is successfully implemented for Au nanoparticles with various morphologies, thereby showing a wide versatility and general application. Next, the overgrowth of Ag and Au results in layer growth and tip growth, respectively, where electron tomography revealed the resulting morphology clearly. The radial structure of the pores and the growth of the tips through them favor the localization of analyte molecules in close proximity to hot spots, as indicated by SERS measurements. All these features render these particles a particularly versatile family of SERS probes: easily tunable, stable in various media, and suitable for biological applications. It should be noted that that it is only because of the developments in chapter 5 that it is possible to investigate these hybrid structures.

### 6.3 Introduction to MOF coated Au-Ag nanomaterials

As discussed in section 6.1, the combination of multi-functional nanoparticles is efficient for enhanced physical and chemical properties. Based on International Union of Pure and Applied Chemistry classification, when the pore size in a material is smaller than 2 nm, such type of materials are classified as microporous: Zeolites and MOFs are typical examples of such materials. Among them, MOFs have been widely applied in energy, catalysis and drug-delivery [206, 207]. Rationalization of the chemical and physical properties of the MOFs relies on structural aspects such as their size and morphology but also on the composition [208, 209]. Typically, the synthesis procedures give rise to bulk MOF powders with relatively large crystal size, random shape, and poor monodispersity, but control over the MOF crystal morphology at the nanometer scale is a pre-requisite in certain fields such as optoelectronics or biomedical applications [210]. Different approaches have been developed to control the size and morphology of the MOFs, which are mostly focused on controlling the kinetic growth processes [211]. The main synthetic strategy that has been explored so far to control the MOFs morphology is based on the coordination modulation method, in which the addition of different additives could be used to control the crystal growth through influencing the coordination equilibrium [212, 213]. For instance, Tsuruoka et al. added acetic acid as competitor to modulate the coordination equilibrium of metal ions and organic linkers [214]. The acetate-copper interaction plays a crucial role in determining the reaction rate and the crystal morphology, where, through oriented attachment the morphology of the MOFs could be tuned from cubic to rod-shape.

Similarly, Umemura et al. have shown that by controlling the concentration of modulator, it is possible to obtain an octahedron-cuboctahedron-cube morphological transition [215]. The presence of lauric acid as modulator controls the crystal growth along the [111] and [100] directions that eventually dictates the final shape. Alternatively, the presence of surfactant molecules have been also reported to act as modulators [216]. The role of surfactant as capping agents and its adsorption to

specific crystal facets could also induce a morphology evolution. Pan et al. demonstrated that the presence of cationic surfactants could change the morphology of ZIF-8 MOFs from a truncated cube to a rhombic dodecahedron [217]. The different adsorption affinity of the surfactant molecules towards the  $\{100\}$  and  $\{110\}$  facets has been claimed as the main reason to modulate their relative growth rate.

In this study, the influence of different surfactants such as CTAB and tris (hydroxymethyl) aminomethane (TRIS) on the growth of ZIF-8 nanostructures is investigated by electron tomography.

### 6.3.1 CTAB mediated ZIF-8 growth

The individual encapsulation of Au-Ag nanoparticles within ZIF-8 crystals involves: (i) the synthesis of plasmonic nanoparticles of a desired size, shape, and composition, which will be stabilized with quaternary ammonium surfactant, (ii) followed by the nucleation and growth of ZIF-8 crystals on the metal surface here at the presence of 0.0460 mM CTAB.

Figure 6.11 a displays a BF-TEM image of individual Au-Ag nanoparticles encapsulated by ZIF-8. Based on the TEM analysis, it is clear that the nanoparticle is individually encapsulated within ZIF-8 crystals. The characterization of ZIF-8 encapsulated nanoparticles is complemented by X-ray diffraction analysis. Figure 6.11 b shows the experimental X-ray diffraction pattern of dried Au nanorod inside ZIF-8 nanoparticles, together with simulated patterns for Au and ZIF-8 crystals. Both patterns, originating from the ordered porous structure of the ZIF-8 shells ( $2\theta = 5^\circ\text{-}35^\circ$ ) [190] and that from the Au cores ( $2\theta = 35^\circ\text{-}50^\circ$ ) are identified. This confirmed the sodalite zeolite-type crystal structure of the ZIF-8 shells and the well-defined peaks in the X-ray diffraction pattern indicate a high crystallinity. SAED is additionally performed on a stand-alone ZIF-8 cube. Since the ZIF-8 morphology changes quickly during electron beam irradiation, the electron dose is kept to a strict minimum. SAED reveals that ZIF-8 nanoparticles are single crystalline with a cubic structure. The SAED pattern in Figure 6.11 c, recorded along the  $[100]$  zone axis, is in agreement with the X-ray diffraction results.

Moreover, to reveal the distribution of the chemical components in the hybrid

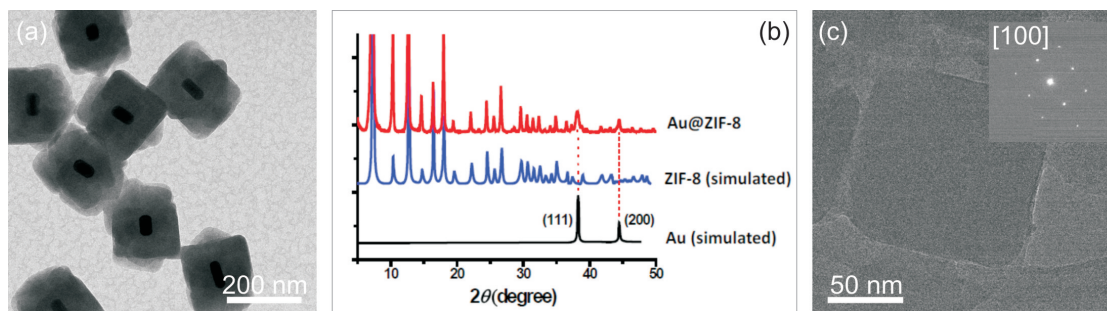


Figure 6.11: (a) Overview BF-TEM images of nanoparticles, (b) powder X-ray diffraction pattern of ZIF-8 coated Au nanorods (red line) and the simulated patterns for ZIF-8 (blue line) and Au (black line). The simulated diffraction peaks generated using the ordered porous structure of ZIF-8 crystals at  $2\theta = 5^\circ\text{-}35^\circ$  and by Au at  $2\theta = 35^\circ\text{-}50^\circ$  are both observed for the Au nanorod@ZIF-8 nanostructure. All of the prominent peaks for the ZIF-8 shells, including 011, 002, 112, 022, 013, and 222, correspond to those of pure ZIF-8 crystals, (c) BF-TEM image together with a SAED from a single crystal ZIF-8 crystal.

particles, EDX mapping is performed, using a Super-X EDX detector which is implemented on a FEI Osiris microscope operating at an accelerating voltage of 120 kV. Figure 6.12 shows that Au and Ag are located only at the core whereas Zn is homogeneously distributed in the shell corresponding to ZIF-8 (Figure 6.12 a-d). The EDX analysis furthermore demonstrates a sharp separation between the Au rod, the Ag shell, and the ZIF-8 matrix, i.e., no intermixing of the elements is detected at the interfaces.

The 3D morphology of the individual nanoparticles is characterized by advanced electron tomography as explained in chapter 5. Multiple detectors (HA)ADF are utilized simultaneously during the acquisition of the tilt series of projection images which are collected over an angular range from  $-74^\circ$  to  $73^\circ$  with a  $3^\circ$  tilt increment. In this manner, heavy and light elements in the same sample are both visualized. As already mentioned, this technique can be considered as dose efficient, which is of great importance to image electron beam sensitive materials in 3D [203]. Visualizations along different directions of the 3D reconstruction are

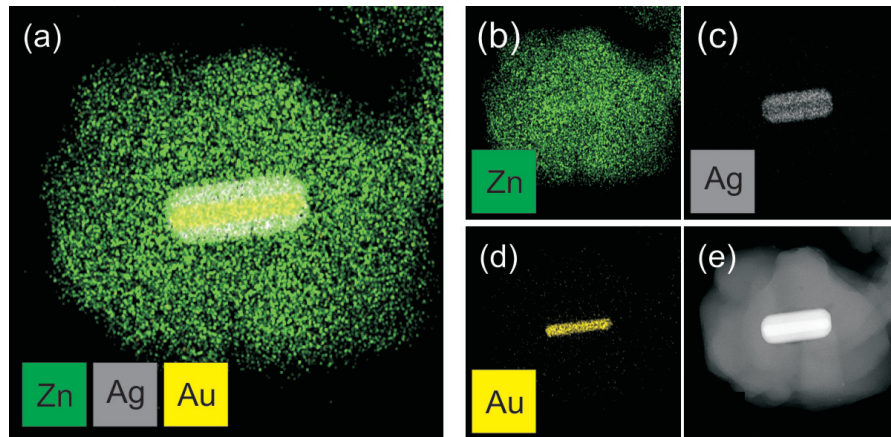


Figure 6.12: (a)-(d) EDX elemental mapping of an Au-Ag@ZIF-8 nanoparticle and (e) the corresponding ADF-STEM image.

presented in Figure 6.13 a-c. The ZIF-8 shell is depicted in orange, whereas Ag is imaged in gray and Au in purple. The 3D reconstruction reveals that the plasmonic Au-Ag nanoparticle is entirely encapsulated with ZIF-8. The morphology of the coating could be ascribed to multiple ZIF-8 nucleations and/or attachment on the metal nanoparticle surface. Then, further growth of separate nuclei continued in different directions.

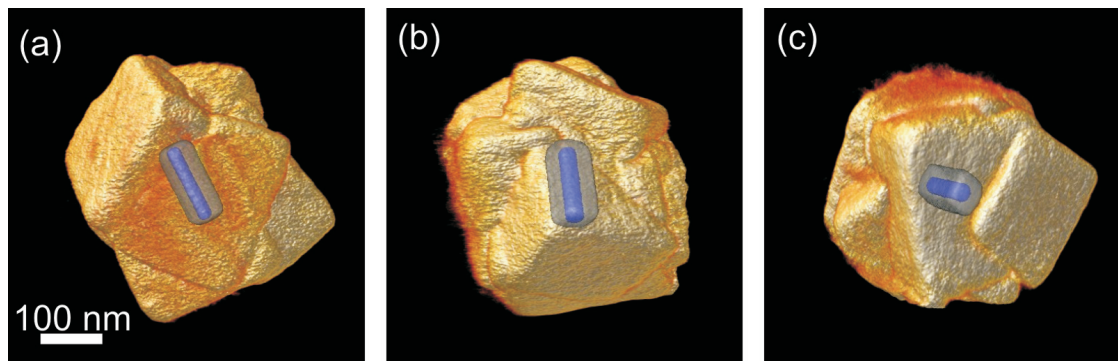


Figure 6.13: (a-c) Visualizations of the 3D reconstruction from different orientations.

The influence of CTAB on ZIF-8 growth is explained by Pan et al. [217]. It is shown in the paper of Pan that if no surfactant is used, a rhombic dodecahedron

with 12 {110} facets occurs. When the CTAB ratio in the solution is increased to 0.0025 wt% truncated rhombic dodecahedron with {100}, {110} and {111} facets are obtained. Further increment of CTAB to 0.01 % resulted in truncated cubic morphology with {100} facets. The reason for such difference is based on the interaction energies of the different facets which is given in Table 6.2. When no CTAB is present, the growth rate of {100} facets is very fast which results in rhombic dodecahedron morphology. When CTAB is added to solution, their interaction with {100} facets is stronger than the other facets. The strong interaction between CTAB molecules with {100} facets hinders the growth in that direction and leads to first truncated rhombic dodecahedron and finally truncated cubic morphology. The same phenomena also fits to the observations in this study where cubic morphology of the ZIF-8 nanoparticles with {100} facets in different orientation is clearly recognizable (see Figure 6.13).

In Figure 6.14 a and b, orthoslices through the reconstruction of ZIF-8 nanoparticles accompanied with 3D isosurface rendering of Au-Ag nanoparticle is presented. It can be clearly observed (highlighted with arrows) that gaps between the ZIF-8 cubes are present. Such gaps probably occur due to ZIF-8 cubes which are grown in different direction and do not fit one to the other. A schematic illustration is presented in Figure 6.14 c. It should be noted that such observations can only be realized by electron tomography and the methodology explained in chapter 5 to reduce the artifact at the hybrid interfaces in the 3D reconstruction. It can be

Table 6.2: The calculated interaction energies obtained through molecular dynamics simulations at 25 C° [217]

surfaces	Interaction energies kcal mol <sup>-1</sup>
{100}	-774.56
{110}	-394.91
{101}	-104.21

concluded that the presence of CTAB as surfactant led to the formation of ZIF-8 nanocrystals with a cubic morphology through the preferential stabilization of the {100} facets. The dimensions of the cubes vary between 110 - 130 nm.

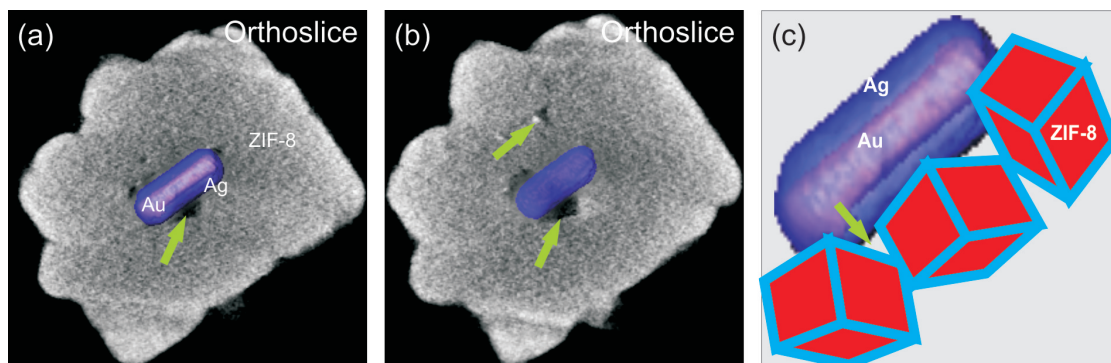


Figure 6.14: (a,b) Orthoslices from 3D reconstruction, (c) illustration of growth of ZIF-8 on Au-Ag nanoparticle.

### 6.3.2 CTAB/TRIS mediated ZIF-8 growth

In this section, we studied the combined influence of both modulators, CTAB and TRIS, on the morphology of ZIF-8 particles. Hence, the growth of the ZIF-8 on Au-Ag nanoparticle is performed in the presence of 0.07 mM CTAB together with 50mM TRIS.

A BF-TEM image from an isolated ZIF-8 nanoparticle without a Au-Ag core is depicted in Figure 6.15 a. In the presence of TRIS together with CTAB the particle developed a burr-puzzle morphology. Additionally, SAED is performed on the ZIF-8 nanocrystal which is shown in Figure 6.15 b. The particle displayed in Figure 6.15 a is oriented along the  $[111]$  direction with respect to the electron beam. Additional reflections (one of them highlighted with a green arrow) are also observed, suggesting that the particle is polycrystalline.

Next, electron tomography is performed to study the 3D structure of the hybrid nanoparticles. The acquisition and reconstruction are performed as explained in section 6.2.1. Visualizations along different orientations of the 3D reconstructions are presented in Figure 6.16. The ZIF-8 shell is depicted in orange, whereas Ag is imaged in gray and Au in purple. In total, 3 different particles are studied and it can be concluded that all Au-Ag nanorods are entirely encapsulated by a ZIF-8 shell. The CTAB/TRIS mediated growth resulted in ZIF-8 spikes which have various sizes. The thickness of the spikes is measured using slices through the 3D

reconstruction and is estimated to vary between 25 nm and 60 nm.

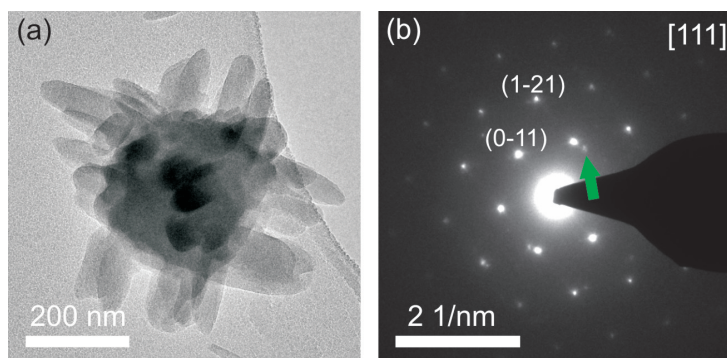


Figure 6.15: BF-TEM image of a burr-puzzle crystal and its corresponding diffraction pattern.

In the presence of capping agents such as CTAB or TRIS with CTAB, particles are obtained with cubic or spiky morphology, respectively. To understand the affinity of molecules on different facets of ZIF-8, intermolecular interactions between ZIF-8, TRIS and CTAB is calculated using MOPAC2012 [218]. Selected minimized representative conformations and interaction energies are shown in Figure 6.17. The obtained negative values clearly indicate the existence of stabilizing interactions between ZIF-8 and TRIS for different geometries and relative orientations. Although the interaction energies are similar, they indicate that adsorption on  $\{111\}$  facets is slightly preferred for TRIS molecules. Hence, it can be concluded, the adsorption of CTAB and TRIS on ZIF-8 takes place preferentially on  $\{100\}$  and  $\{111\}$  facets, respectively. This probably results in a growth direction of mainly in  $\{111\}$  facets, which yields the morphology in Figure 6.16. For deciphering the nanostructures for certain applications, controlling the nanoparticle morphology is of great importance, this study showed the influence of different surfactants to direct the growth of ZIF-7 nanoparticles on plasmonic Au-Ag nanoparticles.

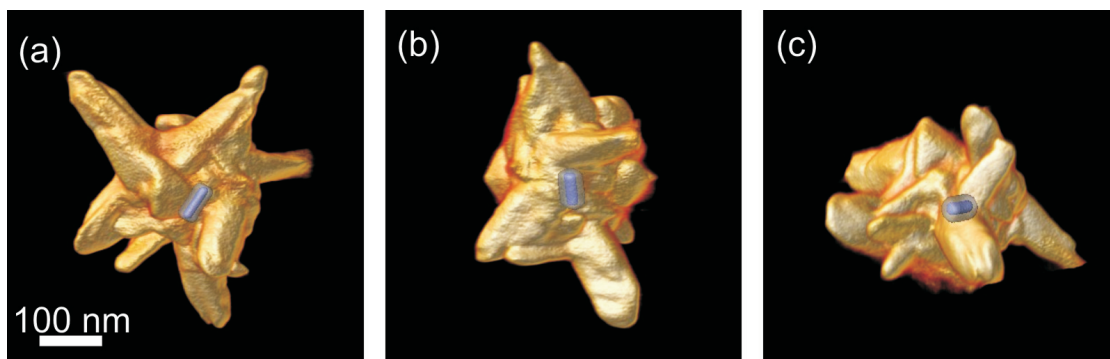


Figure 6.16: Visualization of 3D reconstructions from ZIF-8 nanoparticle encapsulating Au-Ag nanoparticle from different orientations.

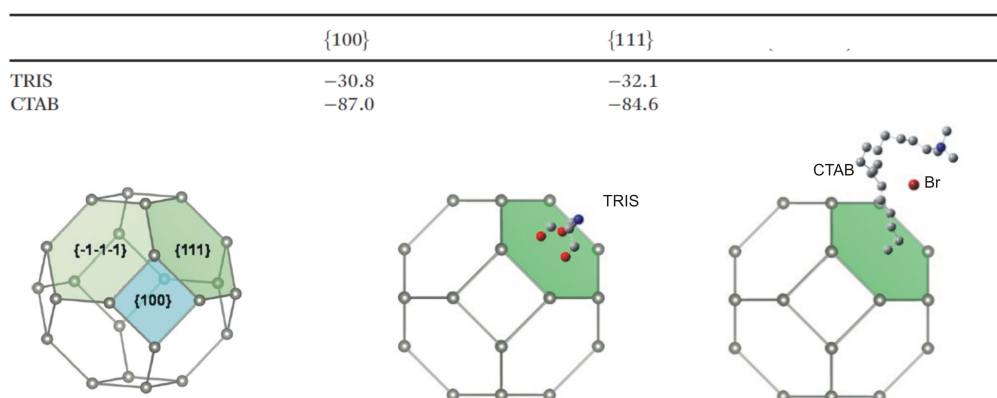


Figure 6.17: Minimized intermolecular interactions between the {100} and {111} facets of ZIF-8 and a unit of TRIS or CTAB [8] are presented. A unit model of ZIF-8 containing 708 atoms was defined and a large number of geometrical optimizations for different orientations between ZIF-8 and a monomer of surfactant CTAB and TRIS were performed. The unit for interaction energies is kcal mol<sup>-1</sup>.

### 6.3.3 Conclusions

In summary, a 3D analysis is performed on ZIF-8 nanocrystals which are grown on Au-Ag nanoparticles using different surfactants. It is observed that the use of different surfactants results in a different ZIF-8 growth and a preferential adsorption to certain facets. While CTAB molecules adsorb preferentially to  $\{100\}$  facets, leading to the growth of ZIF-8 with a cubic morphology, TRIS molecules stabilize preferentially onto the  $\{111\}$  facets and give rise to nanocrystals with spiky morphology. Optimized electron tomography enabled us to study the complex particle structure in 3D, which can be used for the optimization of the synthesis methods for ZIF-8 nanocrystals with a better shape control. This is of great importance in a number of applications such as catalysis, gas sensing and storage.

During the characterization of hybrid nanoparticles made of plasmonic and porous nanoparticles such as ZIF-8 and mesoporous silica, an important limitation is the degradation of nanostructures during the electron tomography experiment. To reduce the degradation, one needs to reduce the electron dose for the experiment. In the next chapter, a methodology which can be used to reduce electron dose during an electron tomography experiment is presented.



## Chapter 7

# Artifact Reduction Based on Sinogram Interpolation for the 3D Reconstruction of Nanoparticles

**This chapter is based on:**

K. Sentosun, I. Lobato, E. Bladt, Y. Zhang, W.J. Palenstijn, K.J. Batenburg, D. Van Dyck, S. Bals, Artifact Reduction Based on Sinogram Interpolation for the 3D Reconstruction of Nanoparticles Using Electron Tomography, *Particle & Particle Systems Characterization*, 34(12), (2017), DOI: 10.1002/ppsc.201700287

## 7.1 Introduction

In the previous chapter, characterization of electron beam sensitive mesoporous silica and ZIF-8 nanoparticles is discussed, such materials require novel approaches to reduce the beam necessary for electron tomography reconstruction. A possible way to do this is to reduce the number of projections. This chapter is devoted to a novel methodology where high quality reconstructions can be obtained even using an even smaller number of projections in comparison to conventional routes.

Typically, a tilt series of projection images is acquired over a tilt range of  $\pm 70^\circ$ - $80^\circ$  with a tilt increment of  $2^\circ$ . Unfortunately, for beam sensitive materials such as ZIF-8, it is far from straightforward to acquire projection data every  $2^\circ$  since the electron beam may induce changes in the morphology or even sample damage during the acquisition. To avoid this, the number of projection images is often reduced during the experiment, leading to degradation of the reconstruction quality. Over the last decade, different reconstruction techniques have been developed that yield superior results for such limited tilt series [34, 42, 44, 153]. These reconstruction techniques typically try to exploit prior knowledge about the reconstructed object. The discrete algebraic reconstruction technique uses prior knowledge about the gray levels during the reconstruction whereas compressive sensing based reconstruction techniques exploit the sparsity of the object in a given basis [34, 44, 153]. However, these methods are not always applicable, due to the lack of prior knowledge. An alternative method to improve the reconstruction quality is by increasing the sampling rate through sinogram interpolation [219–223]. For X-ray computed tomography, sinogram interpolation methods were already successfully applied to minimize streak and ring artifacts [220]. In this chapter, we will start by showing the benefits of sinogram interpolation for electron tomography using phantom objects and then this method will be applied for different experimental TEM datasets.

## 7.2 Methodology

### 7.2.1 Radon space and sinogram

In order to simplify the description of the methodology, we consider a two dimensional object represented by the function  $f(x, y)$  which is shown in Figure 7.1 a. Then its Radon transform  $p(t, \theta)$  is given by [224];

$$p(t, \theta) = \int_{-\infty}^{\infty} \int_{-\infty}^{\infty} f(x, y) \delta(t - x \cos \theta - y \sin \theta) dx dy \quad (7.1)$$

Where  $t$  and  $\theta$  are the distance and the projection angle of the center of rotation, respectively. For a single point source  $f(x, y) = \delta(x - x^*, y - y^*)$ , the Radon transform is given by;

$$p(t, \theta) = \delta(t - x \cos^* \theta - y \sin^* \theta) dx dy \quad (7.2)$$

The Radon transform of an object is often referred to as a sinogram because the transform of an off-center point source in real space corresponds to a sine wave in Radon space. Indeed, when a point object in real space  $(x, y)$  is tilted around an axis, a sine wave  $(\theta, t)$  is generated in the sinogram (see Figure 7.1 b). Since an object consists of many point objects, the Radon transform of an object consists of overlapping sine waves with different amplitudes and phases. By acquiring a higher number of projection images, a higher sampling of the sinogram is achieved. If the object is imaged along all projections, then the inverse Radon transform yields the original object. In experiments, we can only take a limited number of projection images (i.e. sparse sinogram Figure 7.1 c) which yields a reduction of the reconstruction quality of the object [150].

A reconstruction of an object can be obtained by filtering each sinogram column with a ramp filter to correct for uneven sampling of the spatial frequencies [20, 225], and then backprojecting it along the projection angles. To overcome the problem of limited number of projections, we present a sinogram interpolation method. The methodology of our approach is schematically illustrated in Figure 7.2. The method is composed of three main stages: (i) preselection of the sine waves based

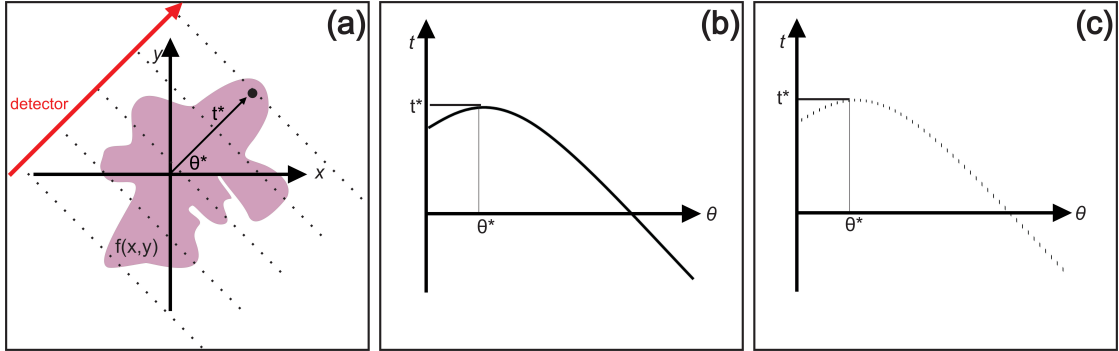


Figure 7.1: (a) 2D object of which a point source corresponds to a sine wave in Radon space (b). In case less projections are available, the sine wave will be sparse (c).

on a threshold, (ii) interpolation and/or extrapolation of a sparse sine wave, (iii) normalization and then reconstruction.

In order to illustrate the main steps of the flowchart diagram, we will use a phantom object consisting of a homogenous sphere embedded in a homogeneous support (Figure 7.3 a). We assume projection data for a tilt range between  $\pm 90^\circ$  with a tilt interval of  $1^\circ$ . A slice through the 3D object, taken orthogonal to the tilt axis, is shown in Figure 7.3 b. The main steps of the flow chart diagram will be explained in the following sections in more detail.

## 7.2.2 Preselection of single sine waves

From Equation 7.2, it can be understood that every pixel in the reconstructed slice corresponds to a particular sine wave in the sinogram. Figure 7.3 c shows the calculated sinogram for the slice in Figure 7.3 b under the experimental conditions mentioned above.

The first step of our method consists of creating an empty matrix with a size equal to the size of the 2D projection images from the tilt series. Next, for each pixel in a slice, sine waves are calculated using Equation 7.2 hereby using the experimental projection angles ( $\theta$ ). A representative sine wave is presented in Figure 7.3 d. This sine wave was calculated for the red voxel in Figure 7.3 a

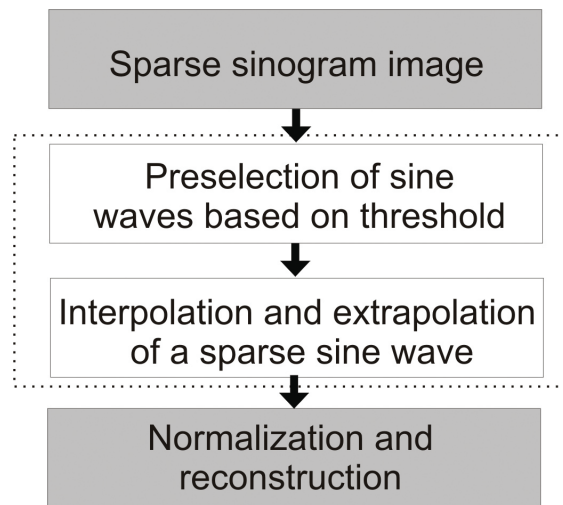


Figure 7.2: Flowchart of the sine wave preselection and interpolation procedure. The sine waves that are part of a recorded object are first identified based on a predefined threshold. Next, interpolation of the missing sinogram columns and the intensity values is carried out. After summing up all the interpolated sine waves and normalization, the resulting sinogram is used as input for the tomographic reconstruction algorithm. The sinogram interpolation procedure is applied slice by slice on a 3D datacube.

and corresponding pixel in Figure 7.3 b. Next, we determine if the sine wave corresponds to a pixel that is possibly part of the object, or if the pixel certainly belongs to the background. The calculated sine wave is therefore superimposed on the experimental sinogram (see Figure 7.3 e) and for every angle  $\theta$ , the intensity value of the sinogram at the position of the calculated sine wave is plotted (Figure 7.3 f).

As an example, two sine waves (depicted in purple and green) are presented in Figure 7.3 e. From Figure 7.3 f, it can be seen that the intensity values extracted based on the purple sine wave are relatively high for all values of  $\theta$ , whereas the values corresponding to the green sine wave are only significantly different from zero for a given range of  $\theta$ . From Figure 7.3 f, we then conclude that the purple sine wave possibly corresponds to a pixel of the object whereas the green sine wave corresponds to a pixel that certainly belongs to the background. This procedure is repeated for each pixel  $(x, y)$  in each slice of the reconstruction.

In general, we assume that pixels may belong to the object if the corresponding sine wave yields intensities above a certain threshold throughout the entire sinogram. This threshold is chosen to be slightly above the intensity value of the homogeneous support. In practice, one can estimate this intensity from a projection image acquired at  $0^\circ$ . The choice of the threshold may be somewhat arbitrary and may give rise to the wrong selection of some points just outside of the contour. However, the relative fraction of those pixels is small in comparison to the total number of internal pixels.

### 7.2.3 Interpolation of a sparse sine wave

Once a sine wave is considered as a part of the object and the intensity values of the sine wave in each experimental projection is obtained, the next step is to calculate the trajectory of the sine wave for the intermediate (unsampled) angles and to interpolate the intensity of the sine wave through the experimental points. This is performed by applying Equation 7.2 for the same point source, but with a finer tilt interval. Once the sine wave trajectory is determined, we estimate the intensity value of the sine waves by using a one-dimensional cubic interpolation

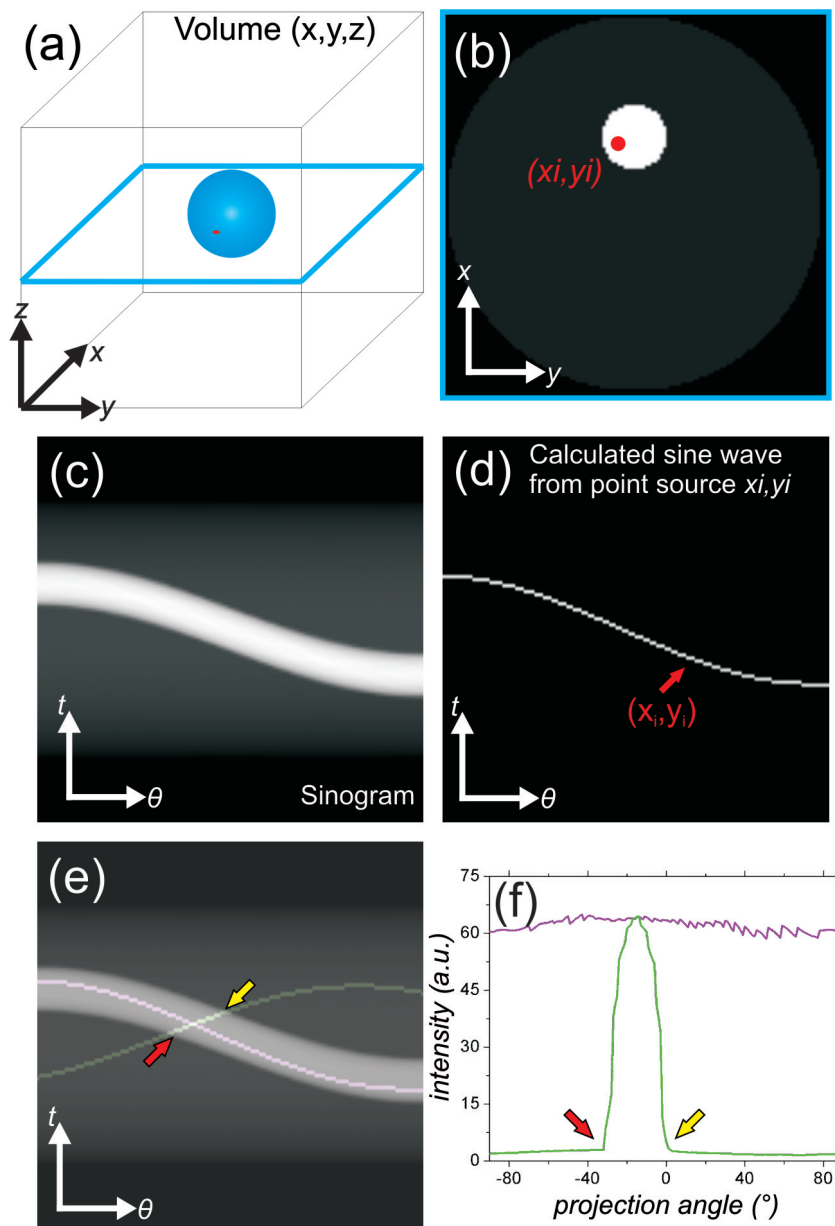


Figure 7.3: (a) A reconstruction volume with a highlighted reconstruction slice. (b) A reconstruction slice of the object to be reconstructed, (c) the corresponding (recorded) sinogram from the object, (d) a single sine wave from a point source  $(x_i, y_i)$ , (e) the overlay image of the sine waves with the sinogram, (f) the intensities of the sinogram along the two sine curves depicted in c.

method. In principle, the interpolation of the intensity can be performed for every calculated sine wave. However, we prefer to apply intensity interpolation only for the sine waves, which were classified as originating from the investigated object. In this manner, interference of the sine waves from different sources is reduced. Next, the total intensity (corresponding to the sum of all sine waves) for a specific coordinate is divided by the number of sine waves passing through that coordinate. In Figure 7.4a, we assume that projection images of the object in Figure 7.3 b are acquired over a tilt range of  $\pm 90^\circ$ , but now with a tilt interval between successive projections of  $30^\circ$ . Therefore, the sinogram is only based on 7 projections. The WBP reconstruction from the sparse sinogram is presented in Figure 7.4 b and it can be seen that the quality of this reconstruction is poor with the obvious presence of streak artifacts. To minimize such artifacts, we apply the methodology explained above. We first calculate the trajectories of the sine waves for all pixels in every reconstruction slice with a tilt range of  $\pm 90^\circ$  and an increment of  $30^\circ$ . An example of a preselected and interpolated of a single sine wave is presented in Figure 7.4 c and d, respectively. The final interpolated sinogram is presented in Figure 7.4 e and the corresponding reconstruction is shown in Figure 7.4 f. We hereby used the classical WBP scheme to judge the improvement of the reconstruction. Every artificially generated column in a sinogram actually represents a projection in real space. Increasing the number of projections by means of sinogram interpolation decreases the artifacts present in the reconstruction. It can be seen that streak artifacts in the reconstruction (Figure 7.4 f) are greatly reduced in comparison to Figure 7.4 b.

### 7.2.4 Reduction of missing wedge artifacts

Typically, a tilt series in an electron tomography experiment covers a range of approximately  $\pm 70^\circ$ - $80^\circ$ . Projections outside of this range are difficult to be recorded due to the shadowing from the single tilt holder or the TEM grid. This results in missing information in a sinogram and as a consequence, streaks artifacts or an elongation of the object are present in the final reconstruction. Here, we extrapolate the missing wedge intensity of the sine wave by exploiting the known

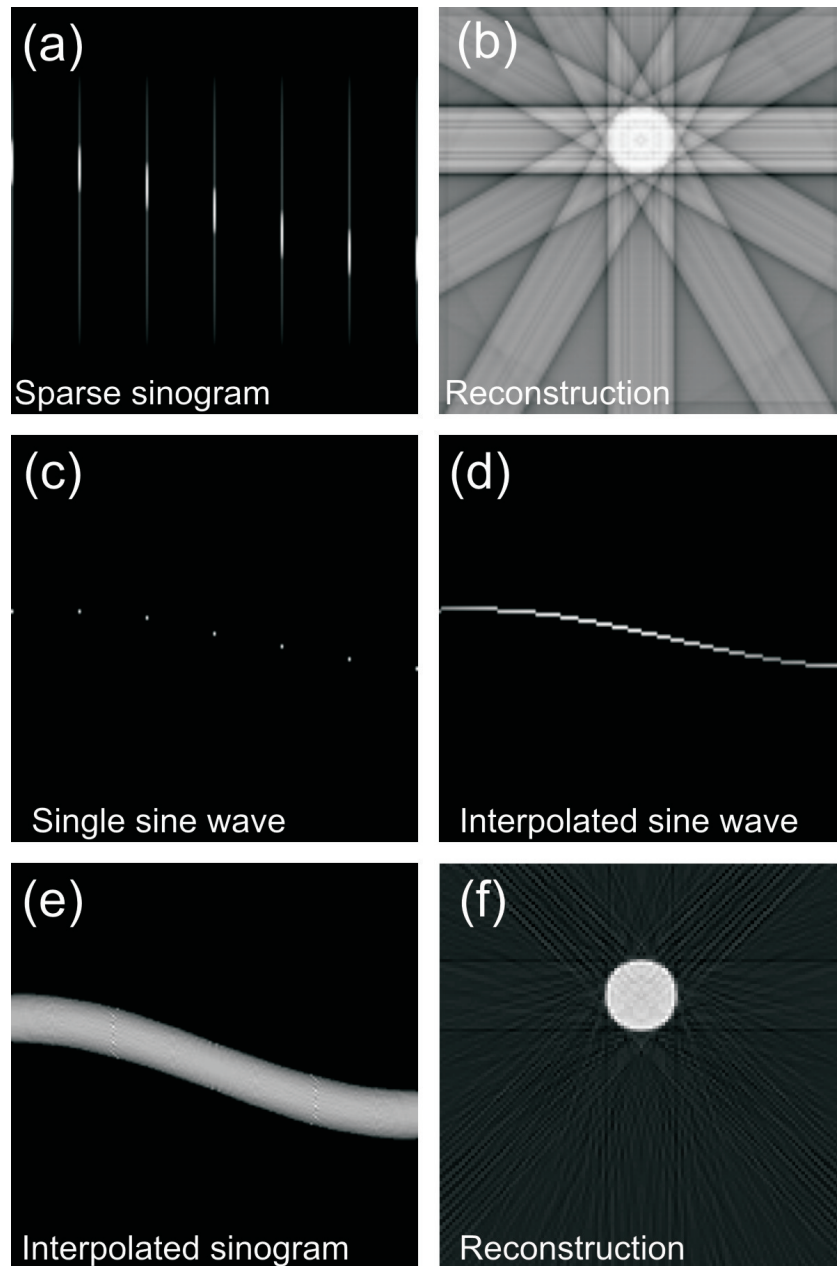


Figure 7.4: (a) A sparse sinogram obtained for a tilt series with a tilt range of  $\pm 90^\circ$  and tilt increment of  $\pm 30^\circ$ , (b) the reconstruction from the sparse sinogram, (c) individual sine wave selected from the sparse sine wave, (d) the sine wave in c after interpolation, (e) the interpolated sinogram, and (f) the reconstruction from the interpolated sinogram.

symmetry properties of the sinogram which is based on the fact that a projection from top to bottom is the mirror image of the bottom to top image [226]. In Figure 7.5 a, the sinogram based on projections obtained from the object in Figure 7.3b over a range of  $\pm 90^\circ$  is shown. The gray rectangles in this image indicate the information that will be lost when only a range of  $\pm 75^\circ$  is covered. The sinogram for this range is also illustrated in Figure 7.5 b.

To estimate the intensity values of the sine waves, a slightly different procedure is used in comparison to the methodology explained above. First, the sinogram is divided into two parts at  $0^\circ$  (indicated by a line in Figure 7.5 b). Next, the angular order is reversed in both parts, as illustrated in Figure 7.5 c. To overcome the mismatch, which is now present in the middle of the modified sinogram, one part of the sinogram (in this case part 2) is flipped with respect to the x-axis (see Figure 7.5 d) yielding a sinusoid with a different trajectory. The intensity values can now be extrapolated based on the intensities in the first and last acquired projection, corresponding to the projection at  $-75^\circ$  and a mirrored projection of  $+75^\circ$ . Next, a 1D interpolation was again employed to estimate the intensities in the missing wedge (see Figure 7.5 e). Next, the modification on the sinogram is reversed as illustrated in Figure 7.5 f, which shows good agreement with Figure 7.5 a (full tilt range). The reconstruction based on WBP using the sinograms from Figure 7.5 b and Figure 7.5 f are shown in Figure 7.5 g and Figure 7.5 h, respectively. To evaluate the results quantitatively, we calculated the elongation of the object before and after interpolation. The reconstructions in Figure 7.5 g, h are segmented by applying a threshold to obtain binary images. Here, the binary images are referred to as segmented images and the phantom in Figure 7.3 b is referred to as our reference.

The elongation is quantified along the vertical and the horizontal direction (Figure 7.5 g, h). After segmenting the reconstructions the length of the object is measured in both directions. The elongation is then calculated by dividing the length of the segmented object by the length of the reference object. In the horizontal direction, no elongation is observed for both reconstructions. However, in the vertical direction, an elongation of 10% is observed for the reconstruction pre-

sented in Figure 7.5 g. After the interpolation procedure (Figure 7.5 h) this number decreases to 3%. It is clear that the streak artifacts and the slight elongation of the object are reduced after the interpolation procedure.

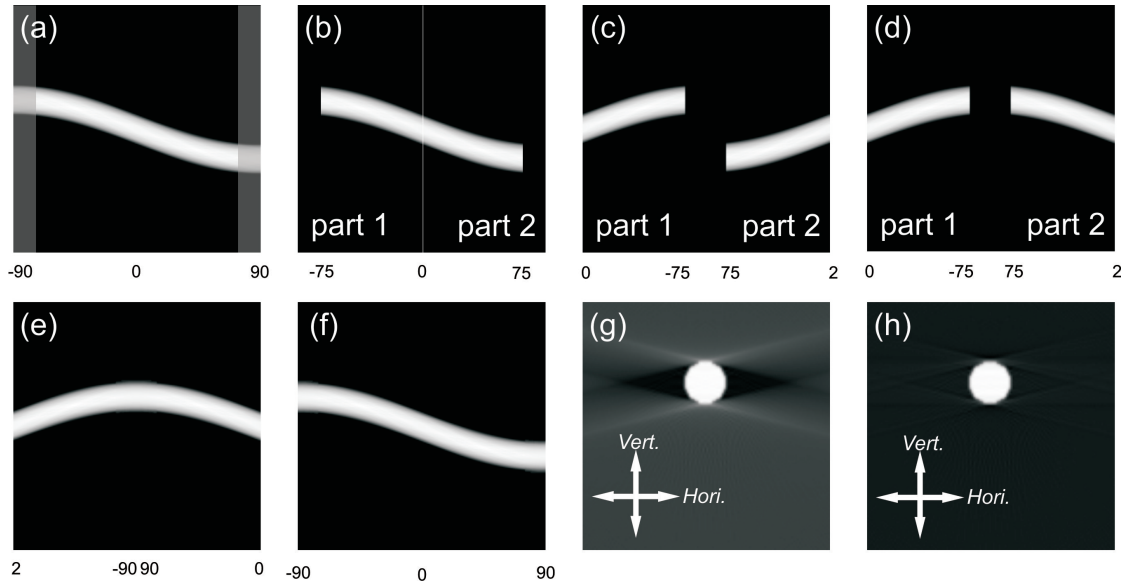


Figure 7.5: (a) The sinogram from an object with projections from  $\pm 90^\circ$ , (b) the same sinogram with missing information, (c) the sinogram with reordered angles, (d) the sinogram with the missing wedge information relocated, (e) after interpolation of the missing information and (f) reversed back sinogram, the reconstructions (g) with missing wedge and (h) after interpolation.

## 7.3 Experimental Results

### 7.3.1 Qualitative and quantitative comparison

In Figure 7.6 a, a HAADF-STEM image of a Au triangle is presented. A tilt series of similar images was recorded over an angular tilt range of  $\pm 76^\circ$  with a tilt increment of  $1^\circ$ . In the remainder, this tilt series is referred to as the “full tilt series”. By removing some projections from the tilt series, sparser tilt series are generated with an increasing tilt interval of 5, 10, 15, 20 and  $30^\circ$ . Next,

the sinogram interpolation method is applied and reconstructed using WBP as illustrated in Figure 7.6. The visualization of WBP reconstruction from full tilt series is presented in Figure 7.6 b and in Figure 7.6 c a reconstruction based on a sparse tilt series with a tilt increment of  $30^\circ$  is presented. The corresponding result after sinogram interpolation is presented in Figure 7.6 d. To evaluate the goodness of the reconstruction, we calculate the ratio ( $r$ ) of the misclassified voxels as follows:

$$r = \frac{|Vol_{rec}^{thr} - Vol_{ref}^{thr}|}{sum(Vol_{ref}^{thr})} * 100 \quad (7.3)$$

$Vol_{ref}$  here refers to the segmented volume of the full tilt series and  $Vol_{rec}$  stands for the segmented volume from sparse or interpolated tilt series. The volume of the segmented object,  $sum(Vol_{ref})$ , is equal to the summation of the voxels in  $Vol_{ref}$  and corresponds to the denominator in Equation 7.3. A threshold for segmentation of the volumes was determined from the reconstruction with a tilt increment of  $1^\circ$ . Figure 7.6 e shows the misclassified voxels, calculated for reconstructions with increasing tilt increment and clearly indicate a significant error, which can be largely avoided through the method we propose here. Even though our interpolation method is able to compensate for missing data, the dataset used as an input for WBP is still incomplete. We therefore expect that iterative algorithms such as SIRT may still improve the quality of the reconstruction. As a consequence of the sinogram interpolation, new projections are in fact artificially generated. These images can also be used as an input for a SIRT. The 3D visualization of the SIRT reconstruction from the full tilt series is presented in Figure 7.7 a. Visualizations of 3D SIRT reconstructions from the sparse tilt series and the tilt series after interpolation are shown in Figure 7.7 b and c, respectively. It is clear that the SIRT reconstruction from the sparse tilt series suffers from severe artifacts at the facets of the nanotriangle. The results based on the tilt series after interpolation (Figure 7.7 c) clearly shows an improved quality in comparison to Figure 7.7 b and the morphology of the nanoparticle is in good agreement with the SIRT reconstruction from the full tilt series. Furthermore, the quality of the SIRT reconstruction is improved in comparison to the WBP reconstruction using the

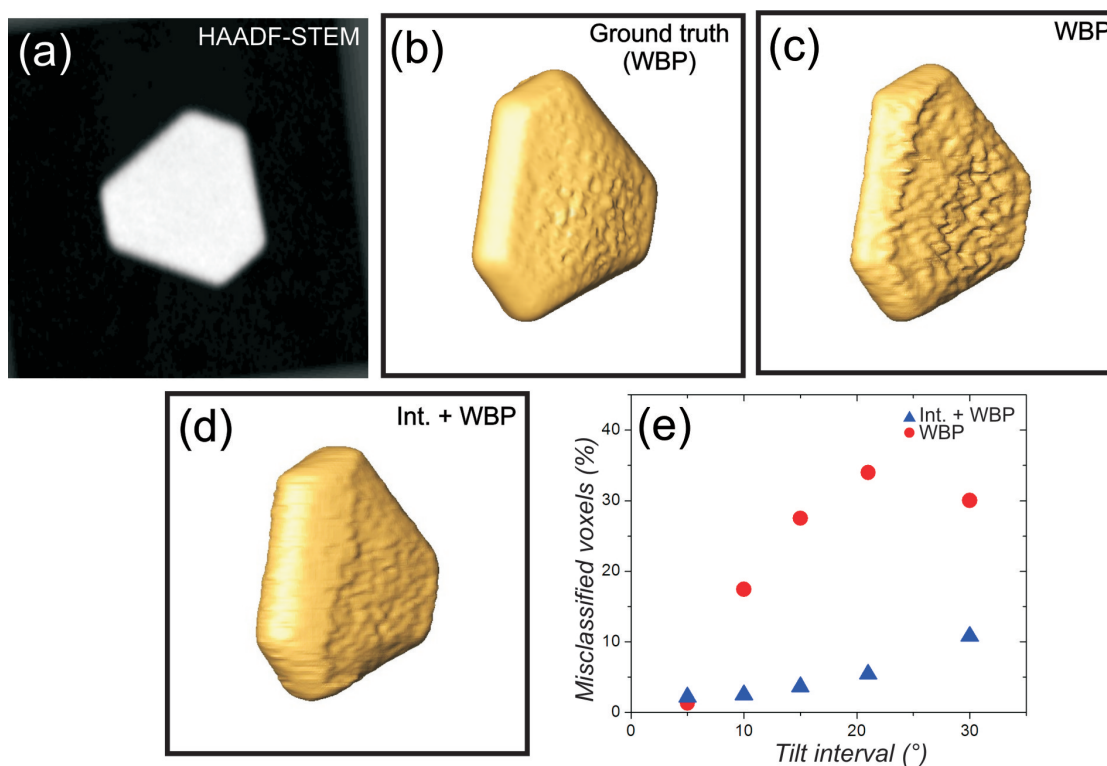


Figure 7.6: (a) HAADF-STEM image from a Au nanotriangle, (b) the reconstruction using full tilt series with a projection every 1°, (c) the reconstruction using sparse tilt series with a projection every 30°, (d) the visualization from the 3D reconstruction of an interpolated tilt series obtained from the tilt series with a projection every 30°, (e) comparison of misclassified voxels between interpolated tilt series and sparse tilt series for different tilt interval.

same interpolated dataset (Figure 7.6 d). To evaluate the reconstructions quantitatively, the number of misclassified voxels was calculated for reconstructions with different tilt interval (Figure 7.7 d). The error equals 10% for a reconstruction based on a series with tilt increment of  $15^\circ$  and increases up to 18% in case of a tilt increment of  $30^\circ$ . However, the percentage of misclassified voxels for the reconstructions using the interpolated tilt series never exceeds 6%. The misclassified voxels in the reconstruction based on only 6 projections are presented in Figure 7.7 e whereas Figure 7.7 f shows the misclassified voxels for the reconstruction using the interpolated tilt series. For both reconstructions, a slight overestimation of the volume is observed, albeit limited for Figure 7.7 f.

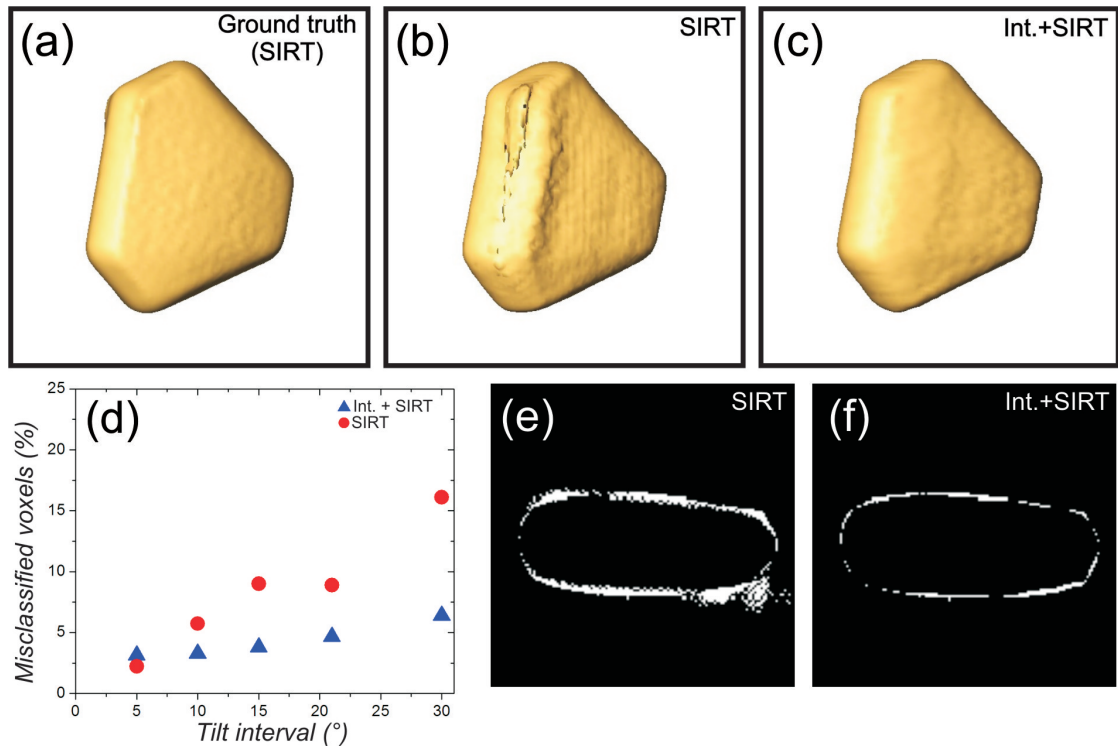


Figure 7.7: (a) The visualization from the 3D reconstruction using full tilt series, (b) using sparse tilt series with a projection every  $30^\circ$ , (c) and from the interpolated tilt series based on the sparse series, (d) the plot for the misclassified voxels as a function of increasing tilt interval. The misclassified voxels comparison between reconstruction from the sparse tilt series (e) and the interpolated tilt series (f).

### 7.3.2 NaYF<sub>4</sub> Hexagonal plates

To illustrate the potential of our approach for investigation of beam sensitive samples, NaYF<sub>4</sub> hexagonal platelets were studied. These nanoparticles can act as efficient luminescent hosts in applications such as biological diagnosis and solar cells [227, 228]. In order to optimize and tune their properties, a complete 3D characterization of their morphology is required. Figure 7.8 a shows a HAADF-STEM image of a NaYF<sub>4</sub> nanoparticle with a size of approximately 30 nm and a thickness of approximately 20 nm. First, a conventional HAADF-STEM tomography experiment was envisioned and a tilt series was acquired from  $-72^\circ$  to  $72^\circ$  with  $2^\circ$  intervals and an acceleration voltage of 200 kV. However, when comparing a HAADF-STEM projection acquired at the same tilt angle before (Figure 7.8 a) and after acquisition of the entire tilt series (Figure 7.8 b), sample degradation due to the electron beam is observed. The beam damage mainly induces holes in the 3D structure and the morphology also changes. Therefore, the tilt series cannot be used as an input for 3D reconstruction. Next, a tilt series of only 7 projection images was acquired from another nanoparticle ( $-74^\circ$  to  $70^\circ$  with a tilt increment of  $24^\circ$ ) and used as an input for sinogram interpolation. The interpolated tilt series was reconstructed using a WBP and a SIRT reconstruction algorithm. An isosurface rendering of the 3D reconstruction is presented in the Figure 7.8 c and d, clearly showing the hexagonal shape of the nanoparticle.

## 7.4 Discussion

Although the proposed sinogram interpolation method does not explicitly incorporate prior knowledge about the object, the method incorporates such prior knowledge in an implicit way, through the assumptions that are used for the interpolation procedure. The first key assumption is that image pixels for which the corresponding sine wave falls below the minimal threshold for some data points in the measured sinogram, do not belong to the object. This assumption may be violated when imaging thin structures, which have only a small contribution to the sinogram intensity. A second key assumption used in our approach is to

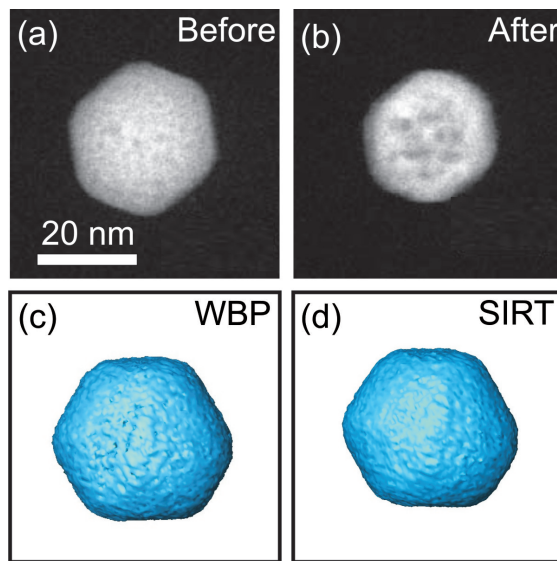


Figure 7.8: (a) HAADF-STEM image from a  $\text{NaYF}_4$  before the electron tomography experiment and (b) after the electron tomography experiment, (c) the visualization of the reconstruction using only 7 projections in combination with sinogram interpolation, (d) the visualization of the reconstruction using SIRT algorithm in combination with sinogram interpolation.

consider the sinogram as smooth and continuous, such that interpolation of the measured data points provides a suitable estimate of the intermediate points. This assumption is valid for structures that vary slowly from one projection to the next (i.e. have limited angular dependence), while structures for which the projections varies wildly from one angle to the next will be less suitable. Finally, we consider here particle structures that can be observed in isolation from possible other, surrounding particles. This property is important to enable effective selection of the sinogram waves that contribute to the particle under investigation.

In general, we can say that for individual convex particles with a diameter that is substantially larger than the pixel size, all key assumptions will often be well satisfied. As evidenced by our experimental results, the proposed method can lead to a strong improvement in image quality for such particles.

## **7.5 Conclusions**

In this study, we propose an approach to increase the reconstruction quality of sparse sampled tilt series by means of sinogram interpolation. The applicability of the method was demonstrated using a tilt series of a Au nanotriangle. Conventional reconstructions based on tilt series with different sparsity were compared with reconstructions after the interpolation procedure. Both a qualitative and a quantitative comparison show that the method we propose here results in a significant improvement of the reconstruction. The interpolation method was furthermore applied to a  $\text{NaYF}_4$  nanoparticle where electron beam damage prevents the acquisition of a tilt series with a relatively small tilt increment. A tilt series of only 7 projection images was acquired and used as an input for the proposed interpolation method and a SIRT reconstruction. In this manner, we could determine the morphology of the sample. We conclude that our methodology is of great interest to reconstruct individual convex particles with a diameter that is substantially larger than the pixel size of the projection images.



# Chapter 8

## Conclusions and Outlook

## 8.1 Conclusions and Outlook

In this thesis, I demonstrated the importance of electron tomography when investigating nanomaterials. My focus was on the 3D characterization of plasmonic nanoparticles, porous materials and the combination of both classes. Conventional electron tomography was applied to investigate the 3D structure of Au nanoparticles with applications in the field in biomedical applications (chapter 2). The outcome of these experiments enabled us to investigate the connection between the 3D structure and the properties of these nanostructures. In chapter 3, I investigated CuTe nanoparticles. These materials again have interesting optical properties, but so far the influence of vacancies was not yet understood. One of the main reasons is that information on the positions of the Cu vacancies is lacking. We therefore proposed a stepwise approach to visualize vacancies in CuTe nanoparticles. This is very challenging since in some areas of the particles, a superstructure was found. Since this was a very local effect, we could only reveal the presence by high resolution electron tomography. By combining the outcome of our experiments with DFT calculations, we could demonstrate that there is indeed an influence of the vacancies on the optical properties. The exact mechanisms however are not yet fully understood and I envisage that further investigations in this field are required. Very often it is necessary to extract quantitative information from 3D reconstructions. This is for example the case in chapter 4, where porous Pt dendrites were investigated. There is a clear need to determine porosity in a reliable manner at a local scale in 3D. This is not straightforward and one of the challenges is to separate chemically active pores from inactive pores (cavities). By tackling this problem, we were able to provide quantitative measurements that could be linked to the synthesis parameters. In this manner, the synthesis can be performed in an optimized manner. However, more progress is still required. For example, using conventional electron tomography it is far from straightforward to obtain 3D information that can be considered as an averaged or statistically relevant result. This is a major drawback when trying to connect the properties of the nanoparticles to their 3D structure. Fast electron tomography techniques will therefore

be of importance in the future. One of the main challenges in this thesis was the investigation of hybrid systems consisting of a Au nanoparticles encapsulated by a porous compound. 3D reconstructions of these systems show clear artifacts that hamper a quantitative investigation of the shell and the hybrid core-shell interface. I therefore proposed an innovative approach that exploits the flexibility of modern TEM instruments. By using different ADF detectors simultaneously, I was able to optimize the acquisition conditions. Moreover, I proposed a novel approach for the reconstruction based on inpainting technique. It is only by these developments that we were able to investigate Au encapsulated by SiO<sub>2</sub>, and were able to quantify the pore diameter. We also investigated the effect of the surfactant during the growth of ZIF-8 on Au@Ag plasmonic nanoparticles. All of these studies are of clear importance since these materials have important applications in the field of catalysis, gas sensing and storage. Being able to investigate the structure in 3D is required to further incorporate these materials in nanotechnology. I envisage that the approach that I proposed can be further optimized by the use of pixelated detectors. Since every pixel can be read out separately, this will enable us to select specific angular ranges without any restrictions after the acquisition. In the final chapter, I developed a new reconstruction approach that is applicable to beam sensitive materials. The technique is based on sinogram interpolation and is currently applicable to convex particles. However, I feel that the technique can also be adapted to investigate non convex systems by applying eigenvector-guided interpolation.

In conclusion, I have demonstrated the great use of electron tomography in the investigation of nanomaterials. Moreover, I have developed several new approaches to improve different aspects of the technique: I developed a new approach for high resolution tomography and I contributed to quantitative electron tomography enabling porosity measurements. To investigate hybrid systems, I optimized both the acquisition and the reconstruction. Finally, I proposed a new approach to investigate sensitive materials in 3D.

---

## Bibliography

- [1] Masatake Haruta. *Cattech*, 6(3):102–115, 2002.
- [2] Helmut Goesmann and Claus Feldmann. *Angewandte Chemie International Edition*, 49(8):1362–1395, 2010.
- [3] Xiaohua Huang, Ivan H El-Sayed, Wei Qian, and Mostafa A El-Sayed. *Journal of the American Chemical Society*, 128(6):2115–2120, 2006.
- [4] Joseph Della Rocca, Demin Liu, and Wenbin Lin. *Accounts of chemical research*, 44(10):957–968, 2011.
- [5] Juan L Vivero-Escoto, Rachel C Huxford-Phillips, and Wenbin Lin. *Chemical Society Reviews*, 41(7):2673–2685, 2012.
- [6] William J Rieter, Kathryn ML Taylor, Hongyu An, Weili Lin, and Wenbin Lin. *Journal of the American Chemical Society*, 128(28):9024–9025, 2006.
- [7] Marta N Sanz-Ortiz, Kadir Sentosun, Sara Bals, and Luis M Liz-Marzán. *ACS nano*, 9(10):10489–10497, 2015.
- [8] Guangchao Zheng, Zhuwen Chen, Kadir Sentosun, Ignacio Pérez-Juste, Sara Bals, Luis M Liz-Marzán, Isabel Pastoriza-Santos, Jorge Pérez-Juste, and Mei Hong. *Nanoscale*, 2017.
- [9] Ji Liu, Christophe Detrembleur, De Pauw-Gillet, Stéphane Mornet, Christine Jérôme, Etienne Duguet, et al. *Small*, 11(19):2323–2332, 2015.
- [10] David B Williams, C Barry Carter, and P Veyssiere. *Transmission electron microscopy: a textbook for materials science*, volume 10. Springer, 1998.
- [11] P Hartel, H Rose, and C Dinges. *Ultramicroscopy*, 63(2):93–114, 1996.
- [12] Rik Brydson. *Aberration-corrected analytical transmission electron microscopy*, volume 3. John Wiley & Sons, 2011.

- 
- [13] P Schlossmacher, DO Klenov, B Freitag, and HS Von Harrach. *Microscopy today*, 18(4):14–20, 2010.
- [14] Ray F Egerton. *Electron energy-loss spectroscopy in the electron microscope*. Springer Science & Business Media, 2011.
- [15] Olivia Nicoletti, Francisco de La Peña, Rowan K Leary, Daniel J Holland, Caterina Ducati, and Paul A Midgley. *Nature*, 502(7469):80, 2013.
- [16] Bart Goris, Stuart Turner, Sara Bals, and Gustaaf Van Tendeloo. *ACS nano*, 8(10):10878–10884, 2014.
- [17] DJ De Rosier and A Klug. *Nature*, 217(5124):130–134, 1968.
- [18] W Hoppe, R Langer, G Knesch, and Ch Poppe. *Naturwissenschaften*, 55(7):333–336, 1968.
- [19] Abraham J Koster, Rudo Grimm, Dieter Typke, Reiner Hegerl, Arne Stoschek, Jochen Walz, and Wolfgang Baumeister. *Journal of structural biology*, 120(3):276–308, 1997.
- [20] PA Midgley and Matthew Weyland. *Ultramicroscopy*, 96(3):413–431, 2003.
- [21] RHM Schoenmakers, RA Perquin, TF Fliervoet, W Voorhout, and H Schirmacher. *Microscopy and Analysis*, 19(4):5–6, 2005.
- [22] James R Kremer, David N Mastrorarde, and J Richard McIntosh. *Journal of structural biology*, 116(1):71–76, 1996.
- [23] Shawn Q Zheng, Bettina Keszthelyi, Eric Branlund, John M Lyle, Michael B Braunfeld, John W Sedat, and David A Agard. *Journal of structural biology*, 157(1):138–147, 2007.
- [24] Daniel Wolf, Axel Lubk, Hannes Lichte, and Heiner Friedrich. *Ultramicroscopy*, 110(5):390–399, 2010.
- [25] G Owen and DL Stokes, 2007.

- 
- [26] Ilke Arslan, Jenna R Tong, and Paul A Midgley. *Ultramicroscopy*, 106(11):994–1000, 2006.
- [27] Michael Radermacher. *Microscopy Research and Technique*, 9(4):359–394, 1988.
- [28] Xiaoxing Ke, Sara Bals, Daire Cott, Thomas Hantschel, Hugo Bender, and Gustaaf Van Tendeloo. *Microscopy and Microanalysis*, 16(2):210–217, 2010.
- [29] Noboru Kawase, Mitsuro Kato, Hideo Nishioka, and Hiroshi Jinnai. *Ultramicroscopy*, 107(1):8–15, 2007.
- [30] Peter Gilbert. *Journal of theoretical biology*, 36(1):105–117, 1972.
- [31] Kees Joost Batenburg and Jan Sijbers. *IEEE Transactions on Image Processing*, 20(9):2542–2553, 2011.
- [32] Daniele Zanaga, Folkert Bleichrodt, Thomas Altantzis, Naomi Winckelmans, Willem Jan Palenstijn, Jan Sijbers, Bart de Nijs, Marijn A van Huis, Ana Sánchez-Iglesias, Luis M Liz-Marzán, et al. *Nanoscale*, 8(1):292–299, 2016.
- [33] John Meurig Thomas, Rowan Leary, Paul A Midgley, and Daniel J Holland. *Journal of colloid and interface science*, 392:7–14, 2013.
- [34] Bart Goris, Wouter Van den Broek, K Joost Batenburg, H Heidari Mezerji, and Sara Bals. *Ultramicroscopy*, 113:120–130, 2012.
- [35] MC Scott, Chien-Chun Chen, Matthew Mecklenburg, Chun Zhu, Rui Xu, Peter Ercius, Ulrich Dahmen, BC Regan, and Jianwei Miao. *arXiv preprint arXiv:1108.5350*, 2011.
- [36] Bart Goris, Sara Bals, Wouter Van den Broek, Enrique Carbó-Argibay, Sergio Gómez-Graña, Luis M Liz-Marzán, and Gustaaf Van Tendeloo. *Nature materials*, 11(11):930–935, 2012.

- 
- [37] Thomas Altantzis, Bart Goris, Ana Sánchez-Iglesias, Marek Grzelczak, Luis M Liz-Marzán, and Sara Bals. *Particle & Particle Systems Characterization*, 30(1):84–88, 2013.
- [38] Stanley R Deans. *The Radon transform and some of its applications*. Courier Corporation, 2007.
- [39] RN Bracewell. *Australian Journal of Physics*, 9(3):297–314, 1956.
- [40] Avinash C Kak and Malcolm Slaney. *Principles of computerized tomographic imaging*. SIAM, 2001.
- [41] M Weyland and PA Midgley. *Nanocharacterisation*. The Royal Society of Chemistry, 2007.
- [42] PFC Gilbert. *Proceedings of the Royal Society of London B: Biological Sciences*, 182(1066):89–102, 1972.
- [43] Hamed Heidari Mezerji, Wouter Van den Broek, and Sara Bals. *Ultramicroscopy*, 111(5):330–336, 2011.
- [44] Rowan Leary, Zineb Saghi, Paul A Midgley, and Daniel J Holland. *Ultramicroscopy*, 131:70–91, 2013.
- [45] Matthew D Guay, Wojciech Czaja, Maria A Aronova, and Richard D Leapman. *Scientific reports*, 6, 2016.
- [46] Heinz Raether. *Springer tracts in modern physics*, volume 111. Springer-Verlag., 1988.
- [47] Prashant K Jain, Kyeong Seok Lee, Ivan H El-Sayed, and Mostafa A El-Sayed. *J. Phys. Chem. B*, 110(14):7238–7248, 2006.
- [48] Viktor Myroshnychenko, Jessica Rodríguez-Fernández, Isabel Pastoriza-Santos, Alison M Funston, Carolina Novo, Paul Mulvaney, Luis M Liz-Marzán, and F Javier Garcia de Abajo. *Chemical Society Reviews*, 37(9):1792–1805, 2008.

- 
- [49] Joseph A Webb and Rizia Bardhan. *Nanoscale*, 6(5):2502–2530, 2014.
- [50] Catherine J Murphy, Anand M Gole, John W Stone, Patrick N Sisco, Alaaldin M Alkilany, Edie C Goldsmith, and Sarah C Baxter. *Accounts of chemical research*, 41(12):1721–1730, 2008.
- [51] Marites P Melancon, Wei Lu, Zhi Yang, Rui Zhang, Zhi Cheng, Andrew M Elliot, Jason Stafford, Tammy Olson, Jin Z Zhang, and Chun Li. *Molecular cancer therapeutics*, 7(6):1730–1739, 2008.
- [52] Yin Zhang, Hao Hong, Duane V Myklejord, and Weibo Cai. *Small*, 7(23):3261–3269, 2011.
- [53] Kiang Wei Kho, Chit Yaw Fu, US Dinish, and Malini Olivo. *Journal of biophotonics*, 4(10):667–684, 2011.
- [54] Kyle C Bantz, Audrey F Meyer, Nathan J Wittenberg, Hyungsoon Im, Özge Kurtuluş, Si Hoon Lee, Nathan C Lindquist, Sang-Hyun Oh, and Christy L Haynes. *Physical Chemistry Chemical Physics*, 13(24):11551–11567, 2011.
- [55] Ramón Alvarez-Puebla, Luis M Liz-Marzán, and F Javier Garcia de Abajo. *The Journal of Physical Chemistry Letters*, 1(16):2428–2434, 2010.
- [56] Laura Rodriguez-Lorenzo, Ramón A Alvarez-Puebla, F Javier Garcia de Abajo, and Luis M Liz-Marzán. *The Journal of Physical Chemistry C*, 114(16):7336–7340, 2009.
- [57] Samuel L Kleinman, Renee R Frontiera, Anne-Isabelle Henry, Jon A Dieringer, and Richard P Van Duyne. *Physical Chemistry Chemical Physics*, 15(1):21–36, 2013.
- [58] Alberto Comin and Liberato Manna. *Chemical Society Reviews*, 43(11):3957–3975, 2014.
- [59] F Javier Garcia de Abajo. *Acs Photonics*, 1(3):135–152, 2014.

- 
- [60] Xin Liu and Mark T Swihart. *Chemical Society Reviews*, 43(11):3908–3920, 2014.
- [61] Mark W Knight, Nicholas S King, Lifei Liu, Henry O Everitt, Peter Nordlander, and Naomi J Halas. *ACS nano*, 8(1):834–840, 2013.
- [62] Isabel Pastoriza-Santos, Ana Sánchez-Iglesias, Benito Rodríguez-González, and Luis M Liz-Marzán. *Small*, 5(4):440–443, 2009.
- [63] Pandian Senthil Kumar, Isabel Pastoriza-Santos, Benito Rodriguez-Gonzalez, F Javier García de Abajo, and Luis M Liz-Marzan. *Nanotechnology*, 19(1):015606, 2007.
- [64] Wentong Lu, Anant Kumar Singh, Sadia Afrin Khan, Dulal Senapati, Hongtao Yu, and Paresh Chandra Ray. *Journal of the American Chemical Society*, 132(51):18103–18114, 2010.
- [65] Marek Grzelczak, Jorge Pérez-Juste, Paul Mulvaney, and Luis M Liz-Marzán. *Chemical Society Reviews*, 37(9):1783–1791, 2008.
- [66] Michelle L Personick, Mark R Langille, Jian Zhang, Nadine Harris, George C Schatz, and Chad A Mirkin. *Journal of the American Chemical Society*, 133(16):6170–6173, 2011.
- [67] Jian Zhang, Mark R Langille, Michelle L Personick, Ke Zhang, Shuyou Li, and Chad A Mirkin. *Journal of the American Chemical Society*, 132(40):14012–14014, 2010.
- [68] Yanyun Ma, Qin Kuang, Zhiyuan Jiang, Zhaoxiong Xie, Rongbin Huang, and Lansun Zheng. *Angewandte Chemie International Edition*, 47(46):8901–8904, 2008.
- [69] Hsin-Lun Wu, Chiu-Hua Chen, and Michael H Huang. *Chemistry of Materials*, 21(1):110–114, 2008.
- [70] Yue Yu, Qingbo Zhang, Xianmao Lu, and Jim Yang Lee. *The Journal of Physical Chemistry C*, 114(25):11119–11126, 2010.

- 
- [71] Amane Shiohara, Yusong Wang, and Luis M Liz-Marzan. *Journal of Photochemistry and Photobiology C: Photochemistry Reviews*, 21:2–25, 2014.
- [72] Calin Hrelescu, Tapan K Sau, Andrey L Rogach, Frank Jäckel, and Jochen Feldmann. *Applied Physics Letters*, 94(15):153113, 2009.
- [73] Stefano Mazzucco, Odile Stéphan, Christian Colliex, Isabel Pastoriza-Santos, Luis M Liz-Marzan, J Garcia de Abajo, and M Kociak. *The European Physical Journal-Applied Physics*, 54(3), 2011.
- [74] Feng Hao, Colleen L Nehl, Jason H Hafner, and Peter Nordlander. *Nano letters*, 7(3):729–732, 2007.
- [75] Jianping Xie, Jim Yang Lee, and Daniel IC Wang. *Chemistry of materials*, 19(11):2823–2830, 2007.
- [76] Max Schütz, Dennis Steinigeweg, Mohammad Salehi, Karsten Kömpe, and Sebastian Schlücker. *Chemical Communications*, 47(14):4216–4218, 2011.
- [77] Hsiangkuo Yuan, Christopher G Khoury, Hanjun Hwang, Christy M Wilson, Gerald A Grant, and Tuan Vo-Dinh. *Nanotechnology*, 23(7):075102, 2012.
- [78] Silvia Barbosa, Amit Agrawal, Laura Rodriguez-Lorenzo, Isabel Pastoriza-Santos, Ramón A Alvarez-Puebla, Andreas Kornowski, Horst Weller, and Luis M Liz-Marzán. *Langmuir*, 26(18):14943–14950, 2010.
- [79] Laura Rodríguez-Lorenzo, Ramón A Álvarez-Puebla, Isabel Pastoriza-Santos, Stefano Mazzucco, Odile Stéphan, Mathieu Kociak, Luis M Liz-Marzán, and F Javier García de Abajo. *Journal of the American Chemical Society*, 131(13):4616–4618, 2009.
- [80] Tuan Vo-Dinh, Andrew M Fales, Guy D Griffin, Christopher G Khoury, Yang Liu, Hoan Ngo, Stephen J Norton, Janna K Register, Hsin-Neng Wang, and Hsiangkuo Yuan. *Nanoscale*, 5(21):10127–10140, 2013.

- 
- [81] Laura Rodríguez-Lorenzo, José M Romo-Herrera, Jorge Perez-Juste, Ramón A Alvarez-Puebla, and Luis M Liz-Marzán. *Journal of Materials Chemistry*, 21(31):11544–11549, 2011.
- [82] Jie Zeng, Stefan Roberts, and Younan Xia. *Chemistry-A European Journal*, 16(42):12559–12563, 2010.
- [83] Yusong Wang, Lakshminarayana Polavarapu, and Luis M Liz-Marzan. *ACS applied materials & interfaces*, 6(24):21798–21805, 2014.
- [84] Ramon A Alvarez-Puebla and Luis M Liz-Marzan. *Chemical Society Reviews*, 41(1):43–51, 2012.
- [85] Andrew M Fales, Hsiangkuo Yuan, and Tuan Vo-Dinh. *The Journal of Physical Chemistry C*, 118(7):3708–3715, 2014.
- [86] Hsiangkuo Yuan, Yang Liu, Andrew M Fales, You Leo Li, Jesse Liu, and Tuan Vo-Dinh. *Analytical chemistry*, 85(1):208–212, 2012.
- [87] Laura Rodríguez-Lorenzo, Zeljka Krpetic, Silvia Barbosa, Ramón A Alvarez-Puebla, Luis M Liz-Marzán, Ian A Prior, and Mathias Brust. *Integrative Biology*, 3(9):922–926, 2011.
- [88] Andrew M Fales, Hsiangkuo Yuan, and Tuan Vo-Dinh. *Langmuir*, 27(19):12186–12190, 2011.
- [89] Naveen Gandra and Srikanth Singamaneni. *Advanced Materials*, 25(7):1022–1027, 2013.
- [90] Jibin Song, Bo Duan, Chenxu Wang, Jiajing Zhou, Lu Pu, Zheng Fang, Peng Wang, Teik Thye Lim, and Hongwei Duan. *Journal of the American Chemical Society*, 136(19):6838–6841, 2014.
- [91] Yusong Wang, Ana Belén Serrano, Kadir Sentosun, Sara Bals, and Luis M Liz-Marzán. Stabilization and encapsulation of gold nanostars mediated by dithiols. *small*, 11(34):4314–4320, 2015.

- 
- [92] Willem Jan Palenstijn, KJ Batenburg, and Jan Sijbers. *Journal of structural biology*, 176(2):250–253, 2011.
- [93] Dong-Kwon Lim, Ki-Seok Jeon, Jae-Ho Hwang, Hyoki Kim, Sunghoon Kwon, Yung Doug Suh, and Jwa-Min Nam. *Nature nanotechnology*, 6(7):452–460, 2011.
- [94] Jeong-Wook Oh, Dong-Kwon Lim, Gyeong-Hwan Kim, Yung Doug Suh, and Jwa-Min Nam. *Journal of the American Chemical Society*, 136(40):14052–14059, 2014.
- [95] Bin Zhao, Jianlei Shen, Shixing Chen, Dongfang Wang, Fan Li, Sanjay Mathur, Shiping Song, and Chunhai Fan. *Chemical Science*, 5(11):4460–4466, 2014.
- [96] Yuhua Feng, Jiating He, Hong Wang, Yee Yan Tay, Hang Sun, Liangfang Zhu, and Hongyu Chen. *Journal of the American Chemical Society*, 134(4):2004–2007, 2012.
- [97] Li Lin, Hongchen Gu, and Jian Ye. *Chemical Communications*, 51(100):17740–17743, 2015.
- [98] Ramón A Alvarez-Puebla, Eugene R Zubarev, Nicholas A Kotov, and Luis M Liz-Marzán. *Nano Today*, 7(1):6–9, 2012.
- [99] Ramón A Alvarez-Puebla, Ashish Agarwal, Prमित Manna, Bishnu P Khanal, Paula Aldeanueva-Potel, Enrique Carbó-Argibay, Nicolas Pazos-Pérez, Leonid Vigderman, Eugene R Zubarev, Nicholas A Kotov, et al. *Proceedings of the National Academy of Sciences*, 108(20):8157–8161, 2011.
- [100] Kyoungweon Park, Lawrence F Drummy, Robert C Wadams, Hilmar Kerner, Dhriti Nepal, Laura Fabris, and Richard A Vaia. *Chemistry of Materials*, 25(4):555–563, 2013.
- [101] Zhenmeng Peng and Hong Yang. *Nano Today*, 4(2):143–164, 2009.

- 
- [102] Luigi Carbone and P Davide Cozzoli. *Nano Today*, 5(5):449–493, 2010.
- [103] Wenhua Li, Reza Zamani, Pilar Rivera Gil, Beatriz Pelaz, Maria Ibanez, Doris Cadavid, Alexey Shavel, Ramon A Alvarez-Puebla, Wolfgang J Parak, Jordi Arbiol, et al. *Journal of the American Chemical Society*, 135(19):7098–7101, 2013.
- [104] Ilka Kriegel, Chengyang Jiang, Jessica Rodríguez-Fernandez, Richard D Schaller, Dmitri V Talapin, Enrico Da Como, and Jochen Feldmann. *Journal of the American Chemical Society*, 134(3):1583–1590, 2012.
- [105] Joseph M Luther, Prashant K Jain, Trevor Ewers, and A Paul Alivisatos. *Nature materials*, 10(5):361–366, 2011.
- [106] Dirk Dorfs, Thomas Hartling, Karol Miszta, Nadja C Bigall, Mee Rahn Kim, Alessandro Genovese, Andrea Falqui, Mauro Povia, and Liberato Manna. *Journal of the American Chemical Society*, 133(29):11175–11180, 2011.
- [107] Ilka Kriegel, Jessica Rodriguez-Fernandez, Andreas Wisnet, Hui Zhang, Christian Waurisch, Alexander Eychmuller, Aliaksei Dubavik, Alexander O Govorov, and Jochen Feldmann. *ACS nano*, 7(5):4367–4377, 2013.
- [108] X Wu, J Zhou, A Duda, Y Yan, G Teeter, S Asher, WK Metzger, S Demtsu, Su-Huai Wei, and R Noufi. *Thin Solid Films*, 515(15):5798–5803, 2007.
- [109] Hongbo Li, Rosaria Brescia, Mauro Povia, Mirko Prato, Giovanni Bertoni, Liberato Manna, and Iwan Moreels. *Journal of the American Chemical Society*, 135(33):12270–12278, 2013.
- [110] Guanjun Xiao, Yi Zeng, Yueyue Jiang, Jiajia Ning, Weitao Zheng, Bingbing Liu, Xiaodong Chen, Guangtian Zou, and Bo Zou. *Small*, 9(5):793–799, 2013.
- [111] Christian Baerlocher, Thomas Weber, Lynne B McCusker, Lukas Palatinus, and Stacey I Zones. *Science*, 333(6046):1134–1137, 2011.

- 
- [112] Tom Willhammar, Junliang Sun, Wei Wan, Peter Oleynikov, Daliang Zhang, Xiaodong Zou, Manuel Moliner, Jorge Gonzalez, Cristina Martínez, Fernando Rey, et al. *Nature chemistry*, 4(3):188–194, 2012.
- [113] Daliang Zhang, Peter Oleynikov, Sven Hovmöller, and Xiaodong Zou. *Zeitschrift für Kristallographie International journal for structural, physical, and chemical aspects of crystalline materials*, 225(2-3):94–102, 2010.
- [114] U Kolb, T Gorelik, C Kübel, MT Otten, and D Hubert. *Ultramicroscopy*, 107(6):507–513, 2007.
- [115] Tom Willhammar, Yifeng Yun, and Xiaodong Zou. *Advanced Functional Materials*, 24(2):182–199, 2014.
- [116] Mark Feyand, Enrico Mugnaioli, Frederik Vermoortele, Bart Bueken, Johannes M Dieterich, Tim Reimer, Ute Kolb, Dirk De Vos, and Norbert Stock. *Angewandte Chemie International Edition*, 51(41):10373–10376, 2012.
- [117] Bart Goris, Jan De Beenhouwer, Annick De Backer, Daniele Zanaga, K Joost Batenburg, Ana Sánchez-Iglesias, Luis M Liz-Marzán, Sandra Van Aert, Sara Bals, Jan Sijbers, et al. *Nano letters*, 15(10):6996–7001, 2015.
- [118] Renyong Tu, Yi Xie, Giovanni Bertoni, Aidin Lak, Roberto Gaspari, Arnaldo Rapallo, Andrea Cavalli, Luca De Trizio, and Liberato Manna. *J. Am. Chem. Soc.*, 138(22):7082–7090, 2016.
- [119] Gaixia Zhang, Shuhui Sun, Mei Cai, Yong Zhang, Ruying Li, and Xueliang Sun. *Scientific reports*, 3, 2013.
- [120] Timothy E Lipman, Jennifer L Edwards, and Daniel M Kammen. *Energy Policy*, 32(1):101–125, 2004.
- [121] Joshua Snyder, Ian McCue, Ken Livi, and Jonah Erlebacher. *Journal of the American Chemical Society*, 134(20):8633–8645, 2012.
- [122] Na Tian, Zhi-You Zhou, Shi-Gang Sun, Yong Ding, and Zhong Lin Wang. *science*, 316(5825):732–735, 2007.

- 
- [123] Lan Yun Chang, Amanda S Barnard, Lionel Cervera Gontard, and Rafal E Dunin-Borkowski. *Nano letters*, 10(8):3073–3076, 2010.
- [124] Hao Ming Chen, Ru-Shi Liu, Man-Yin Lo, Sung-Chun Chang, Li-Duan Tsai, Yu-Min Peng, and Jyh-Fu Lee. *The Journal of Physical Chemistry C*, 112(20):7522–7526, 2008.
- [125] M Manikandan, Nazim Hasan, and Hui-Fen Wu. *Biomaterials*, 34(23):5833–5842, 2013.
- [126] Byungkwon Lim, Majiong Jiang, Pedro HC Camargo, Eun Chul Cho, Jing Tao, Xianmao Lu, Yimei Zhu, and Younan Xia. *science*, 324(5932):1302–1305, 2009.
- [127] Shaofang Fu, Chengzhou Zhu, Qiurong Shi, Haibing Xia, Dan Du, and Yuehe Lin. *Nanoscale*, 8(9):5076–5081, 2016.
- [128] Ashok Mohanty, Niti Garg, and Rongchao Jin. *Angewandte Chemie International Edition*, 49(29):4962–4966, 2010.
- [129] Jianguang Xu, Adria R Wilson, Aaron R Rathmell, Jane Howe, Miaofang Chi, and Benjamin J Wiley. *ACS nano*, 5(8):6119–6127, 2011.
- [130] Jon Ustarroz, Bart Geboes, Hans Vanrompay, Kadir Sentosun, Sara Bals, Tom Breugelmans, and Annick Hubin. *ACS Applied Materials & Interfaces*, 9(19):16168–16177, 2017.
- [131] Bart Geboes, Jon Ustarroz, Kadir Sentosun, Hans Vanrompay, Annick Hubin, Sara Bals, and Tom Breugelmans. *ACS Catalysis*, 6(9):5856–5864, 2016.
- [132] Yuyan Shao, Geping Yin, and Yunzhi Gao. *Journal of Power Sources*, 171(2):558–566, 2007.
- [133] S Srinivasan. *LLC, New York*, page 208, 2006.
- [134] Stephen Brunauer, Paul Hugh Emmett, and Edward Teller. *Journal of the American chemical society*, 60(2):309–319, 1938.

- 
- [135] Wolf Vielstich, Arnold Lamm, Harumi Yokokawa, and Hubert Andreas Gasteiger. *Handbook of fuel cells: fundamentals technology and applications*, volume 2. John Wiley & Sons, 2009.
- [136] Bart Vanrenterghem, Bart Geboes, Sara Bals, Jon Ustarroz, Annick Hubin, and Tom Breugelmans. *Applied Catalysis B: Environmental*, 181:542–549, 2016.
- [137] Tine Brülle, Wenbo Ju, Philipp Niedermayr, Andrej Denisenko, Odysseas Paschos, Oliver Schneider, and Ulrich Stimming. *Molecules*, 16(12):10059–10077, 2011.
- [138] Kwok H Ng, H Liu, and RM Penner. *Langmuir*, 16(8):4016–4023, 2000.
- [139] H. Vanrompay. Quantitative structural characterization of porous nanomaterials by advanced electron tomography. Master’s thesis, University of Antwerp, Antwerp, 2016.
- [140] Donald Smith. *Thin-film deposition: principles and practice*. McGraw Hill Professional, 1995.
- [141] Jon Ustarroz, Joshua A Hammons, Thomas Altantzis, Annick Hubin, Sara Bals, and Herman Terryn. *Journal of the American Chemical Society*, 135(31):11550–11561, 2013.
- [142] Mitch Jacoby. *Chem. Eng. News*, 86(34):13–16, 2008.
- [143] Zhenjiang Zhang, Liming Wang, Jing Wang, Xiumei Jiang, Xiaohui Li, Zhijian Hu, Yinglu Ji, Xiaochun Wu, and Chunying Chen. *Advanced Materials*, 24(11):1418–1423, 2012.
- [144] CT Kresge, ME Leonowicz, WJ Roth, JC Vartuli, JS Beck, et al. *nature*, 359(6397):710–712, 1992.
- [145] Paul A Midgley and Rafal E Dunin-Borkowski. *Nature materials*, 8(4):271, 2009.

- 
- [146] AJ Koster, Ulrike Ziese, AJ Verkleij, AH Janssen, and KP De Jong. *The Journal of Physical Chemistry B*, 104(40):9368–9370, 2000.
- [147] Sara Bals, Gustaaf Van Tendeloo, and Christian Kisielowski. *Advanced Materials*, 18(7):892–895, 2006.
- [148] B Goris, S Bals, W Van den Broek, J Verbeeck, and G Van Tendeloo. *Ultramicroscopy*, 111(8):1262–1267, 2011.
- [149] H Friedrich, MR McCartney, and PR Buseck. *Ultramicroscopy*, 106(1):18–27, 2005.
- [150] Meng CAO, H-B ZHANG, Yong LU, R Nishi, and A Takaoka. *Journal of microscopy*, 239(1):66–71, 2010.
- [151] F Edward Boas and Dominik Fleischmann. *Imaging Med*, 4(2):229–240, 2012.
- [152] SJ Pennycook. *Annual review of materials science*, 22(1):171–195, 1992.
- [153] Kees Joost Batenburg, Sara Bals, J Sijbers, C Kübel, PA Midgley, JC Hernandez, U Kaiser, ER Encina, EA Coronado, and G Van Tendeloo. *Ultramicroscopy*, 109(6):730–740, 2009.
- [154] Enrique Carbó-Argibay, Benito Rodríguez-González, Isabel Pastoriza-Santos, Jorge Pérez-Juste, and Luis M Liz-Marzán. *Nanoscale*, 2(11):2377–2383, 2010.
- [155] Luis M Liz-Marzán, Michael Giersig, and Paul Mulvaney. *Langmuir*, 12(18):4329–4335, 1996.
- [156] Paula C Angelomé, Isabel Pastoriza-Santos, Jorge Pérez-Juste, Benito Rodríguez-González, Andrés Zelcer, Galo JAA Soler-Illia, and Luis M Liz-Marzán. *Nanoscale*, 4(3):931–939, 2012.
- [157] Paula C Angelomé and Luis M Liz-Marzán. *Journal of sol-gel science and technology*, 70(2):180–190, 2014.

- 
- [158] Jorge Pérez-Juste, Luis M Liz-Marzán, Steven Carnie, Derek YC Chan, and Paul Mulvaney. *Advanced Functional Materials*, 14(6):571–579, 2004.
- [159] Wim van Aarle, Willem Jan Palenstijn, Jan De Beenhouwer, Thomas Alantzi, Sara Bals, K Joost Batenburg, and Jan Sijbers. *Ultramicroscopy*, 157:35–47, 2015.
- [160] Kahye Song, Luis R Comolli, and Mark Horowitz. *Journal of structural biology*, 178(2):108–120, 2012.
- [161] Yang Chen, Yinsheng Li, Hong Guo, Yining Hu, Limin Luo, Xindao Yin, Jianping Gu, and Christine Toumoulin. *Mathematical Problems in Engineering*, 2012, 2012.
- [162] Jianwei Gu, Li Zhang, Guoqiang Yu, Yuxiang Xing, and Zhiqiang Chen. *Journal of X-ray Science and Technology*, 14(2):73–82, 2006.
- [163] Damien Garcia. *Computational statistics & data analysis*, 54(4):1167–1178, 2010.
- [164] Guojie Wang, Damien Garcia, Yi Liu, Richard De Jeu, and A Johannes Dolman. *Environmental Modelling & Software*, 30:139–142, 2012.
- [165] Kojirou Fuku, Ryunosuke Hayashi, Shuhei Takakura, Takashi Kamegawa, Kohsuke Mori, and Hiromi Yamashita. *Angewandte Chemie International Edition*, 52(29):7446–7450, 2013.
- [166] P Pallavicini, G Chirico, M Collini, G Dacarro, A Donà, L D’alfonso, A Falqui, Y Diaz-Fernandez, S Freddi, B Garofalo, et al. *Chemical Communications*, 47(4):1315–1317, 2011.
- [167] David D Evanoff and George Chumanov. *ChemPhysChem*, 6(7):1221–1231, 2005.
- [168] K Lance Kelly, Eduardo Coronado, Lin Lin Zhao, and George C Schatz, 2003.

- 
- [169] Wiebke Albrecht, Jessi ES Van Der Hoeven, Tian-Song Deng, Petra E De Jongh, and Alfons Van Blaaderen. *Nanoscale*, 9(8):2845–2851, 2017.
- [170] Martin Mayer, Leonardo Scarabelli, Katia March, Thomas Altantzis, Moritz Tebbe, Mathieu Kociak, Sara Bals, F Javier García de Abajo, Andreas Fery, and Luis M Liz-Marzan. *Nano letters*, 15(8):5427, 2015.
- [171] Yong Yang, Jianlin Shi, Go Kawamura, and Masayuki Nogami. *Scripta Materialia*, 58(10):862–865, 2008.
- [172] Rafael Contreras-Caceres, Claudine Dawson, Petr Formanek, Dieter Fischer, Frank Simon, Andreas Janke, Petra Uhlmann, and Manfred Stamm. *Chemistry of Materials*, 25(2):158–169, 2013.
- [173] Dongyuan Zhao, Jianglin Feng, Qisheng Huo, Nicholas Melosh, Glenn H Fredrickson, Bradley F Chmelka, and Galen D Stucky. *science*, 279(5350):548–552, 1998.
- [174] Dongyuan Zhao, Qisheng Huo, Jianglin Feng, Bradley F Chmelka, and Galen D Stucky. *Journal of the American Chemical Society*, 120(24):6024–6036, 1998.
- [175] G Satishkumar, L Titelman, and MV Landau. *Journal of Solid State Chemistry*, 182(10):2822–2828, 2009.
- [176] Wenbo Yue and Wuzong Zhou. *Progress in Natural Science*, 18(11):1329–1338, 2008.
- [177] AL Doadrio, EMB Sousa, JC Doadrio, J Pérez Pariente, I Izquierdo-Barba, and M Vallet-Regí. *Journal of Controlled Release*, 97(1):125–132, 2004.
- [178] Hui Yu and Qing-Zhou Zhai. *Microporous and Mesoporous Materials*, 123(1):298–305, 2009.
- [179] Randy Mellaerts, Kristof Houthoofd, Ken Elen, Hong Chen, Michiel Van Speybroeck, Jan Van Humbeeck, Patrick Augustijns, Jules Mullens,

- 
- Guy Van den Mooter, and Johan A Martens. *Microporous and Mesoporous Materials*, 130(1):154–161, 2010.
- [180] SA Mirji, SB Halligudi, Nevin Mathew, Nalini E Jacob, KR Patil, and AB Gaikwad. *Materials Letters*, 61(1):88–92, 2007.
- [181] Masahiro Ohmori and Egon Matijević. *Journal of Colloid and Interface Science*, 160(2):288–292, 1993.
- [182] Luis M Liz-Marzán and Albert P Philipse. *Journal of colloid and interface science*, 176(2):459–466, 1995.
- [183] Timothy R Cook, Yao-Rong Zheng, and Peter J Stang. *Chemical reviews*, 113(1):734–777, 2012.
- [184] Stephen S-Y Chui, Samuel M-F Lo, Jonathan PH Charmant, A Guy Orpen, and Ian D Williams. *Science*, 283(5405):1148–1150, 1999.
- [185] Thierry Loiseau, Christian Serre, Clarisse Huguenard, Gerhard Fink, Francis Taulelle, Marc Henry, Thierry Bataille, and Gérard Férey. *Chemistry-A European Journal*, 10(6):1373–1382, 2004.
- [186] Sergio J Garibay and Seth M Cohen. *Chemical Communications*, 46(41):7700–7702, 2010.
- [187] Hai-Long Jiang, Bo Liu, Tomoki Akita, Masatake Haruta, Hiroaki Sakurai, and Qiang Xu. *Journal of the American Chemical Society*, 131(32):11302–11303, 2009.
- [188] Helge Bux, Christian Chmelik, Rajamani Krishna, and Juergen Caro. *Journal of membrane science*, 369(1):284–289, 2011.
- [189] Helge Bux, Fangyi Liang, Yanshuo Li, Janosch Cravillon, Michael Wiebcke, and Jurgen Caro. *Journal of the American Chemical Society*, 131(44):16000–16001, 2009.

- 
- [190] Surendar R Venna, Jacek B Jasinski, and Moises A Carreon. *Journal of the American Chemical Society*, 132(51):18030–18033, 2010.
- [191] Yichang Pan and Zhiping Lai. *Chemical Communications*, 47(37):10275–10277, 2011.
- [192] Rie Makiura, Soichiro Motoyama, Yasushi Umemura, Hiroaki Yamanaka, Osami Sakata, and Hiroshi Kitagawa. *Nature materials*, 9(7), 2010.
- [193] Kah Ee Fong and Lin-Yue Lanry Yung. *Nanoscale*, 5(24):12043–12071, 2013.
- [194] Kathryn M Mayer and Jason H Hafner. *Chemical reviews*, 111(6):3828–3857, 2011.
- [195] MA Garcia. *Journal of Physics D: Applied Physics*, 45(38):389501, 2012.
- [196] Sebastian Schlücker. *Angewandte Chemie International Edition*, 53(19):4756–4795, 2014.
- [197] Lakshminarayana Polavarapu, Jorge Pérez-Juste, Qing-Hua Xu, and Luis M Liz-Marzán. *Journal of Materials Chemistry C*, 2(36):7460–7476, 2014.
- [198] Leonardo Scarabelli, Marc Coronado-Puchau, Juan J Giner-Casares, Judith Langer, and Luis M Liz-Marzán. *ACS nano*, 8(6):5833–5842, 2014.
- [199] Weiyang Li, Pedro HC Camargo, Xianmao Lu, and Younan Xia. *Nano letters*, 9(1):485–490, 2008.
- [200] Cristina Fernández-López, Cintia Mateo-Mateo, Ramón A Alvarez-Puebla, Jorge Pérez-Juste, Isabel Pastoriza-Santos, and Luis M Liz-Marzán. Highly controlled silica coating of peg-capped metal nanoparticles and preparation of sers-encoded particles. *Langmuir*, 25(24):13894–13899, 2009.
- [201] Wenjing Liu, Zhening Zhu, Ke Deng, Zhengtao Li, Yunlong Zhou, Huibin Qiu, Yan Gao, Shunai Che, and Zhiyong Tang. *Journal of the American Chemical Society*, 135(26):9659–9664, 2013.

- 
- [202] Bart Goris, Annick De Backer, Sandra Van Aert, Sergio Gomez-Gran a, Luis M Liz-Marzan, Gustaaf Van Tendeloo, and Sara Bals. *Nano letters*, 13(9):4236–4241, 2013.
- [203] Kadir Sentosun, Marta N Sanz Ortiz, K Joost Batenburg, Luis M Liz-Marzán, and Sara Bals. *Particle & Particle Systems Characterization*, 32(12):1063–1067, 2015.
- [204] Mingzhao Liu and Philippe Guyot-Sionnest. *The Journal of Physical Chemistry B*, 108(19):5882–5888, 2004.
- [205] Sergey M Novikov, Ana Sánchez-Iglesias, Mikołaj K Schmidt, Andrey Chuvilin, Javier Aizpurua, Marek Grzelczak, and Luis M Liz-Marzán. *Particle & Particle Systems Characterization*, 31(1):77–80, 2014.
- [206] Rahul Dev Mukhopadhyay, Vakayil K Praveen, Arpan Hazra, Tapas Kumar Maji, and Ayyappanpillai Ajayaghosh. *Chemical Science*, 6(11):6583–6591, 2015.
- [207] Paolo Falcaro, Raffaele Ricco, Amirali Yazdi, Inhar Imaz, Shuhei Furukawa, Daniel MasPOCH, Rob Ameloot, Jack D Evans, and Christian J Doonan. *Coordination Chemistry Reviews*, 307:237–254, 2016.
- [208] Hae Sung Cho, Hexiang Deng, Keiichi Miyasaka, Zhiyue Dong, Minhyung Cho, Alexander V Neimark, Jeung Ku Kang, Omar M Yaghi, and Osamu Terasaki. *Nature*, 527(7579):503–507, 2015.
- [209] Jarad A Mason, Julia Oktawiec, Mercedes K Taylor, Matthew R Hudson, Julien Rodriguez, Jonathan E Bachman, Miguel I Gonzalez, Antonio Cervellino, Antonietta Guagliardi, Craig M Brown, et al. *Nature*, 527(7578):357–361, 2015.
- [210] Melinda Sindoro, Nobuhiro Yanai, Ah-Young Jee, and Steve Granick. *Accounts of chemical research*, 47(2):459–469, 2013.

- 
- [211] Christina V McGuire and Ross S Forgan. *Chemical communications*, 51(25):5199–5217, 2015.
- [212] Jianfeng Yao, Ming He, and Huanting Wang. *CrystEngComm*, 17(27):4970–4976, 2015.
- [213] Beatriz Seoane, Sonia Castellanos, Alla Dikhtiarenko, Freek Kapteijn, and Jorge Gascon. *Coordination Chemistry Reviews*, 307:147–187, 2016.
- [214] Takaaki Tsuruoka, Shuhei Furukawa, Yohei Takashima, Kaname Yoshida, Seiji Isoda, and Susumu Kitagawa. *Angewandte Chemie International Edition*, 48(26):4739–4743, 2009.
- [215] Ayako Umemura, Stéphane Diring, Shuhei Furukawa, Hiromitsu Uehara, Takaaki Tsuruoka, and Susumu Kitagawa. *Journal of the American Chemical Society*, 133(39):15506–15513, 2011.
- [216] Wei-Wei Xiong and Qichun Zhang. *Angewandte Chemie International Edition*, 54(40):11616–11623, 2015.
- [217] Yichang Pan, Dodi Heryadi, Feng Zhou, Lan Zhao, Gabriella Lestari, Haibin Su, and Zhiping Lai. *CrystEngComm*, 13(23):6937–6940, 2011.
- [218] James JP Stewart. Mopac2012. *Stewart Computational Chemistry, Colorado Springs, CO, USA*, 2012.
- [219] Ravishankar Chityala, Kenneth R Hoffmann, Stephen Rudin, and Daniel R Bednarek. In *Proceedings of SPIE—the International Society for Optical Engineering*, volume 5747, page 2110. NIH Public Access, 2005.
- [220] Yinsheng Li, Yang Chen, Yining Hu, Ahmed Oukili, Limin Luo, Wufan Chen, and Christine Toumoulin. *JOSA A*, 29(1):153–163, 2012.
- [221] EPA Constantino and Krikor B Ozanyan. *Measurement Science and Technology*, 19(9):094015, 2008.
- [222] Martti Kalke and Samuli Siltanen. *Applied Mathematics*, 5(03):423, 2014.

- [223] Catur Edi Widodo, Kus Kusminarto, and Gede Bayu Suparta. *Int J Eng Technol IJET-IJENS*, 11:86–89, 2011.
- [224] Toft Peter. *The radon transform-theory and implementation*. PhD thesis, PhD thesis, Dept. of Mathematical Modelling Section for Digital Signal Processing of Technical University of Denmark, 1996.
- [225] Sara Bals, Bart Goris, Thomas Altantzis, Hamed Heidari, Sandra Van Aert, and Gustaaf Van Tendeloo. *Comptes Rendus Physique*, 15(2):140–150, 2014.
- [226] Alexander D Poularikas. *Transforms and applications handbook*. CRC press, 2010.
- [227] Guofeng Wang, Qing Peng, and Yadong Li. *Accounts of chemical research*, 44(5):322–332, 2011.
- [228] Jing Zhou, Zhuang Liu, and Fuyou Li. *Chemical Society Reviews*, 41(3):1323–1349, 2012.

# List of scientific contributions

## Papers in A1 scientific journals

- Stabilization and encapsulation of gold nanostars mediated by dithiols, Yusong Wang, Ana Belen Serrano, **Kadir Sentosun**, Sara Bals, Luis M Liz-Marzan, *Small*, 11(34), 4314-4320, 2015
- Templated growth of surface enhanced raman scattering-active branched gold nanoparticles within radial mesoporous silica shells, Marta N Sanz-Ortiz, **Kadir Sentosun**, Sara Bals, Luis M Liz-Marzan, *ACS nano*, 9(10), 10489-10497, 2015
- Engineering structural diversity in gold nanocrystals by ligand-mediated interface control, Yusong Wang, **Kadir Sentosun**, Anran Li, Marc Coronado-Puchau, Ana Sanchez-Iglesias, Shuzhou Li, Xiaodi Su, Sara Bals, Luis M Liz-Marzan, *Chemistry of Materials*, 27(23), 8032-8040, 2015
- Combination of HAADF-STEM and ADF-STEM Tomography for Core-Shell Hybrid Materials, **Kadir Sentosun**, Marta N Sanz Ortiz, K Joost Batenburg, Luis M Liz-Marzan, Sara Bals, *Particle & Particle Systems Characterization*, 32(12), 1063-1067, 2015)
- Gold nanostar-coated polystyrene beads as multifunctional nanoprobe for SERS bioimaging, Ana B Serrano-Montes, Judith Langer, Malou Henriksen-Lacey, Dorleta Jimenez de Aberasturi, Diego M Solis, Jose M Taboada, Fernando Obelleiro, **Kadir Sentosun**, Sara Bals, Ahmet Bekdemir, Francesco Stellacci, Luis M Liz-Marzan, *The Journal of Physical Chemistry C*, 120(37), 20860-20868, 2016
- Encapsulation of Single Plasmonic Nanoparticles within ZIF-8 and SERS Analysis of the MOF Flexibility, Guangchao Zheng, Sarah de Marchi, Vanesa

Lopez-Puente, **Kadir Sentosun**, Lakshminarayana Polavarapu, Ignacio Prez-Juste, Eric H. Hill, Sara Bals, Luis M Liz-Marzan, Isabel Pastoriza-Santos, Jorge Prez-Juste, *Small*, 12(29), 3935-3943, 2016

- Electrochemical Behavior of Electrodeposited Nanoporous Pt Catalysts for the Oxygen Reduction Reaction, Bart Geboes, Jon Ustarroz, **Kadir Sentosun**, Hans Vanrompay, Annick Hubin, Sara Bals, Tom Breugelmans, *ACS Catalysis*, 6(9), 5856-5864, 2016
- Structure and vacancy distribution in copper telluride nanoparticles influence plasmonic activity in the near-infrared, Tom Willhammar, **Kadir Sentosun**, Stefanos Mourdikoudis, Bart Goris, Mert Kurttepli, Marnik Berx, Dirk Lamoen, Bart Partoens, Isabel Pastoriza-Santos, Jorge Prez-Juste, Luis M Liz-Marzan, Sara Bals, Gustaaf Van Tendeloo *Nature communications*, 8, 2017
- Comprehensive Study of the Electrodeposition of Nickel Nanostructures from Deep Eutectic Solvents: Self-Limiting Growth by Electrolysis of Residual Water, El Amine Mernissi Cherigui, **Kadir Sentosun**, Pieter Bouckenooge, Hans Vanrompay, Sara Bals, Herman Terryn, Jon Ustarroz, *The Journal of Physical Chemistry C*, 121(17), 9337-9347, 2017
- Electrodeposition of Highly Porous Pt Nanoparticles Studied by Quantitative 3D Electron Tomography: Influence of Growth Mechanisms and Potential Cycling on the Active Surface Area, Jon Ustarroz, Bart Geboes, Hans Vanrompay, **Kadir Sentosun**, Sara Bals, Tom Breugelmans, Annick Hubin, *ACS applied materials & interfaces*, 9(19), 16168-16177, 2017
- Shape control in ZIF-8 nanocrystals and metal nanoparticles@ ZIF-8 heterostructures, Guangchao Zheng, Zhuwen Chen, **Kadir Sentosun**, Ignacio Prez-Juste, Sara Bals, Luis M Liz-Marzan, Isabel Pastoriza-Santos, Jorge Prez-Juste, Mei Hong, *Nanoscale*, 9(43), 16645-16651, 2017
- Artifact reduction based on sinogram interpolation for the 3D reconstruction of nanoparticles using electron tomography, **Kadir Sentosun**, Ivan Lobato,

Eva Bladt, Yang Zhang, Willem Jan Palenstijn, Kees Joost Batenburg, Dirk Van Dyck, Sara Bals, *Particle & Particle Systems Characterization*, 34(12), 2017

# Acknowledgment

In this part, I would like to take a moment to thank some people who have contributed to the final result of this thesis. Foremost, I would like to express my utmost gratitude to my supervisor Prof. Dr. Sara Bals for giving me, first of all the opportunity and also the encouragement and support during the four years which I will always remember.

It is a great pleasure to thank everyone who helped me write my thesis successfully; many thanks to Dr. Bart Goris, Dr. Tom Willhammar and Marnik Bercx and Dr. Ivan Lobato, Dr. Willem Jan Palenstijn, Prof. Dr. K. Joost Batenburg and Prof. Dr. Dirk Van Dyck for their close collaborations, assistance and fruitful discussions. I would like to thank Prof. Dr. Luis M. Liz-Marzan, Dr. Yusong Wang, Dr. Marta N. Sanz Ortiz, Dr. Ana Belen Serrano Montes in CICbiomaGUNE, Prof. Dr. Herman Terryn, Dr. Jon Ustarroz, Dr. Bart Geboes, El Amine Mernissi Cherigui in University of Brussels for providing the samples. I would like to thank Dr. Karel van den Bos for translations. I would especially thank to Dr. Eva Bladt for helping me both with significant amount of corrections in my thesis and my presentations during the four years.

I would like to thank to Dr. Armand Beche, Dr. Stuart Turner, Dr. Thomas Altantzis, Dr. Mert Kurttepli, Dr. Hamed Heidari Mezerji and Dr. Rasit Burak Erkartal for the assistance with the microscopes and/or data analysis.

I am indebted to many of my colleagues and friends for providing the most stimulating and fun environment to learn and to enjoy. In particular, Eva Bladt, Thomas Altantzis, Daniele Zanaga, Martin Phannmoeller, Marnik Bercx, Andrea La Porta, Roeland Juchtmans, Giulio Guzzinati, and Mert Kurttepli, Burak Erkartal, Engin Torun, Deniz Cakir.

I am eternally grateful to my parents and my brothers, who were always support-

ive, with their unquestioning support throughout my life.

Last but not least, I want to thank my wife Bridget, for her unlimited support during this long journey of my PhD. The journey of a student during PhD is very much like a sine wave, full of ‘ups’ and ‘downs’, with your support I was able to overcome the difficulties. Thank you.

Kadir Şentosun

Antwerp, February 2018